BEILSTEIN JOURNAL OF NANOTECHNOLOGY

Micro- and mesoporous solids: From science to application

Edited by Jörg J. Schneider

Imprint

Beilstein Journal of Nanotechnology
www.bjnano.org
ISSN 2190-4286
Email: journals-support@beilstein-institut.de

The *Beilstein Journal of Nanotechnology* is published by the Beilstein-Institut zur Förderung der Chemischen Wissenschaften.

Beilstein-Institut zur Förderung der
Chemischen Wissenschaften
Trakehner Straße 7–9
60487 Frankfurt am Main
Germany
www.beilstein-institut.de

Beilstein Journal
of Nanotechnology

Micro- and mesoporous solids: From science to application

Jörg J. Schneider

Editorial

Open Access

Address:
Department of Chemistry, Eduard-Zintl-Institute, Inorganic Chemistry,
Technische Universität Darmstadt, Petersenstr. 18, 64287 Darmstadt,
Germany

Email:
Jörg J. Schneider - joerg.schneider@ac.chemie.tu-darmstadt.de

Beilstein J. Nanotechnol. **2011,** *2,* 774–775.
doi:10.3762/bjnano.2.85

Received: 02 November 2011
Accepted: 02 November 2011
Published: 30 November 2011

This article is part of the Thematic Series "Micro- and mesoporous solids: From science to application".

Editor-in-Chief: T. Schimmel

The concept of a porous solid might sound like a term of contradiction as solids are typically regarded as a dense and compact state of matter. Of course this is obviously not so, and zeolites are probably the most prominent representatives of such solids, known for already more than 250 years, and have been used in technical applications for more than 50 years in industry. 200 different structural types of zeolites have already been listed, with this number increasing each year. However, the pore sizes of zeolites are restricted to well below 1 nm (for faujasite), which in turn restricts the scope of the chemistry that is possible inside the pores, typically to the molecular level.

However, in the last two decades especially, mesoporous materials having pore dimensions between 2 and approximately 50 nm have emerged, and this group has established itself as an important class of solid-state materials with a huge and still constantly growing number of new congeners with pores on the nano- to mesoscale. These can be broadly classified into inorganic, organic and metal–organic types. Nevertheless, hybrids of these compositions have even been realized, extending the diversity in the chemical composition of such mesoporous solids further still. Besides their different chemical composition, the pore morphology, geometry and pore dimensions make these materials outstanding with respect to, e.g., catalytic reaction processes, in the area of sensorics, photonics and gas storage (Figure 1). In the realm of gas storage, mesoporous metal–organic frameworks (MOFs) appeared on the scene a couple of years ago and have quickly emerged as most-promising highly meso- and macroporous materials exhibiting enormous pore volumes with inner surface areas comparable with bare nanoparticles and thus coming close to the ultimate adsorption limit for solid materials. Consequently they have paved the way for the design of new materials, e.g., for the storage of fuel molecules, such as H_2 and CH_4 as well as other technologically and environmentally important small molecules. Besides the prospective applications of mesoporous materials in these and other areas, one of the other main focus points of research into these solids is to achieve a basic understanding of what happens inside the porous framework of such a solid on the molecular, and nano- and mesocopic level, in a hierarchical order, during adsorption, desorption and chemical reactions. Alongside the development of experimental methods to unravel the details of the adsorption sites and dynamics, a theoretical understanding, e.g., employing state of the art theoretical modeling techniques, is certainly necessary. The development of synthetic concepts for the formation of two-dimensional, layered, porous structures, e.g., by swelling and delamination followed by film-formation techniques, is another avenue of basic research into exciting mesoporous materials, and the application of such mesoporous layered materials to adsorption and catalysis can certainly be envisaged in the near future.

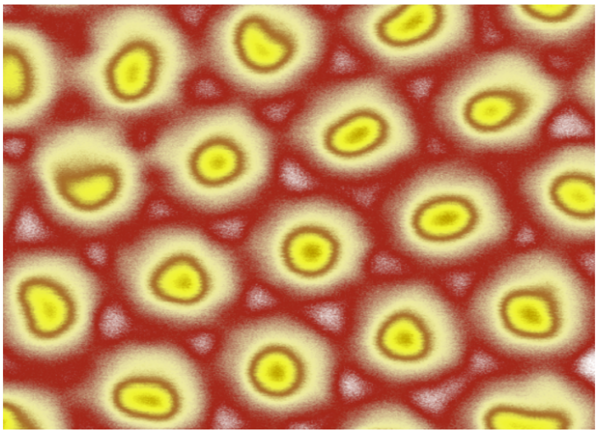

Figure 1: Artificially colorized view of a hexagonally ordered cell structure of mesoporous alumina. The pores are shown in yellow and are ca. 40 nm in diameter. The red color grading represents the typically different densities of the alumina cells surrounding the pores, which is due to the synthesis process. As with other mesoporous materials, the inner surface of the pores can be chemically modified to tune the surface chemistry and thus the functional properties.

In this Thematic Series the interested reader will find a compilation of recent experimental findings relating to mesoporous inorganic solids, covering aspects of synthesis as well as the functional properties of such materials in catalysis and sensing.

Jörg J. Schneider

Darmstadt, November 2011

License and Terms

The definitive version of this article is the electronic one which can be found at:
doi:10.3762/bjnano.2.85

Beilstein Journal
of Nanotechnology

Microfluidic anodization of aluminum films for the fabrication of nanoporous lipid bilayer support structures

Jaydeep Bhattacharya, Alexandre Kisner, Andreas Offenhäusser and Bernhard Wolfrum*

Full Research Paper

Open Access

Address:
Peter Grünberg Institute, PGI-8/ICS-8, Forschungszentrum Jülich GmbH, Leo-Brandt-Str., 52425 Jülich, Germany and Jülich - Aachen Research Alliance (JARA - FIT), Germany

Email:
Bernhard Wolfrum* - b.wolfrum@fz-juelich.de

* Corresponding author

Keywords:
anodization; lipid bilayer; microfluidics; nanofabrication; nanoporous alumina

Beilstein J. Nanotechnol. **2011,** *2,* 104–109.
doi:10.3762/bjnano.2.12

Received: 13 December 2010
Accepted: 04 February 2011
Published: 11 February 2011

This article is part of the Thematic Series "Micro- and mesoporous solids: From science to application".

Guest Editor: J. J. Schneider

Abstract

Solid state nanoporous membranes show great potential as support structures for biointerfaces. In this paper, we present a technique for fabricating nanoporous alumina membranes under constant-flow conditions in a microfluidic environment. This approach allows the direct integration of the fabrication process into a microfluidic setup for performing biological experiments without the need to transfer the brittle nanoporous material. We demonstrate this technique by using the same microfluidic system for membrane fabrication and subsequent liposome fusion onto the nanoporous support structure. The resulting bilayer formation is monitored by impedance spectroscopy across the nanoporous alumina membrane in real-time. Our approach offers a simple and efficient methodology to investigate the activity of transmembrane proteins or ion diffusion across membrane bilayers.

Introduction

In recent years nanoporous alumina membranes have gained increased attention for technical and biological applications due to their versatile implementation as biointerfaces and ease of fabrication [1-8]. Their applications range from serving as template structures in nanofabrication technology [9-20] to their direct use as functional interfaces for controlled release of molecules [21-23], co-culture development [24], or biosensing [25]. For example, Steinem et al. have demonstrated the advantages of using nanoporous membranes as support structures for lipid bilayers, which allows the monitoring of the activity of membrane proteins [26-30]. Although solid lipid support structures [31] may exhibit versatile functionality for lab-on-a-chip applications [32], only porous substrates can address the backside of the membrane via a direct fluidic interface. The advantage of nanoporous substrates over other membrane spanning systems using microapertures lies in the increased stability caused by the small pore size [33-36]. Nevertheless, alumina membranes themselves are quite brittle and therefore easy to break if mechanical handling is required. Here, we present an approach of directly fabricating alumina membranes in a microfluidic environment which allows the monitoring and manipulation of membrane characteristics during the fabrication process. We demonstrate the formation of lipid bilayers on top of the nanoporous membrane which is monitored using impedance spectroscopy.

Experimental

The experimental setup for the microfluidic anodization approach is shown schematically in Figure 1.

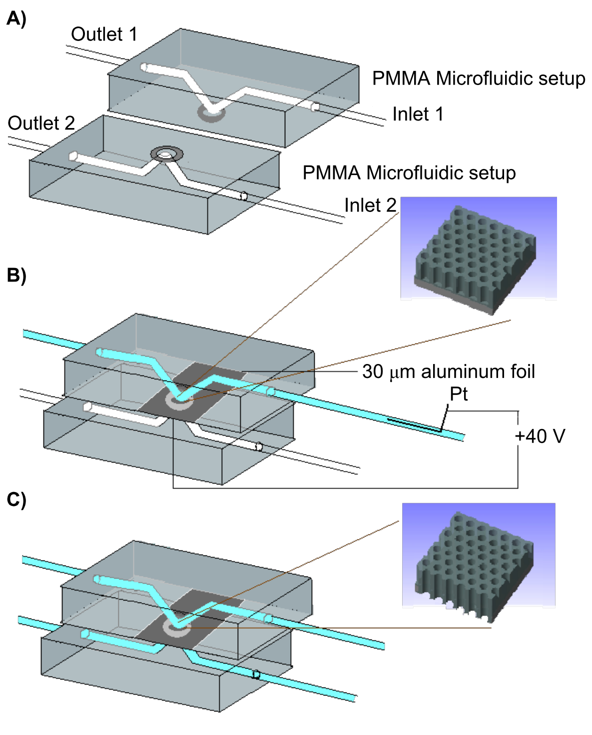

Figure 1: A) Schematics of the flow cell design for microfluidic anodization. B) An aluminum substrate is anodized at 40 V under a constant flow of oxalic acid inside a microfluidic cell to form a nanoporous alumina membrane. C) After the anodization is complete, the remaining alumina at the bottom of the pores is opened by injecting phosphoric acid into both fluidic channels.

The aluminum substrate, either a 30 μm thick aluminum foil or a thin aluminum film on an aperture released silicon support structure [21], was inserted into a PMMA dual-line flow cell. Oxalic acid (0.3 M) was injected into one of the inlets via pressure controlled flow (Fluigent, MFCS 4C, France) and contacted the exposed aluminum substrate in a localized area of 0.2 mm^2. The aluminum was then anodized under constant voltage conditions. Thus, 40 V were applied between the aluminum and a platinum counter electrode, which was inserted in the flow cell, approximately 2 cm upstream of the substrate. The aluminum anode was directly contacted outside of the flow cell. Completion of the anodization was indicated by a steep drop in the anodization current indicating the formation of a residual alumina barrier layer. Oxalic acid was then rinsed from the channel and 5% phosphoric acid injected into the upper and lower channels to remove the remaining alumina film at the bottom of the nanoporous membrane. The dissolution of the barrier layer was monitored via impedance spectroscopy (10 Hz to 10 kHz) across the nanoporous alumina membrane by a modular electrochemical system [Autolab (PGSTAT 100/FRA2), Eco Chemie Utrecht, The Netherlands] using silver/silver chloride electrodes inside the fluidic channels on both sides of the membrane. A decrease in the recorded impedance indicated opening of the pores. Some of the nanoporous films were removed from the flow cell and investigated by scanning electron microscopy (Gemini 1550 VP, Carl Zeiss, Jena, Germany).

To prepare the nanoporous membrane for lipid bilayer formation, the nanoporous alumina surface was first subjected to silanization. The silanization was carried out in the solution phase according to the method described by Steinle and coworkers [37,38] with slight modifications. Briefly, a 10% (v/v) solution of (3-aminopropyl)triethoxysilane (APTES) was prepared in pure ethanol. The solution was mixed with a 0.1 M acetate buffer (pH 5.1) to a final concentration of 5% (v/v) buffered APTES. This solution was stirred mechanically for 5 min and passed through the microfluidic channel at 500 μL/h for 2 h at 22 °C. The whole system was then cured at 60 °C for 60 min.

The lipid bilayer on the modified nanoporous alumina surface was prepared by the method of liposomal fusion [39]. The liposomes were prepared from 1-palmitoyl-2-oleoyl-*sn*-glycero-3-phosphocholine (POPC, Avanti Polar Lipids, U.S.A.) by the following method. First, 5 mL of a lipid chloroform solution (5 mg/mL) were vacuum dried in a glass vessel. Then, a phosphate buffered saline (5 mL, 0.9% NaCl, 100 mM phosphate buffer, pH 7.2) was added to form multilamelar vesicles. Sonication and extrusion (Avanti Polar Lipids, U.S.A.) were performed to produce unilamellar small vesicles of approximate sizes between 60 and 80 nm as determined by dynamic light scattering (Dynapro, Wyatt Technology Corporation, U.S.A.). The vesicle solution was then injected into the microfluidic channel for the synthesis of the lipid bilayer on the modified alumina membrane. The formation of the lipid bilayer on the nanoporous support structure was monitored by impedance spectroscopy in the range of 10 Hz to 10 kHz with a root mean square amplitude of 10 mV as measured by the Autolab system.

Results and Discussion

Figure 2 shows a typical SEM image of the nanoporous membrane after anodization and pore enlargement. An irregular pattern of pores with an average diameter of 30 ± 10 nm and a nearest neighbor interpore spacing of 40 ± 7 nm can be observed. The distance of the pores is about a factor of two lower compared to results obtained from standard anodization protocols reported in literature [40]. A smaller interpore spacing between nearest neighbors is expected due to the inhomogeneity of the pattern. Nevertheless, a potential drop inside the microfluidic cell might also contribute to a reduced pore separation. The striped pattern as well as the irregularity of the pores as opposed to perfect hexagonal ordering can be explained by the surface roughness of the untreated alumina samples and the single-step anodization process. An ordered pattern is usually obtained either by using imprint methods or a two-step anodization protocol [41]. At the front side, the pores were distributed over the whole surface area (0.2 mm^2), which had been exposed to oxalic acid. Interestingly, the backside did not reveal a similar pattern but only showed nanoporous structures in a confined region of about 300 µm^2. Such behavior is known from indented aluminum films on conducting substrates, where the indented regions exhibit advanced pore formation [15]. However, since in this investigation no inert conducting subjacent layer was present, the pore formation is expected to stop at the non-conducting alumina barrier layer after complete oxidation of the exposed aluminum film. We therefore attribute localized pore formation to the flow and diffusion profile inside the microfluidic chamber during anodization or barrier layer removal. Nevertheless, inhomogeneities in the film thickness will also affect the anodization profile and may lead to sparsely perforated regions on the backside of the membrane. A defined fluidic interface allowing precise control of the flow profile and velocity distribution could be used to study this aspect in more detail.

We investigated the formation of lipid bilayers on the nanoporous support structure inside the microfluidic cell. Figure 3 shows a plot of the impedance obtained before and after application of lipid vesicles to the front side of the silanized nanoporous membrane. The impedance measured at 10 Hz across the membrane increased by more than five orders of magnitude after vesicle application. We attribute this effect to the formation of a lipid bilayer spanning the front side of the nanoporous structure. As expected, phase changes from an ohmic to a capacitive behavior revealed the non-conducting nature of the lipid–membrane system. We chose an amino-terminated silane coating to facilitate spreading of the vesicles on the alumina surface. Vesicle rupture is probably aided via electrostatic interactions of the negative phosphate of the zwitterionic POPC-heads with the protonated amino groups from the APTES molecules immobilized on the surface [42]. In principle, one could also expect coverage of the inside pore walls, as has been observed by Bourdillon and coworkers [43,44]. However, the drastic change in impedance indicates that in our case the small pore diameter seems to favor a scenario where the nanopores are spanned by a lipid bilayer. To avoid the chemical pretreatment of the surface, an advanced deposition method of lipid bilayers on alumina as proposed by Mager et al. could be utilized [45].

Applying a simple RC equivalent circuit model to the data yields a membrane capacitance of 3.96 ± 0.1 pF. This amounts to a specific capacitance of 1.3 µF/cm^2 for an actual active area

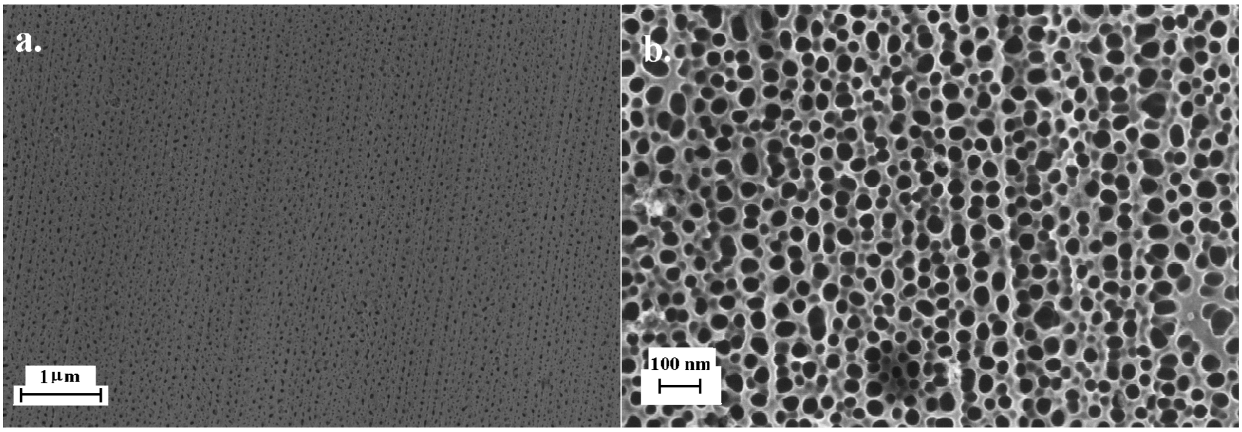

Figure 2: SEM images of the nanoporous alumina film anodized under constant flow conditions.

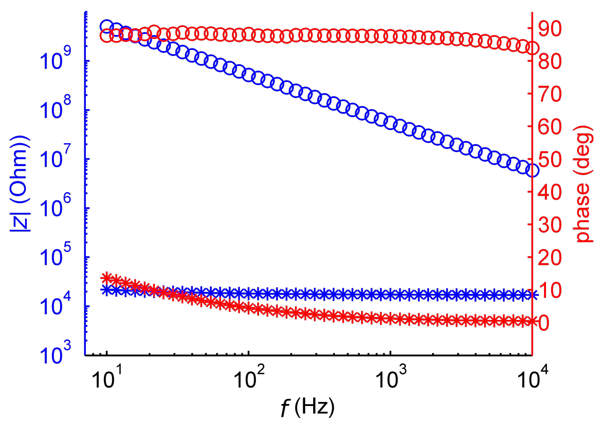

Figure 3: Impedance plot measured across the nanoporous membrane before (stars) and after (circles) lipid bilayer formation. Left axis: Absolute value of the impedance (blue). Right axis: Phase in degrees (red).

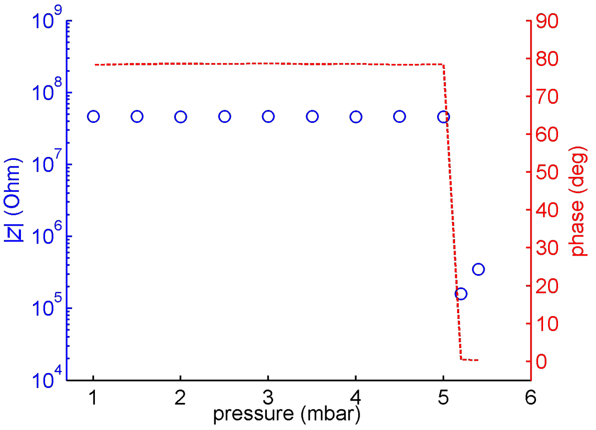

Figure 4: Impedance and phase measured at 1 kHz across the nanoporous membrane versus driving pressure for the microfluidic cell. A stable bilayer exhibits capacitive behavior at high impedance.

of 300 µm^2 in which the pores penetrate the whole substrate. This value is somewhat above the expected value of 1 µF/cm^2 measured for a pure membrane capacitance [27]. However, discrepancies can arise because of an inaccurate determination of the size of the porous membrane patch. The impedance without the bilayer showed an almost ohmic behavior around 20 kΩ. It was partially determined by the electrolyte resistance inside the microfluidic access channels leading to the nanoporous alumina membrane.

To assess the stability of the lipid bilayer under flow conditions, we measured the impedance across the membrane in dependence of the input pressure as shown in Figure 4. The bilayer could withstand an input pressure of 5.2 mbar, corresponding to a flow rate of 54 µL/min. At lower flow rates, impedance and phase exhibited a constant capacitive behavior indicating that the lipid bilayer remained intact.

At pressures above 5.2 mbar we observed a decrease in the impedance of several orders of magnitude and a phase shift towards a more ohmic behavior (Figure 4). The drop in impedance indicates that at least parts of the nanopore-spanning bilayer were ruptured under these flow conditions. For input pressures below 10 mbar, the rupture of the membrane was reversible. Once the pressure was lowered below 5.2 mbar we observed a steady increase of the impedance, which we attribute to the reformation of the lipid bilayer on the nanoporous substrate. The kinetics of the bilayer formation could be studied under this condition. Thus, we reversibly ruptured the membrane by raising the pressure to 10 mbar for 30 s before restoring the pressure to 0. Then we allowed the bilayer to settle and observed the change in impedance and phase at regular time intervals during the process. From Figure 5 we can see that after about 15 min the pore spanning bilayer was reestablished. However, at pressures above 10 mbar the bilayer was permanently damaged and could not be repaired by restoring the pressure. The resealing property of the membrane indicates that a residual lipid film remains on the modified alumina surface during moderate flow conditions. This film can subsequently act as a precursor to regenerate the pore spanning bilayers. The long time span of several minutes associated with this process is rather surprising. We attribute the delay to the diffusion of lipid molecules to the pore edges but further experiments will be necessary to elucidate this mechanism. The initial bilayer formation was even slower than the reformation process (~20–25 min). However, this delay can be explained by the time needed to accumulate a critical vesicle coverage required for rupture and bilayer formation [46-49].

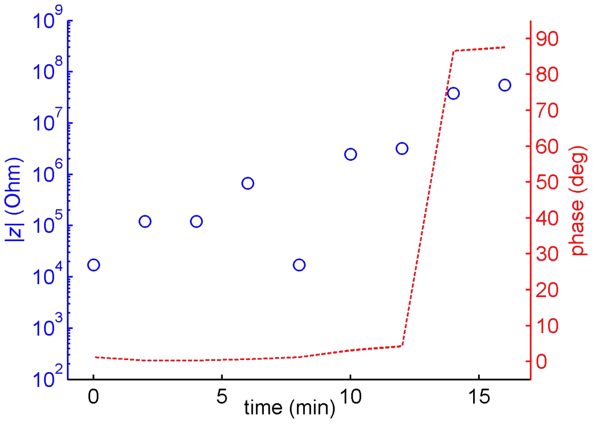

Figure 5: The kinetics of the lipid bilayer formation on a nanoporous alumina membrane is shown by measuring the impedance (blue) and the phase change (red) at 1 kHz across the nanoporous membrane over time.

Conclusion

We have demonstrated a technique for locally anodizing aluminum membranes under flow conditions. Localized anodization allows the generation of stable patches of nanoporous alumina, which can be used in microfluidic experiments. Lipid membranes were grown on the nanoporous patches inside the microfluidic system and the process of membrane formation and rupture was investigated by impedance spectroscopy. We envision the use of this technique for the investigation of transmembrane protein activity under controlled flow conditions.

Acknowledgements

We thank Dieter Strobl for the fabrication of the microfluidic cell and Dirk Mayer for helpful discussions. Funding by the Humboldt Foundation and the Helmholtz Association is gratefully acknowledged.

References

1. Karlsson, M.; Palsgard, E.; Wilshaw, P. R.; Di Silvio, L. *Biomaterials* **2003,** *24,* 3039–3046. doi:10.1016/S0142-9612(03)00146-7
2. Lee, W.; Ji, R.; Gosele, U.; Nielsch, K. *Nat. Mater.* **2006,** *5,* 741–747. doi:10.1038/nmat1717
3. Norman, J. J.; Desai, T. A. *Ann. Biomed. Eng.* **2006,** *34,* 89–101. doi:10.1007/s10439-005-9005-4
4. Popat, K. C.; Chatvanichkul, K. I.; Barnes, G. L.; LaTempa, T. J.; Grimes, C. A.; Desai, T. A. *J. Biomed. Mater. Res., Part A* **2007,** *80A,* 955–964. doi:10.1002/jbm.a.31028
5. Adiga, S. P.; Jin, C. M.; Curtiss, L. A.; Monteiro-Riviere, N. A.; Narayan, R. J. *Wiley Interdiscip. Rev.: Nanomed. Nanobiotechnol.* **2009,** *1,* 568–581. doi:10.1002/wnan.50
6. Graham, A. H. D.; Bowen, C. R.; Robbins, J.; Taylor, J. *Sens. Actuators, B* **2009,** *138,* 296–303. doi:10.1016/j.snb.2009.01.050
7. Graham, A. H. D.; Bowen, C. R.; Taylor, J.; Robbins, J. *Biomed. Microdevices* **2009,** *11,* 1091–1101. doi:10.1007/s10544-009-9326-4
8. Chung, S. H.; Son, S. J.; Min, J. *Nanotechnology* **2010,** *21,* 125104. doi:10.1088/0957-4484/21/12/125104
9. Martin, C. R. *Science* **1994,** *266,* 1961–1966. doi:10.1126/science.266.5193.1961
10. Masuda, H.; Mizuno, T.; Baba, N.; Ohmori, T. *J. Electroanal. Chem.* **1994,** *368,* 333–336. doi:10.1016/0022-0728(94)03310-2
11. Crouse, D.; Lo, Y. H.; Miller, A. E.; Crouse, M. *Appl. Phys. Lett.* **2000,** *76,* 49–51. doi:10.1063/1.125652
12. Sauer, G.; Brehm, G.; Schneider, S.; Nielsch, K.; Wehrspohn, R. B.; Choi, J.; Hofmeister, H.; Gosele, U. *J. Appl. Phys.* **2002,** *91,* 3243–3247. doi:10.1063/1.1435830
13. Sander, M. S.; Tan, L. S. *Adv. Funct. Mater.* **2003,** *13,* 393–397. doi:10.1002/adfm.200304290
14. Crouse, M. M.; Miller, A. E.; Crouse, D. T.; Ikram, A. A. *J. Electrochem. Soc.* **2005,** *152,* D167–D172. doi:10.1149/1.2032452
15. Wolfrum, B.; Mourzina, Y.; Mayer, D.; Schwaab, D.; Offenhausser, A. *Small* **2006,** *2,* 1256–1260. doi:10.1002/smll.200600311
16. Lei, Y.; Cai, W. P.; Wilde, G. *Prog. Mater. Sci.* **2007,** *52,* 465–539. doi:10.1016/j.pmatsci.2006.07.002
17. Vlad, A.; Matefi-Tempfli, M.; Antohe, V. A.; Faniel, S.; Reckinger, N.; Olbrechts, B.; Crahay, A.; Bayot, V.; Piraux, L.; Melinte, S.; Matefi-Tempfli, S. *Small* **2008,** *4,* 557–560. doi:10.1002/smll.200700724
18. Zhou, H. B.; Li, G.; Sun, X. N.; Zhu, Z. H.; Jin, Q. H.; Zhao, J. L.; Ren, Q. S. *J. Microelectromech. Syst.* **2009,** *18,* 88–96. doi:10.1109/JMEMS.2008.2011122
19. Sengupta, K.; Moyen, E.; Mace, M.; Benoliel, A. M.; Pierres, A.; Thibaudau, F.; Masson, L.; Limozin, L.; Bongrand, P.; Hanbucken, M. *Small* **2009,** *5,* 449–453. doi:10.1002/smll.200800836
20. Byun, J.; Lee, J. I.; Kwon, S.; Jeon, G.; Kim, J. K. *Adv. Mater.* **2010,** *22,* 2028–2032. doi:10.1002/adma.200903763
21. Wolfrum, B.; Mourzina, Y.; Sommerhage, F.; Offenhausser, A. *Nano Lett.* **2006,** *6,* 453–457. doi:10.1021/nl052370x
22. Prasad, S.; Quijano, J. *Biosens. Bioelectron.* **2006,** *21,* 1219–1229. doi:10.1016/j.bios.2005.05.005
23. Jiang, X. Q.; Mishra, N.; Turner, J. N.; Spencer, M. G. *Microfluid. Nanofluid.* **2008,** *5,* 695–701. doi:10.1007/s10404-008-0300-x
24. Hoess, A.; Thormann, A.; Friedmann, A.; Aurich, H.; Heilmann, A. *Adv. Eng. Mater.* **2010,** *12,* B269–B275. doi:10.1002/adem.201080010
25. Kang, M. C.; Trofin, L.; Mota, M. O.; Martin, C. R. *Anal. Chem.* **2005,** *77,* 6243–6249. doi:10.1021/ac0508907
26. Hennesthal, C.; Steinem, C. *J. Am. Chem. Soc.* **2000,** *122,* 8085–8086. doi:10.1021/ja000940j
27. Drexler, J.; Steinem, C. *J. Phys. Chem. B* **2003,** *107,* 11245–11254. doi:10.1021/jp030762r
28. Romer, W.; Lam, Y. H.; Fischer, D.; Watts, A.; Fischer, W. B.; Goring, P.; Wehrspohn, R. B.; Gosele, U.; Steinem, C. *J. Am. Chem. Soc.* **2004,** *126,* 16267–16274. doi:10.1021/ja0451970
29. Kepplinger, C.; Hofer, I.; Steinem, C. *Chem. Phys. Lipids* **2009,** *160,* 109–113. doi:10.1016/j.chemphyslip.2009.05.001
30. Schmitt, E. K.; Weichbrodt, C.; Steinem, C. *Soft Matter* **2009,** *5,* 3347–3353. doi:10.1039/b901683j
31. Sackmann, E. *Science* **1996,** *271,* 43–48. doi:10.1126/science.271.5245.43
32. Kumar, K.; Tang, C. S.; Rossetti, F. F.; Textor, M.; Keller, B.; Voros, J.; Reimhult, E. *Lab Chip* **2009,** *9,* 718–725. doi:10.1039/b814281e
33. Hirano-Iwata, A.; Taira, T.; Oshima, A.; Kimura, Y.; Niwano, M. *Appl. Phys. Lett.* **2010,** *96,* 213706–213708. doi:10.1063/1.3441298
34. Mager, M. D.; Melosh, N. A. *Adv. Mater.* **2008,** *20,* 4423–4427. doi:10.1002/adma.200800969
35. White, R. J.; Ervin, E. N.; Yang, T.; Chen, X.; Daniel, S.; Cremer, P. S.; White, H. S. *J. Am. Chem. Soc.* **2007,** *129,* 11766–11775. doi:10.1021/ja073174q
36. Kresak, S.; Hianik, T.; Naumann, R. L. C. *Soft Matter* **2009,** *5,* 4021–4032. doi:10.1039/b907661a
37. Steinle, E. D.; Mitchell, D. T.; Wirtz, M.; Lee, S. B.; Young, V. Y.; Martin, C. R. *Anal. Chem.* **2002,** *74,* 2416–2422. doi:10.1021/ac020024j
38. Penumetcha, S. S.; Kona, R.; Hardin, J. L.; Molder, A. L.; Steinle, E. D. *Sensors* **2007,** *7,* 2942–2952. doi:10.3390/s7112942
39. Brian, A. A.; McConnell, H. M. *Proc. Natl. Acad. Sci. U. S. A.* **1984,** *81,* 6159–6163. doi:10.1073/pnas.81.19.6159
40. Nielsch, K.; Choi, J.; Schwirn, K.; Wehrspohn, R. B.; Gosele, U. *Nano Lett.* **2002,** *2,* 677–680. doi:10.1021/nl025537k
41. Masuda, H.; Fukuda, K. *Science* **1995,** *268,* 1466–1468. doi:10.1126/science.268.5216.1466
42. Cha, T.; Guo, A.; Zhu, X. Y. *Biophys. J.* **2006,** *90,* 1270–1274. doi:10.1529/biophysj.105.061432

43. Fliniaux, O.; Elie-Caille, C.; Pantigny, J.; Bourdillon, C. *Electrochem. Commun.* **2005,** *7,* 697–702. doi:10.1016/j.elecom.2005.04.023
44. Proux-Delrouyre, V.; Laval, J. M.; Bourdillon, C. *J. Am. Chem. Soc.* **2001,** *123,* 9176–9177. doi:10.1021/ja010361u
45. Mager, M. D.; Almquist, B.; Melosh, N. A. *Langmuir* **2008,** *24,* 12734–12737. doi:10.1021/la802726u
46. Mashaghi, A.; Swann, M.; Popplewell, J.; Textor, M.; Reimhult, E. *Anal. Chem.* **2008,** *80,* 3666–3676. doi:10.1021/ac800027s
47. Reimhult, E.; Hook, F.; Kasemo, B. *Langmuir* **2003,** *19,* 1681–1691. doi:10.1021/la0263920
48. Richter, R. P.; Berat, R.; Brisson, A. R. *Langmuir* **2006,** *22,* 3497–3505. doi:10.1021/la052687c
49. Richter, R.; Mukhopadhyay, A.; Brisson, A. *Biophys. J.* **2003,** *85,* 3035–3047. doi:10.1016/S0006-3495(03)74722-5

License and Terms

The definitive version of this article is the electronic one which can be found at:
doi:10.3762/bjnano.2.12

Beilstein Journal
of Nanotechnology

Pore structure and surface area of silica SBA-15: influence of washing and scale-up

Jörg P. Thielemann[1,2], Frank Girgsdies[1], Robert Schlögl[1]
and Christian Hess*[2]

Full Research Paper

Open Access

Address:
[1]Abteilung Anorganische Chemie, Fritz-Haber-Institut der Max-Planck-Gesellschaft, Faradayweg 4–6, 14195 Berlin, Germany and [2]Eduard-Zintl-Institut für Anorganische und Physikalische Chemie, Technische Universität Darmstadt, Petersenstr. 20, 64287 Darmstadt, Germany

Email:
Christian Hess* - hess@pc.chemie.tu-darmstadt.de

* Corresponding author

Keywords:
SBA-15; scale-up; silica mesoporous material; tensile strength effect; washing

Beilstein J. Nanotechnol. **2011,** *2,* 110–118.
doi:10.3762/bjnano.2.13

Received: 01 November 2010
Accepted: 12 January 2011
Published: 16 February 2011

This article is part of the Thematic Series "Micro- and mesoporous solids: From science to application"

Guest Editor: J. J. Schneider

Abstract

The removal of the surfactant ($EO_{20}PO_{70}EO_{20}$) by washing before final calcination is a critical step in the synthesis of silica SBA-15. In contrast to washing with pure water or ethanol, washing with water *and* ethanol may, depending on the quantity of solvent used, alter the homogeneity and order of the pores, but also lead to an increase of the surface area of SBA-15. A reduction of solvent volume and a controlled washing protocol allow the synthesis of high surface area SBA-15 materials with a narrow monomodal pore size distribution. For larger batch sizes the influence of the quantity of solvent on the quality of the SBA-15 is reduced.

Introduction

SBA-15 is a mesoporous silica sieve based on uniform hexagonal pores with a narrow pore size distribution and a tunable pore diameter of between 5 and 15 nm [1]. The thickness of the framework walls is about 3.1 to 6.4 nm, which gives the material a higher hydrothermal and mechanical stability than, for instance, MCM-41 [2]. The high internal surface area of typically 400–900 m^2/g makes SBA-15 a well suited material for various applications. It can be used in environmental analytics for adsorption and separation [3,4], advanced optics [5,6], as a support material for catalysts [7,8] and as a template for the production of nanostructured carbon or platinum replica [9,10].

SBA-15 is synthesized in a cooperative self-assembly process under acidic conditions using the triblock copolymer Pluronic 123 ($EO_{20}PO_{70}EO_{20}$) as template and tetraethoxysilane (TEOS) as the silica source [11]. After synthesis, the template can be removed by calcination [1,12], washing [13,14], reflux extraction [1,12], acid [15], H_2O_2 treatment [16], extraction with supercritical CO_2 [17] and microwave digestion [18]. In the literature template removal is often carried out using pure solvents such as water [19], acetone [7] or ethanol [20,21]. According to Bae et al. using ethanol instead of water is three times more effective in removing the template from the SBA-15 framework, although the Pluronic 123 cannot be removed completely from the SBA-15 by washing, as shown by thermogravimetric analysis (TGA) [22]. Also the more effective template removal by ethanol is connected with shrinkage of the SBA-15 structure as observed by Ko et al. [13].

To the best of our knowledge there are no reports on SBA-15 synthesis using a washing approach with two solvents. In the following we will show that the use of two solvents while washing can lead to an increase of the surface area and that for small batches the volume of the solvents has an impact on the surface area and pore size distribution of SBA-15. Also the influence of scaling up to 27 g per batch on the properties of SBA-15 is discussed. Up until now the largest synthesis scale as reported by Tkachenko et al. corresponded to approximately 24.5 g [23].

The paper is organised as follows: In the first section the influence of washing freshly synthesised SBA-15 with water or ethanol is discussed. The second section deals with a combined washing approach using water and ethanol. Particular emphasis is put on the effect of the solvent quantities being used while washing. The third section addresses the issue of scaling up the SBA-15 synthesis to 9 times the size described in the original procedure by Zhao et al. [1,12].

Results and Discussion

Template removal by washing with a single solvent

The removal of the Pluronic 123 template ($EO_{20}PO_{70}EO_{20}$) by washing prior to calcinations is a crucial step in the synthesis of SBA-15. Therefore, a series of experiments was conducted to understand first the effect of each solvent separately (water, ethanol), and then the effect of a combination of these two solvents while washing. To investigate the batch size dependence while washing with a single solvent, a 9× batch was separated into two 1× half batches and two 3× half batches (see Experimental section for detailed information). As the results for both half batches were similar, only the 1× half batch will be discussed in the following.

The shape of the isotherms of sample **1** (Figure 1) is almost ideally type-IV and no change of the hysteresis was observed with the different washing procedures. This means that the homogeneity and order of the hexagonal pores were not altered by washing. The surface area and the pore volume of the untreated reference sample **1A** and the water treated sample **1C** is nearly the same, whereas the surface area and pore volume of the ethanol treated sample **1B** is significantly reduced by 150 m^2/g and 0.2 cm^3/g. The shrinking of pore volume and surface area while washing with pure ethanol seems to be due to more efficient removal of the surfactant from the meso- and micropores than with pure water [13]. The shrinking also affected the ratio between micro- and mesopores. The ethanol washed sample **1B** exhibited more and the water washed sample **1C** less micropore volume than the unwashed reference samples **1A** (Table 1).

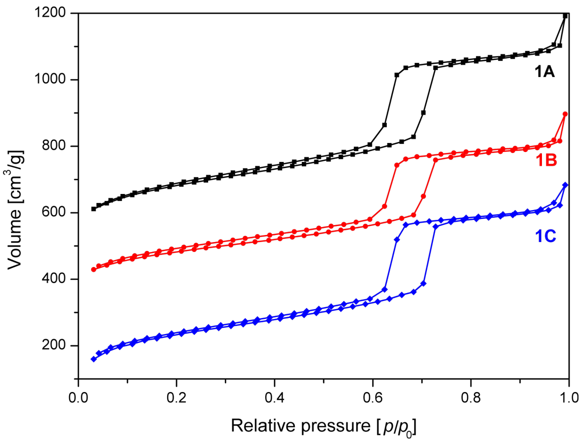

Figure 1: N_2 adsorption/desorption isotherms of SBA-15 unwashed (**1A**), after washing with 30 mL ethanol (**1B**) and 30 mL water (**1C**). The isotherms are offset by 450 (**1A**) and 300 (**1B**) cm^3/g.

Figure 2 depicts the pore size distributions of the adsorption branch of the isotherm for the three samples, which are quite similar. The pore size distributions were characterized by a maximum at 70 Å (samples **1A** and **1C**) and 73 Å (sample **1B**) and a FWHM of 8 Å was observed. The high order of the mesopores of samples **1A–C** – compared to SBA-15 samples **2C** and **3C** reported in later sections – was also corroborated by XRD results (Figure 3). Independent of the washing procedure the (100), (110) and (200) reflections occur at almost the same position with the same relative intensity.

Influence of combined washing with ethanol and water

In contrast to washing with a pure solvent, the combined washing with ethanol and water may lead to an increase of surface area (Table 1), but also damages the material. The damage is observed as a bulge in the desorption branch of the BET isotherm. To investigate the possible sources for this decreased homogeneity of the pores the following potential

Table 1: Surface and porosity characteristics of SBA-15 samples washed with pure water, ethanol and a combination of ethanol and water.

SBA-15 sample	washing procedure[a]	S_{Micro} (m^2/g)[b]	S_{Total} (m^2/g)[c]	S_{Micro}/S_{Total}[d]	D_P (Å)[e]	a_0 (Å)[f]	a_0-D_P (Å)[g]	V_{Total} (cm^3/g)[h]
1A	no washing	263	700	0.38	70	108	38	0.98
1B	30 mL ethanol	300	551	0.54	73	110	37	0.78
1C	30 mL water	213	709	0.30	70	108	38	0.94
2A	no washing	267	671	0.40	68	107	39	0.88
2B	5 mL ethanol/water	381	817	0.47	70	109	39	1.01
2C	30 mL ethanol/water	215	573	0.38	61	100	39	0.62
3A	no washing	297	758	0.39	70	111	41	0.88
3B	5 mL ethanol/water (1× half batch)	389	872	0.45	70	107	37	1.11
3C	35 mL ethanol/water (1× half batch)	343	755	0.45	68	109	41	0.87
3D	120 mL ethanol/water (3× half batch)	354	790	0.45	70	109	39	0.96
3E	350 mL ethanol/water (9× half batch)	364	838	0.43	70	111	41	1.06

[a]solvent volume used per washing cycle; [b]micropore surface area; [c]total BET surface area; [d]fraction of the micropore surface area of the total BET surface area; [e]pore diameter determined from the adsorption isotherms by the NLDFT method; [f]unit-cell parameter (a_0) determined from small-angle XRD; [g]pore wall thickness estimated by subtracting the pore diameter value (D_P) from the hexagonal unit-cell dimension (a_0); [h]total pore volume.

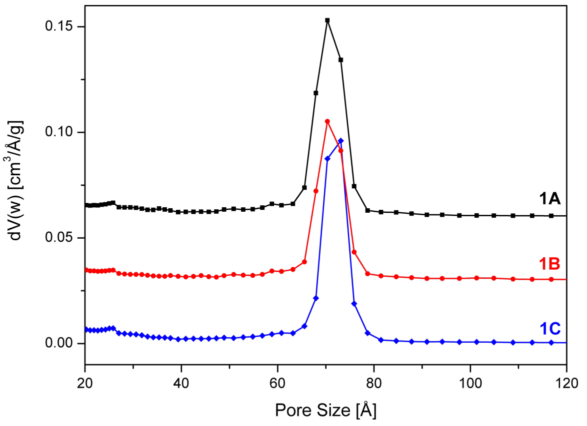

Figure 2: NLDFT pore size distributions of SBA-15 unwashed (**1A**), after washing with 30 mL ethanol (**1B**) and 30 mL water (**1C**) calculated from the adsorption branch of the isotherm. The pore size distributions are offset by 0.06 (**1A**) and 0.03 (**1B**) cm³/Å/g.

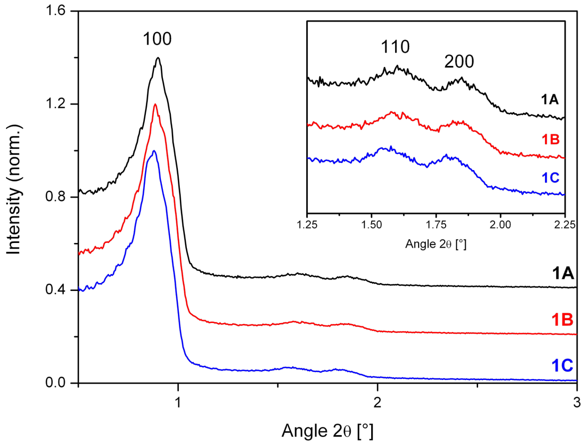

Figure 3: Small angle XRD of SBA-15 unwashed (**1A**), after washing with 30 mL ethanol (**1B**) and 30 mL water (**1C**). The intensities are normalized to the (100) reflection and offset by 0.4 (**1A**) and 0.2 (**1B**).

influences on the synthesis were examined and excluded: (i) temperature in the first synthesis step a) by precise temperature stabilization at 35 °C and avoidance of any temperature fluctuations b) by increasing the synthesis temperature to 37 °C, (ii) variation of the addition velocity of tetraethoxysilane (TEOS), (iii) stirring velocity during the synthesis and TEOS addition, (iv) heating rate and temperature fluctuation at the aging step (85 °C), (v) influence of the cooling rate after aging, (vi) tightness of the bottle while aging and (vii) influence of grinding after synthesis. Van der Voort et al. and Kruk et al. [24,25] report that an increased TEOS/surfactant ratio can influence the structure of the SBA-15. Therefore, according to their recommendation (viii) the TEOS/surfactant ratio was fixed to 58:1 for all samples to exclude it as source for the observed disorder. Importantly, it was found that under the chosen conditions only the amount of solvent used in the washing process had a significant influence on the shape of the isotherm of the final product (Figure 4).

To gain insight into the influence of solvent volume, a single batch (sample **2**) was split into two half batches. A reference sample **2A** of 80 mg, which was not washed, was taken before

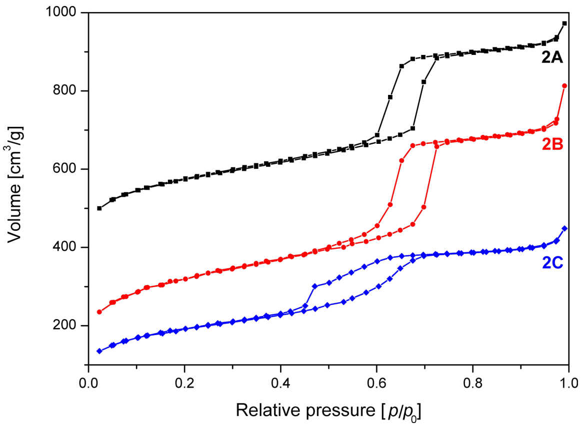

Figure 4: N_2 adsorption/desorption isotherms of SBA-15 unwashed (**2A**), after washing with 5 mL (**2B**) and 30 mL (**2C**) quantities of solvent. The isotherms are offset by 350 (**2A**) and 50 (**2B**) cm^3/g.

splitting into two half batches. One of the half batches was gently washed with 5 mL (**2B**) and the other with 30 mL (**2C**) of solvent. All samples were subsequently calcined at 550 °C. The resulting samples were analyzed regarding BET surface area, pore size distribution and pore volume (Figure 5, Figure 6 and Table 1).

The reference sample **2A**, which was not washed shows the best isotherm hysteresis and a narrow pore size distribution (FWHM = 9 Å) as calculated from the adsorption branch of the isotherm (Figure 5 and Table 1). In comparison to the other two samples, the gently washed sample **2B** shows a significantly increased surface area and a narrow pore size distribution (FWHM = 9 Å) with a maximum at 70 Å. In contrast, sample **2C** washed with plenty of solvent shows a significantly changed shape of the isotherm as evidenced by the bulge in the desorption branch at p/p_0 = 0.45 as well as by a reduced surface area compared to sample **2B**.

The closure of the hysteresis loop at p/p_0 values between 0.4 and 0.45 for sample **2C** can be explained by the tensile strength effect [26,27]. The effect occurs when interconnected pores filled with N_2 at 77 K are emptied through smaller pores or narrower sections along the pore. In those pores with a diameter below 50 Å the N_2 evaporation is delayed until a critical pressure $(p/p_0)_{TSE}$ is reached, at which the hemispherical meniscus collapses and the pores are immediately emptied. This also leads to the observed forced closure of the hysteresis loop as pores with smaller diameter do not show a hysteresis [28]. As a result there is a typical sharp peak at 50 Å in the pore size distribution (Figure 6), which can be considered an artefact [26]. Therefore, as recommended [27,29] the unaffected adsorption branch of the isotherm was used to calculate the pore size distribution.

Nevertheless, the pore size distribution of sample **2C** calculated from the adsorption branch of the isotherm is relatively broad and shifted to 61 Å as compared to samples **2A** and **2B**. This behaviour shows that the order of the pores in sample **2C** has decreased due to washing with increased solvent quantities. The ratio of the microporous to mesoporous surface area for **2C** stays almost constant compared to **2A**, whereas the contents of micropore surface area is increased by 7% for **2B** (Table 1).

The reduced order of homogeneity of the pores can be also observed in the XRD data (Figure 7), as the (110) and (200) reflections almost disappear for the extensively washed

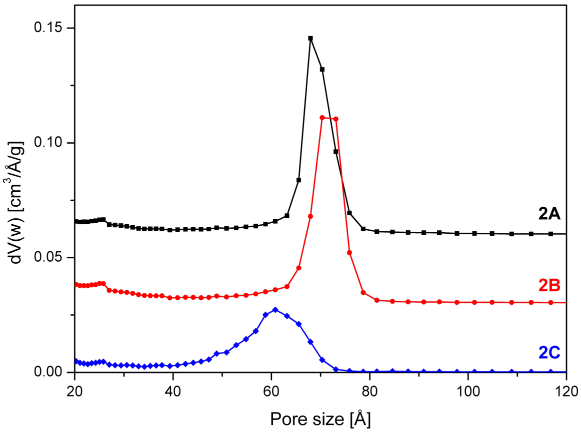

Figure 5: NLDFT pore size distribution of SBA-15 unwashed (**2A**), after washing with 5 mL (**2B**) and 30 mL (**2C**) quantities of solvent calculated from the adsorption branch of the isotherm. The pore size distributions are offset by 0.05 (**2A**) and 0.025 (**2B**) cm^3/Å/g.

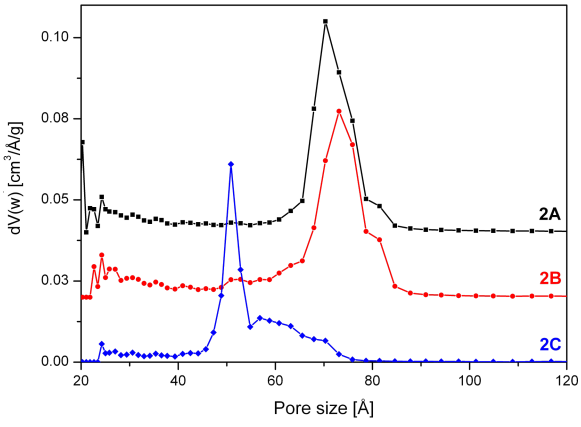

Figure 6: NLDFT pore size distribution of SBA-15 unwashed (**2A**), after washing with 5 mL (**2B**) and 30 mL (**2C**) quantities of solvent calculated from the desorption branch of the isotherm. The pore size distributions are offset by 0.5 (**2A**) and 0.25 (**2B**) cm^3/Å/g.

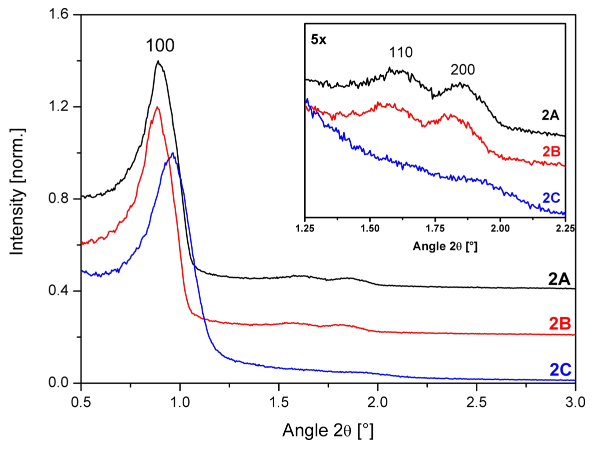

Figure 7: Small angle XRD of SBA-15 unwashed (**2A**), after washing with 5 mL (**2B**) and 30 mL (**2C**) quantities of solvent. The intensities are normalized to the (100) reflection and offset by 0.4 (**2A**) and 0.2 (**2B**).

SBA-15 sample **2C**. Also the lattice constant a_0 (Table 1) of sample **2C** is reduced by 9 Å compared to sample **2B**, showing that plenty of washing leads to a shrinking of the SBA-15 structure.

Influence of scaling up on the washing effect

In the previous section it was pointed out that the amount of solvent used while washing has a significant influence on the shape of the isotherm and thus also on the pore size distribution of the resulting SBA-15. To investigate to which extent a synthesis scale up is influenced by this “washing effect” a 9× batch was split into sub factions resembling 9×, 3×, 1× half size batches. Before washing a reference sample (80 mg) was taken from the 9× batch and calcined at 550 °C. The half size batches were then washed with linearly scaled up amounts of solvent based on material weight and also calcined at 550 °C.

Interestingly, the BET isotherms of the 1× half batch (Figure 8), which was obtained by dividing the 9× batch into smaller factions, shows similar features to the 1× half batch discussed in the previous section. The surface area was maximized in the little washed sample **3B** (Table 1) and the typical bulge in the desorption branch due to the tensile strength effect was observed at p/p_0 = 0.45 for **3C** (Figure 8). As the extent of the bulge is lower compared to sample **2C,** the order of the mesopores appears to be slightly higher for the scaled up sample after washing with plenty of solvent. This is also reflected in the pore size distributions shown in Figure 9 as the maximum for **3C** is shifted only by 2 Å as compared to the 7 Å shift in case of **2C**. Furthermore, the peak broadening of **3C** is much lower as in case of **2C**.

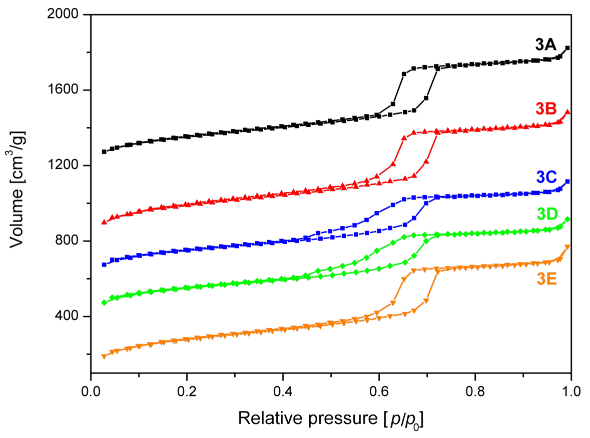

Figure 8: N_2 adsorption/desorption isotherms of SBA-15 sample **3** devided into a 1× half batch unwashed (**3A**), after washing with 5 mL (**3B**) and 30 mL (**3C**), a 3× half batch washed with 120 mL (**3D**) and a 9× half batch washed with 350 mL (**3E**) quantities of solvent. The isotherms are offset by 1100 (**3A**), 700 (**3B**), 500 (**3C**), 300 (**3D**) cm^3/g.

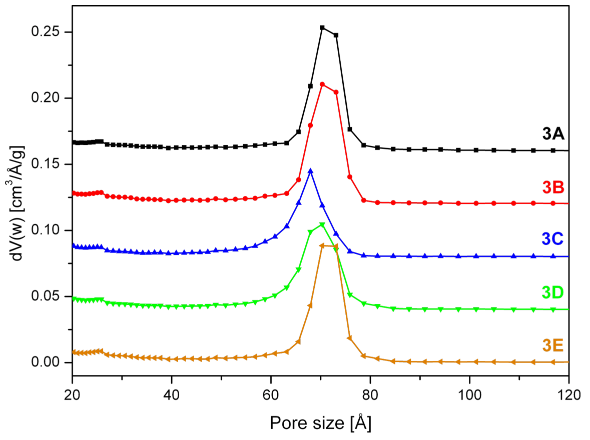

Figure 9: NLDFT pore size distribution of SBA-15 sample **3** calculated from the adsorption branch of the isotherm. The sample was devided into a 1× half batch unwashed (**3A**), after washing with 5 mL (**3B**) and 30 mL (**3C**), a 3× half batch washed with 120 mL (**3D**) and a 9× half batch washed with 350 mL (**3E**) quantities of solvent. The pore size distributions are offset by 0.16 (**3A**), 0.12 (**3B**), 0.08 (**3C**) and 0.04 (**3D**) cm^3/Å/g.

Comparison of the desorption branches of the isotherms of the extensively washed samples **3C**, **3D**, **3E** (Figure 8) revealed that with increasing batch size the bulge at relative pressure 0.45 decreases and the surface area increases. This indicates that the mesopores in the material become more ordered and homogeneous during the scale-up.

These results were also corroborated by small angle XRD. On the one hand, as can be seen in Figure 10, the relative intensity of the (110) and (200) reflections decreases compared to the (100) reflection from **3A, 3B** to **3C**, which shows that order of

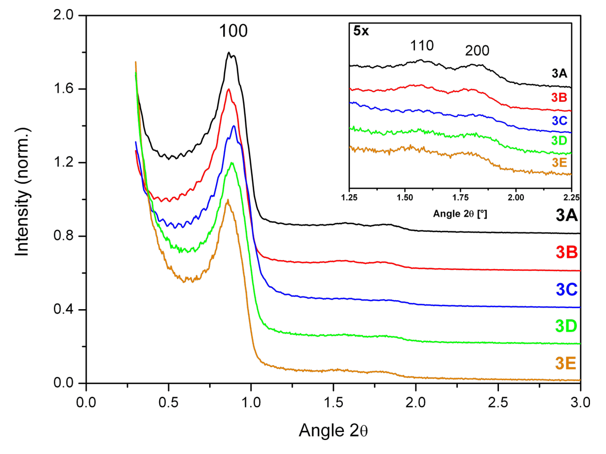

Figure 10: XRD of SBA-15 sample **3** devided into a 1× half batch unwashed (**3A**), after washing with 5 mL (**3B**) and 30 mL (**3C**), a 3× half batch washed with 120 mL (**3D**) and a 9× half batch washed with 350 mL (**3E**) quantities of solvent. The intesities are normalized to the (100) reflection and offset by 0.8 (**3A**), 0.6 (**3B**), 0.4 (**3C**) and 0.2 (**3D**). Note: Oscillations are an artefact in the measurement.

the mesopores decreases when the amount of solvent for the downscaled 1× half batch is increased. On the other hand, an increase of the mesopore order with batch size is observed for the extensively washed samples **3C**, **3D**, **3E** as the relative intensity of the (110) and (200) reflections increases.

An explanation for the higher quality of the SBA-15 may be that the washing process becomes less effective on linear scale up. This behaviour is also consistent with the observation, that for smaller batches (samples **2A**–**C** and **3A**–**C**) washing with less solvent leads to a higher quality of the SBA-15.

As described above, combined washing with ethanol and water may modify the SBA-15 mesopores. While small amounts of solvent lead to an increase in surface area without significant effects on pore structure, extensive washing strongly reduces the surface area as well as the order of the pores. A possible explanation for this behaviour could be that the template has a higher solubility in ethanol than in water. Therefore ethanol leads to a more efficient removal of the template as described by Ko and Bae [13,22]. The cleaned surface of the SBA-15 can then come into full contact with the water which being more polar is a better source for H^+ and OH^- and might induce hydrolysis reactions. As a result, narrowing and widening of part of the SBA-15 mesopores may take place (Figure 11). Besides, during extensive washing the formation of blocked pores cannot be ruled out which would offer a straightforward explanation for the significant reduction in surface area. The presence of narrowed and blocked mesopores causes delayed evaporation leading to a lower desorption pressure p/p_0 and changes in the shape of the desorption branch of the isotherm. The pores of the prepared SBA-15 materials exhibit an average diameter of 70 Å. If part of those pores is narrowed to approximately 50 Å or lower, evaporation is delayed [25-27]. As a result the tensile strength effect is observed at p/p_0 = 0.45 leading to a forced closure of the hysteresis loop. Its extent depends on the degree of modification, in particular, the number of narrowed sections created during washing. The height of the bulge in the desorption branch may therefore be used to estimate qualitatively the degree of disorder created by combinational washing with plenty of solvent. However, the forced closure of the hysteresis loop is temperature and adsorptive dependent [30,31]. Therefore argon adsorption/desorption measurements, for example, are a good solution to distinguish more clearly between pores with constrictions, plugs or corrugated surface and to obtain more reliable quantitative information about the pore size distribution [24].

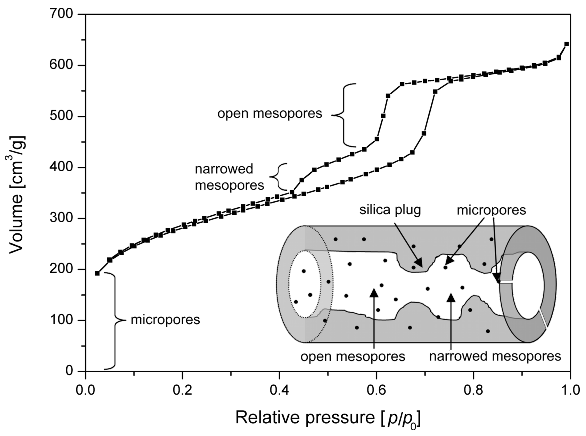

Figure 11: Effect of narrowed pores in the SBA-15 structure on the isotherm shape.

The observed effect on the isotherm shape and the interpretation as blocking or narrowing of the mesopores has also been described by other researchers [25,32-35]. Vansant et al., for instance, reported for Plugged Hexagonal Templated Silica (PHTS), which is a material analogous to SBA-15, synthesized at different TEOS/Pluronic 123 ratios, the occurrence of pore narrowing and blocking by silica nanoparticles inside the pores [25,32-34]. Tian et al. polymerized *N*-isopropylacrylamide inside the SBA-15 structure and explained their XRD results and the isotherm shape with a bulge at p/p_0 = 0.45 by the presence of a poly-*N*-isopropylacrylamide layer of varying thickness on the SBA-15 surface [35].

Conclusion

Washing with plenty of pure solvent (water or ethanol) does not alter the homogeneity and order of the pores in SBA-15. A combined washing approach using water and ethanol increases the surface area, but may change the SBA-15 when plenty of solvent is used. The change can be observed as a bulge at a p/p_0 value of 0.45 in the desorption branch of the nitrogen adsorption isotherm (tensile strength effect) and a decrease of the long range order in XRD. This may be attributed to hydrolysis and re-condensation reactions of the silica in the pore wall, which leads to a narrowing or widening of certain pore sections. Thus, controlled washing with reduced quantities of solvent is the optimum condition for obtaining an increased surface area and a narrow monomodal pore size distribution. Scale up of the SBA-15 synthesis reduces the influence of the solvent volume on the shape of the isotherm and the pore size distribution.

Experimental

Synthesis of SBA-15

4.07 g Pluronic 123 were dissolved in 30 mL distilled water and 120 mL 2 M hydrochloric acid in a perfluoralkoxylalkane (PFA) bottle at 35 °C. Afterwards, 9 mL of tetraethoxysilane (TEOS) were added and the mixture was stirred (600 rpm) at 35 °C for 20 h in the closed bottle. The resulting white suspension was then aged at 85 °C for 24 h without stirring. After cooling to room temperature, the copolymer was removed by washing with distilled water and/or ethanol using a G4 frit. The product was dried at room temperature over night and then calcined at 550 °C for 12 h. Then the product was carefully ground and characterized by N_2 adsorption/desorption isotherms. The FWHM and intensity maxima of the pore size distribution were determined by fitting with a Gaussian function. The batches were also increased in size (3×, 9×), as compared to the size described in the literature [1,12]. These batches are referred to as 3× or 9× batches. When they were divided into two smaller batches they were named 3× or 9× half batches. The yield for a 1×, 3× and 9× batch was 2.5 g, 7.5 g and 25 g SBA-15. The residue carbon content of the SBA-15 determined by elemental analysis after calcination was – independent of batch size and washing procedure – 0.09 % at maximum.

Details of the washing procedure

Two batches produced under the same synthesis conditions can still show small variations regarding surface area, pore volume and pore size distribution, which makes it difficult to study the pure effect of washing. The absolute surface area and pore volume may deviate from batch to batch by ±5%. For the pore size distribution this deviation is about ±2%. To overcome this problem, a batch or scaled up batch was divided into two identical half batches and a small, unwashed reference sample of approximately 80 mg. The weight of the reference samples is negligible compared to the two half batches which are used for the washing experiments. The washing was always performed 15 times with a defined quantity of solvent which was poured on to the sample in the G4 frit at 25 °C and subsequently removed by suction during each washing cycle. Additionally, the sample was carefully stirred with a glass rod after each addition of solvent. The combined washing approach consisted of washing with defined quantities of water (5×), ethanol (5×) and again water (5×). In the case where only pure solvent was used the amount of each solvent quantity and the total number of washing cycles (15×) was comparable as in case of the combined washing approach. In Table 2 typical contact times of the solvents for each washing step with dependence on the batch size are given.

Table 2: Typical contact times while washing.

SBA-15 sample	washing procedure[a]	contact time (min) water	ethanol	water
3A	no washing	0	0	0
3B	5 mL ethanol/water (1× half batch)	2	2	2
3C	35 mL ethanol/water (1× half batch)	6	6	6
3D	120 mL ethanol/water (3× half batch)	15	10	11
3E	350 mL ethanol/water (9× half batch)	60	30	27

[a] solvent volume is given per washing cycle.

Nitrogen adsorption

The calcined SBA-15 samples were pre-treated in vacuum at 80 °C for 16 h and then measured on Quantachrome Autosorb-1 and Autosorb-6B instruments. The total pore volume was determined from the adsorption branch of the N_2 isotherm curve at a relative pressure of $p/p_0 = 0.95$. A standard isotherm was measured with 80 data points. For the calculation of the surface area a nitrogen cross section of 13.5 Å^2 was used [36]. The pore-size distribution was calculated from the adsorption and desorption branch of the isotherm using the NLDFT method and its FWHM determined by fitting with a Gaussian function. The micro-pore surface area was calculated at p/p_0 values from 0.3 to 0.45 with the t-plot method by de Boer [37].

X-ray diffraction

Low angle X-ray diffraction (XRD) measurements were performed on a conventional (i.e., wide angle) STOE STADI P transmission powder diffractometer, equipped with a primary focusing Ge monochromator (Cu Kα_1 radiation) and scintillation counter. In order to enhance the accuracy of the 2θ scale, a measurement mode with two symmetric scans (negative and positive 2θ) was chosen. Small amounts of powdered sample were sandwiched between two layers of polyacetate film and fixed with a small amount of X-ray amorphous grease. This sandwich was clamped into a sample holder ring, which was rotated around the primary beam axis. At low angles, small differences in 2θ result in significant errors on the d-spacing scale. Thus, the diffractions patterns were evaluated using correlated fitting of the asymmetric diffraction peaks. An asymmetric instrumental function was convoluted with a symmetric Voigt function representing the sample contribution. A common lattice parameter a and a common 2θ offset (zero error) was refined on the (100), (110) and (200) peaks of the two-dimensional hexagonal lattice for both scan ranges (negative and positive) simultaneously. Due to the internal 2θ calibration based on the symmetric scan mode and correlated fitting, the instrumental zero error can be determined with high precision, yielding a more reliable determination of the a_0 lattice parameter in turn. Thus, this procedure allows a robust and reproducible evaluation of the d-values of differently treated samples. However, it needs to be kept in mind that, both, due to the asymmetric peak shape and the strongly asymmetric background, these values will depend strongly on the evaluation procedure applied. Thus, care should be taken when comparing the results of different studies on an absolute scale.

Acknowledgements

The authors would like to thank Gisela Lorenz for conducting the N_2 adsorption/desorption experiments. Till Wolfram is kindly acknowledged for fruitful discussions regarding BET analysis. In addition, we would like to thank Sigrid Imme from the Chemistry Department of the Technische Universität Berlin for performing the elemental analysis.

References

1. Zhao, D. Y.; Feng, J. L.; Huo, Q. S.; Melosh, N.; Fredrickson, G. H.; Chmelka, B. F.; Stucky, G. D. *Science* **1998,** *279,* 548–552. doi:10.1126/science.279.5350.548
2. Cassiers, K.; Linssen, T.; Mathieu, M.; Benjelloun, M.; Schrijnemakers, K.; Van Der Voort, P.; Cool, P.; Vansant, E. F. *Chem. Mater.* **2002,** *14,* 2317–2324. doi:10.1021/cm0112892
3. Hoang, V. T.; Huang, Q.; Eic, M.; Do, T. O.; Kaliaguine, S. *Langmuir* **2005,** *21,* 2051–2057. doi:10.1021/la048349d
4. Han, Y. J.; Stucky, G. D.; Butler, A. *J. Am. Chem. Soc.* **1999,** *121,* 9897–9898. doi:10.1021/ja992138r
5. Scott, B. J.; Wirnsberger, G.; Stucky, G. D. *Chem. Mater.* **2001,** *13,* 3140–3150. doi:10.1021/cm0110730
6. Yang, P.; Wirnsberger, G.; Huang, H. C.; Cordero, S. R.; McGehee, M. D.; Scott, B.; Deng, T.; Whitesides, G. M.; Chmelka, B. F.; Buratto, S. K.; Stucky, G. D. *Science* **2000,** *287,* 465–467. doi:10.1126/science.287.5452.465
7. Hess, C. *ChemPhysChem* **2009,** *10,* 319–326. doi:10.1002/cphc.200800585
8. Cavalleri, M.; Hermann, K.; Knop-Gericke, A.; Hävecker, M.; Herbert, R.; Hess, C.; Oestereich, A.; Döbler, J.; Schlögl, R. *J. Catal.* **2009,** *262,* 215–223. doi:10.1016/j.jcat.2008.12.013
9. Ryoo, R.; Ko, C. H.; Kruk, M.; Antochshuk, V.; Jaroniec, M. *J. Phys. Chem. B* **2000,** *104,* 11465–11471. doi:10.1021/jp002597a
10. Lu, A.; Schüth, F. *Adv. Mater.* **2006,** *18,* 1793–1805. doi:10.1002/adma.200600148
11. Yu, C.; Fan, J.; Tian, B.; Zhao, D. *Chem. Mater.* **2004,** *16,* 889–898. doi:10.1021/cm035011g
12. Zhao, D.; Huo, Q.; Feng, J.; Chmelka, B. F.; Stucky, G. D. *J. Am. Chem. Soc.* **1998,** *120,* 6024–6036. doi:10.1021/ja974025i
13. Kruk, M.; Jaroniec, M.; Ko, C. H.; Ryoo, R. *Chem. Mater.* **2000,** *12,* 1961–1968. doi:10.1021/cm000164e
14. Chong, A. S. M.; Zhao, X. S. *J. Phys. Chem. B* **2003,** *107,* 12650–12657. doi:10.1021/jp035877+
15. Yang, C. M.; Zibrowius, B.; Schmidt, W.; Schüth, F. *Chem. Mater.* **2004,** *16,* 2918–2925. doi:10.1021/cm049526z
16. Yang, L. M.; Wang, Y. J.; Luo, G. S.; Dai, Y. Y. *Microporous Mesoporous Mater.* **2005,** *81,* 107–114. doi:10.1016/j.micromeso.2005.01.023
17. van Grieken, R.; Calleja, G.; Stucky, G. D.; Melero, J. A.; Garcia, R. A.; Iglesias, J. *Langmuir* **2003,** *19,* 3966–3973. doi:10.1021/la026970c
18. Tian, B.; Liu, X.; Yu, C.; Gao, F.; Luo, Q.; Xie, S.; Tu, B.; Zhao, D. *Chem. Commun.* **2002,** 1186–1187. doi:10.1039/b202180c
19. Luan, Z.; Maes, E. M.; van der Heide, P. A. W.; Zhao, D.; Czernuszewicz, R. S.; Kevan, L. *Chem. Mater.* **1999,** *11,* 3680–3686. doi:10.1021/cm9905141
20. Perathoner, S.; Lanzafame, P.; Passalacqua, R.; Centi, G.; Schlögl, R.; Su, D. S. *Microporous Mesoporous Mater.* **2006,** *90,* 347–361. doi:10.1016/j.micromeso.2005.10.024
21. Ojeda, M. L.; Esparza, J. M.; Campero, A.; Cordero, S.; Kornhauser, I.; Rojas, F. *Phys. Chem. Chem. Phys.* **2003,** *5,* 1859–1866. doi:10.1039/b300821e
22. Bae, Y. K.; Han, O. H. *Microporous Mesoporous Mater.* **2007,** *106,* 304–307. doi:10.1016/j.micromeso.2007.02.030
23. Tkachenko, O. P.; Klementiev, K. V.; Löffler, E.; Ritzkopf, I.; Schüth, F.; Bandyopadhyay, M.; Grabowski, S.; Gies, H.; Hagen, V.; Muhler, M.; Lu, L.; Fischer, R. A.; Grünert, W. *Phys. Chem. Chem. Phys.* **2003,** *5,* 4325–4334. doi:10.1039/b303429a
24. Kruk, M.; Jaroniec, M.; Joo, S. H.; Ryoo, R. *J. Phys. Chem. B* **2003,** *107,* 2205–2213. doi:10.1021/jp0271514
25. Van Der Voort, P.; Ravikovitch, P. I.; De Jong, K. P.; Benjelloun, M.; Van Bavel, E.; Janssen, A. H.; Neimark, A. V.; Weckhuysen, B. M.; Vansant, E. F. *J. Phys. Chem. B* **2002,** *106,* 5873–5877. doi:10.1021/jp025642i
26. Groen, J. C.; Peffer, L. A. A.; Pérez-Ramírez, J. *Microporous Mesoporous Mater.* **2003,** *60,* 1–17. doi:10.1016/S1387-1811(03)00339-1
27. Lowell, S.; Shields, J. E.; Thomas, M. A.; Thommes, M. *Characterization of Porous Solids and Powders: Surface Area, Pore Size and Density;* Kluwer Academic Publishers: Dordrecht, The Netherlands, 2004.
28. Sonwane, C. G.; Ludovice, P. J. *J. Mol. Catal. A* **2005,** *238,* 135–137. doi:10.1016/j.molcata.2005.05.013
29. Sing, K. S. W.; Everett, D. H.; Haul, R. A. W.; Moscou, L.; Pierotti, R. A.; Rouquerol, J.; Siemieniewska, T. *Pure Appl. Chem.* **1985,** *57,* 603–619. doi:10.1351/pac198557040603
30. Morishige, K.; Fujii, H.; Uga, M.; Kinukawa, D. *Langmuir* **1997,** *13,* 3494–3498. doi:10.1021/la970079u
31. Morishige, K.; Shikimi, M. *J. Chem. Phys.* **1998,** *108,* 7821–7824. doi:10.1063/1.476218
32. Van Der Voort, P.; Ravikovitch, P. I.; De Jong, K. P.; Neimark, A. V.; Janssen, A. H.; Benjelloun, M.; Van Bavel, E.; Cool, P.; Weckhuysen, B. M.; Vansant, E. F. *Chem. Commun.* **2002,** 1010–1011. doi:10.1039/b201424f

33. Meynen, V.; Cool, P.; Vansant, E. F. *Microporous Mesoporous Mater.* **2007,** *104,* 26–38. doi:10.1016/j.micromeso.2006.12.003
34. Meynen, V.; Cool, P.; Vansant, E. F.; Kortunov, P.; Grinberg, F.; Kärger, J.; Mertens, M.; Lebedev, O. I.; Van Tendeloo, G. *Microporous Mesoporous Mater.* **2007,** *99,* 14–22. doi:10.1016/j.micromeso.2006.08.029
35. Tian, B. S.; Yang, C. *J. Phys. Chem. C* **2009,** *113,* 4925–4931. doi:10.1021/jp808534q
36. Jelinek, L.; Kováts, E. *Langmuir* **1994,** *10,* 4225–4231. doi:10.1021/la00023a051
37. de Boer, J. H.; Linsen, B. G.; van der Plas, T.; Zondervan, G. J. *J. Catal.* **1965,** *4,* 649–653. doi:10.1016/0021-9517(65)90264-2

License and Terms

The definitive version of this article is the electronic one which can be found at:
doi:10.3762/bjnano.2.13

Beilstein Journal
of Nanotechnology

Novel acridone-modified MCM-41 type silica: Synthesis, characterization and fluorescence tuning

Maximilian Hemgesberg[1], Gunder Dörr[1], Yvonne Schmitt[1], Andreas Seifert[2], Zhou Zhou[3], Robin Klupp Taylor[4], Sarah Bay[5], Stefan Ernst[1], Markus Gerhards[1], Thomas J. J. Müller[5] and Werner R. Thiel*[1]

Full Research Paper

Address:
[1]TU Kaiserslautern, Fachbereich Chemie, Erwin-Schrödinger-Straße 52–54, D-67653 Kaiserslautern, Germany, [2]TU Chemnitz, Institut für Chemie, Straße der Nationen 62, D-09111 Chemnitz, Germany, [3]Friedrich-Alexander-Universität Erlangen-Nürnberg, Erlangen Catalysis Resource Center (ECRC), Egerlandstraße 3, D-91058 Erlangen, Germany, [4]Friedrich-Alexander-Universität Erlangen-Nürnberg, Institut für Partikeltechnologie, Cauerstraße 4, D-91058 Erlangen, Germany and [5]Heinrich-Heine-Universität Düsseldorf, Institut für Organische Chemie und Makromolekulare Chemie, Universitätsstraße 1, D-40225 Düsseldorf, Germany

Email:
Werner R. Thiel* - thiel@chemie.uni-kl.de

* Corresponding author

Keywords:
acridone; co-condensation; fluorescence; scandium; MCM-41

Beilstein J. Nanotechnol. **2011,** *2,* 284–292.
doi:10.3762/bjnano.2.33

Received: 21 March 2011
Accepted: 12 May 2011
Published: 09 June 2011

This article is part of the Thematic Series "Micro- and mesoporous solids: From science to application"

Guest Editor: J. J. Schneider

Abstract

A Mobil Composition of Matter (MCM)-41 type mesoporous silica material containing *N*-propylacridone groups has been successfully prepared by co-condensation of an appropriate organic precursor with tetraethyl orthosilicate (TEOS) under alkaline sol–gel conditions. The resulting material was fully characterized by means of X-ray diffraction (XRD), N_2-adsorption–desorption, transmission electron microscopy (TEM), IR and UV–vis spectroscopy, as well as ^{29}Si and ^{13}C CP-MAS NMR techniques. The material features a high inner surface area and a highly ordered two-dimensional hexagonal pore structure. The fluorescence properties of the organic chromophore can be tuned via complexation of its carbonyl group with scandium triflate, which makes the material a good candidate for solid state sensors and optics. The successful synthesis of highly ordered MCM materials through co-condensation was found to be dependent on the chemical interaction of the different precursors.

Introduction

Mesoporous silicates are widely used for a variety of applications such as gas storage and heterogeneous catalysis, e.g., the synthesis of ε-caprolactam [1], or the decomposition of nitrous oxides [2]. MCM-41, MCM-48 and other silica materials can normally be functionalized either by in situ post-sol–gel modification or by direct co-condensation of different types of organic precursors [3]. The latter method often leads to a more homogeneous distribution of the desired functionalization within the material. It also provides the possibility to characterize application-tailored sol–gel precursors prior to implementing them into the solid, thus increasing the depth of information compared to the data solely drawn from solid state measurements.

Focusing on the synthesis of novel inorganic–organic hybrid materials, we also investigated new ways to produce trialkoxysilanes bearing polycyclic aromatic compounds as terminal groups, Ar–$(CH_2)_n$–$Si(OR)_3$ (n = 3, R = Me, Et), which may lead to interesting optical or electronic properties [4-6]. Acridone, being a well-known fluorophore used, e.g., for chemosensors [7], has previously been reported to be suitable for the pK_a determination of lanthanide salts in aqueous solution, the fluorescence undergoing a bathochromic shift directly correlated to the acidity of the cation bound to its carbonyl group [8]. We therefore sought to create a micro- or mesoporous material containing covalently bound acridone units that would serve the same purpose, by choosing the amino function of acridone as the functional group to be modified. Trialkoxysilanes with a variety of functional groups have already been prepared by *N*-alkylation of amines using 3-iodopropyltrimethoxysilane (IPTMS) [9] or 3-bromopropyltrimethoxysilane (BPTMS) [10], by sulfamidation [11], by imide [12] or via imine forming reactions [13] using 3-aminopropyltriethoxysilane (APTES). In 2009, an *N*-alkylated acridone derivative bearing a (tri-isopropyloxysilyl)propyl group and its application as an anion-selective fluorescent probe were reported by Lin and Chen [14]. However, to the best of our knowledge, up to now, no MCM-like material featuring covalently bound acridone units has been described.

Results and Discussion

Compound **1** was prepared in a two-step sequence (Scheme 1): Following a published procedure, acridone was obtained from commercially available *N*-phenylanthranilic acid by an acid catalyzed ring closure reaction [15]. To attach the silyl functionalized linker, acridone was deprotonated by NaH and the resulting anion reacted with 3-iodopropyltrimethoxysilane (IPTMS).

Co-condensation of TEOS with organosilanes in the presence of an appropriate structure-directing template allows the direct and homogeneous incorporation of organic functionalities into a mesoporous material. Applying this method, we were recently able to introduce up to 30 wt % of redox-active phenothiazines into mesostructured silicas [4-6]. The resulting materials showed a continuous decrease of ordering with increasing bulk of the organic groups, although all exhibited very high specific surface areas. As the formation of micelles will strongly depend on the nature of the organic molecule and its concentration, it was decided to keep the amount of precursor **1** at 10 mol % with respect to TEOS in order to be sure that a highly ordered material would be obtained. The MCM-41 analogue was prepared by a modified synthesis previously reported by Pang et al. [15], in which aqueous ethylamine is used in order to adjust smoothly the pH-value of the solution. Given the fact that polycyclic compounds are rather bulky organic moieties which might behave differently when undergoing a sol–gel transformation, a slightly larger molecule (stearyltrimethylammonium bromide, $C_{18}TAB$) was chosen as the templating agent.

However, obtaining materials with high surface areas has previously been shown to be also dependent on the boiling point of the sol–gel solution. Thus, the addition of larger amounts of volatile organic solvents such as THF to the aqueous phase often prevents the formation of highly ordered mesoporous structures [16]. On the other hand, the π-stacking of large aromatics generally causes them to be less readily dissolved and requires larger amounts of solvents, which are mostly immiscible with water. Therefore, pure TEOS was tested as a mediating agent for introduction into the sol–gel process. It turned out to be beneficial for the co-condensation process that precursor **1** could be mixed with TEOS rather easily, although it did not prove possible to obtain a homogeneous solution. Despite the fact that it was rather difficult to handle by syringe, a mixture of TEOS and **1** could be converted to the corresponding mesostructured silica **MCM-ACR**.

In contrast to **1**, a similar compound prepared from pyrenesulfonyl chloride and APTES via sulfamidation immediately yielded a flocculent precipitate when brought in contact with

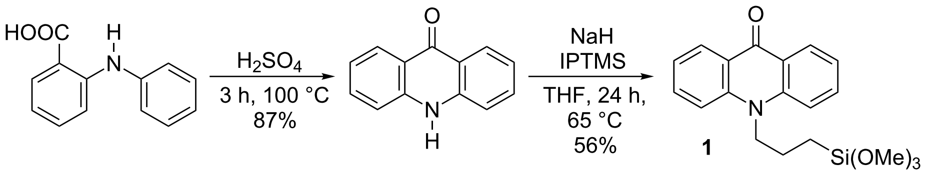

Scheme 1: Synthesis of the sol–gel precursor **1**.

TEOS. This observation might be explained by the combination of the pyrene moieties, forming strong π-bonding interactions, and the highly polar hydrogen bonding sulfonamide, causing the compound to become inhomogeneous in TEOS. As expected, the material obtained from the pyrene precursor showed a drastically decreased inner surface area of only 322 $m^2 \cdot g^{-1}$ and no ordered material structure at all.

The CHNS analysis of **MCM-ACR** clearly indicates a slightly increased ratio between the dye and silica (1:7.5) compared to the initial ratio of the synthesis (1:9), probably resulting from different rates of hydrolysis of TEOS and the $RSi(OMe)_3$ groups. Converting the materials' molecular composition to the amount of *N*-propylacridone moieties per gram, we obtained a dye loading of approximately 240 $mg \cdot g^{-1}$.

From the infrared spectra of **1** and both the unmodified as well as the modified **MCM-ACR**, the aromatic and aliphatic C–H vibrational bands around 3000 cm^{-1} showed reduced intensities in the solid and were mostly covered by the weak, yet broad, absorption bands of the silanol groups and bands from water trapped in the silica framework (Figure 1).

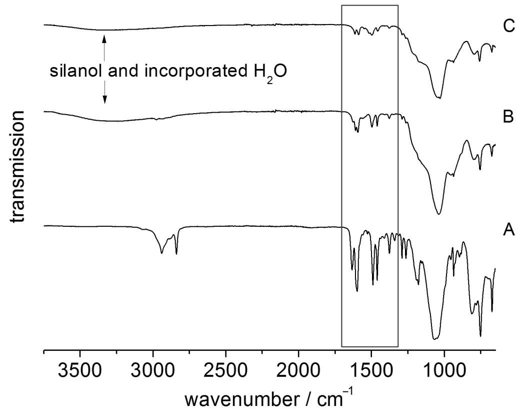

Figure 1: Infrared spectra of compound **1** (A), **MCM-ACR** (B) and **MCM-ACR** + $Sc(OTf)_3$ (C). The box marks the section given in Figure 2 (resolution ±2 cm^{-1}).

The spectra were also found to be in accordance with the interpretation of the infrared spectrum of free acridone reported earlier by Berezin et al. [17]. By comparing the region between $\tilde{\nu}$ = 1700 cm^{-1} and 1300 cm^{-1}, complex formation with the scandium(III) cation is clearly observed. The infrared absorption of the C=O vibrational band (precursor **1**: 1630 cm^{-1}, *N*-methylacridone: 1630 cm^{-1} [18]) shifts slightly to lower wavenumbers (Figure 2) after the immobilization, and also splits into two resonances (**MCM-ACR**: 1625 cm^{-1}, 1609 cm^{-1}) indicating an interaction of the carbonyl group with Lewis or Brønsted acidic or with hydrogen-bond-donating surface sites, which has previously been described for fluorescent probes such as Michler's ketone [19]. This again changes after the reaction with $Sc(OTf)_3$: A single C=O absorption emerges at 1613 cm^{-1}. The redshift of the absorption frequency is conclusive with respect to the weakened C=O double bond caused by the electron donation from the carbonyl unit to the scandium(III) cation, which is also evident in the UV–vis absorption of **MCM-ACR** (see below in Figure 9).

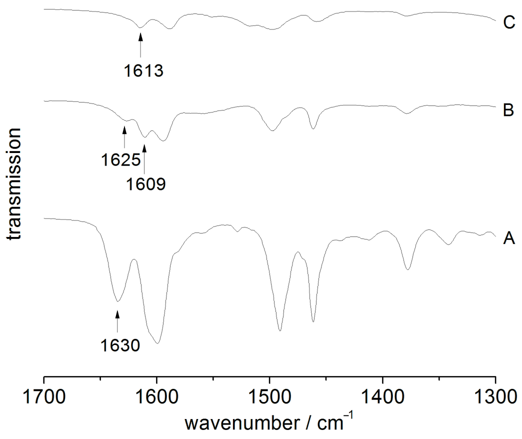

Figure 2: C=O vibrational band section of the infrared spectra of compound **1** (A), **MCM-ACR** (B) and **MCM-ACR** + $Sc(OTf)_3$ (C).

According to the TEM analysis (Figure 3) and BET measurements (Figure 4), the sol–gel process yielded a well ordered mesoporous material with a total surface area of up to 810 $m^2 \cdot g^{-1}$, exhibiting a characteristic pore size distribution with a sharp peak around 2.4 nm. The XRD spectrum reveals the expected peak patterns only for the (110) and (200) Miller indices as the (100) peak is not distinguishable from the primary beam (Figure 5). BET data of an authentic MCM-41 sample previously prepared in our group corresponded to a total surface area of 1122 $m^2 \cdot g^{-1}$, so the experimental value for **MCM-ACR** is in accordance with our expectations. Table 1 summarizes the values obtained for the described MCM-41-sample as well as for both Sc(III)-free and Sc(III)-containing **MCM-ACR**.

The type IV BET isotherms of the material exhibit a large slope in the N_2 uptake only at lower p/p_0 ratios, and they show no significant sorption hysteresis. We may therefore conclude that the silica obtained has a very uniform structure and a homogeneous composition, thus proving that the co-condensation could be carried out in a controllable way, and that the formation of larger mesopores was prevented in the presence of the organic precursor in spite of its rather bulky nature.

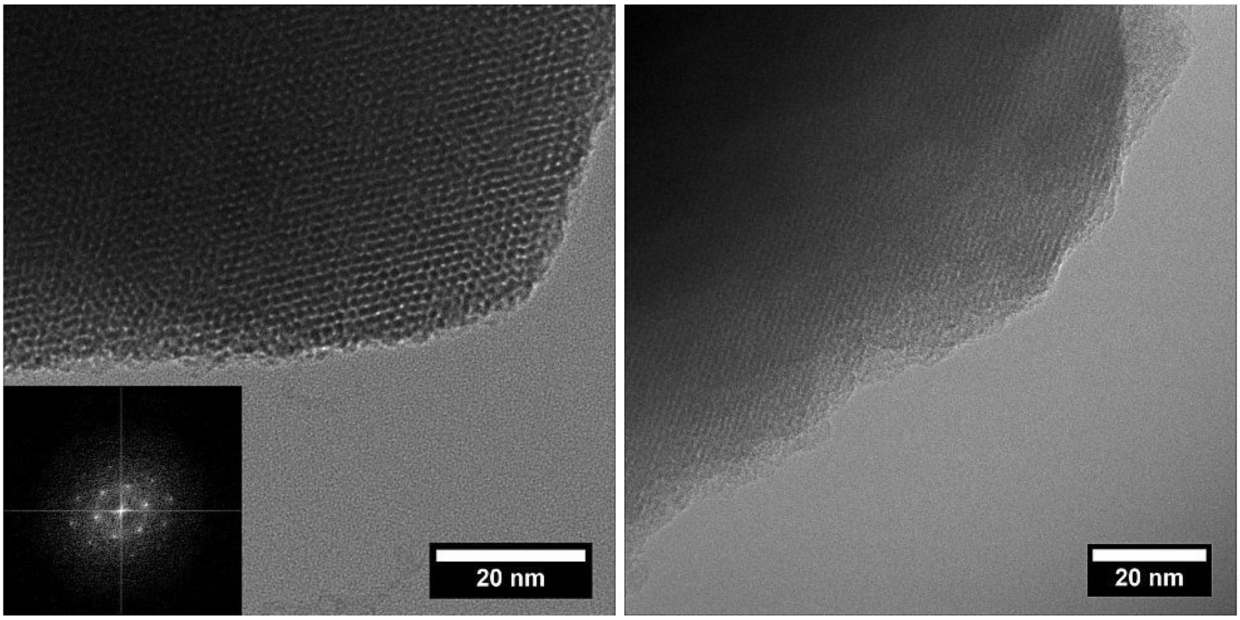

Figure 3: TEM images showing the mesoporous structure of **MCM-ACR** (left: frontal, right: lateral), inset in left image: Electron diffraction pattern.

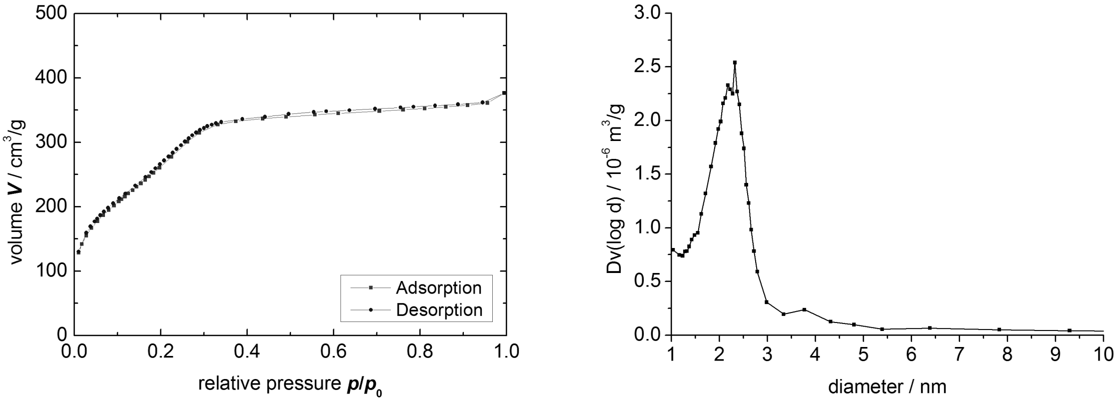

Figure 4: Sorption isotherm (left) and pore size distribution (BJH plot) (right) of **MCM-ACR**.

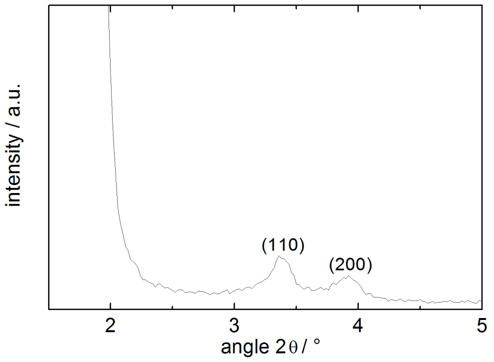

Figure 5: XRD pattern of **MCM-ACR**.

The ^{13}C CP-MAS NMR spectrum of **MCM-ACR** (Figure 6) shows the expected signals for the three methylene groups of the propyl chain as well as for the acridone moieties. Minor impurities in the spectrum of the precursor are mostly due to hydrolysis occurring during the measurement. The two prominent sharp alkyl peaks in the solid state spectrum may be attributed to the remaining free EtOH within the silicate. The ^{29}Si CP-MAS NMR data of **MCM-ACR** (Figure 7) prove that the material features the expected distribution of T- and Q-peaks. The minor T_2-peak at −57 ppm can be ascribed to the $R_{alkyl}Si(OMe)(OSi)_2$ unit resulting from the partially incomplete incorporation of the precursor's anchoring group into the framework [20].

Table 1: BET and PSD date of different obtained mesoporous siliceous materials. In the case of **MCM-ACR**, two batches have been prepared with well reproducible outcomes (second batch in parentheses). The modified **MCM-ACR** sample was prepared from the first batch with a BET surface area of 775 $m^2 \cdot g^{-1}$.

type of material	BET surface [$m^2 \cdot g^{-1}$]	Langmuir surface [$m^2 \cdot g^{-1}$]	average pore diameter [nm]
MCM-41	1122	2346	2.4
MCM-ACR	775 (810)	1135 (1661)	2.4
MCM-ACR + $Sc(OTf)_3$	734	962	2.3

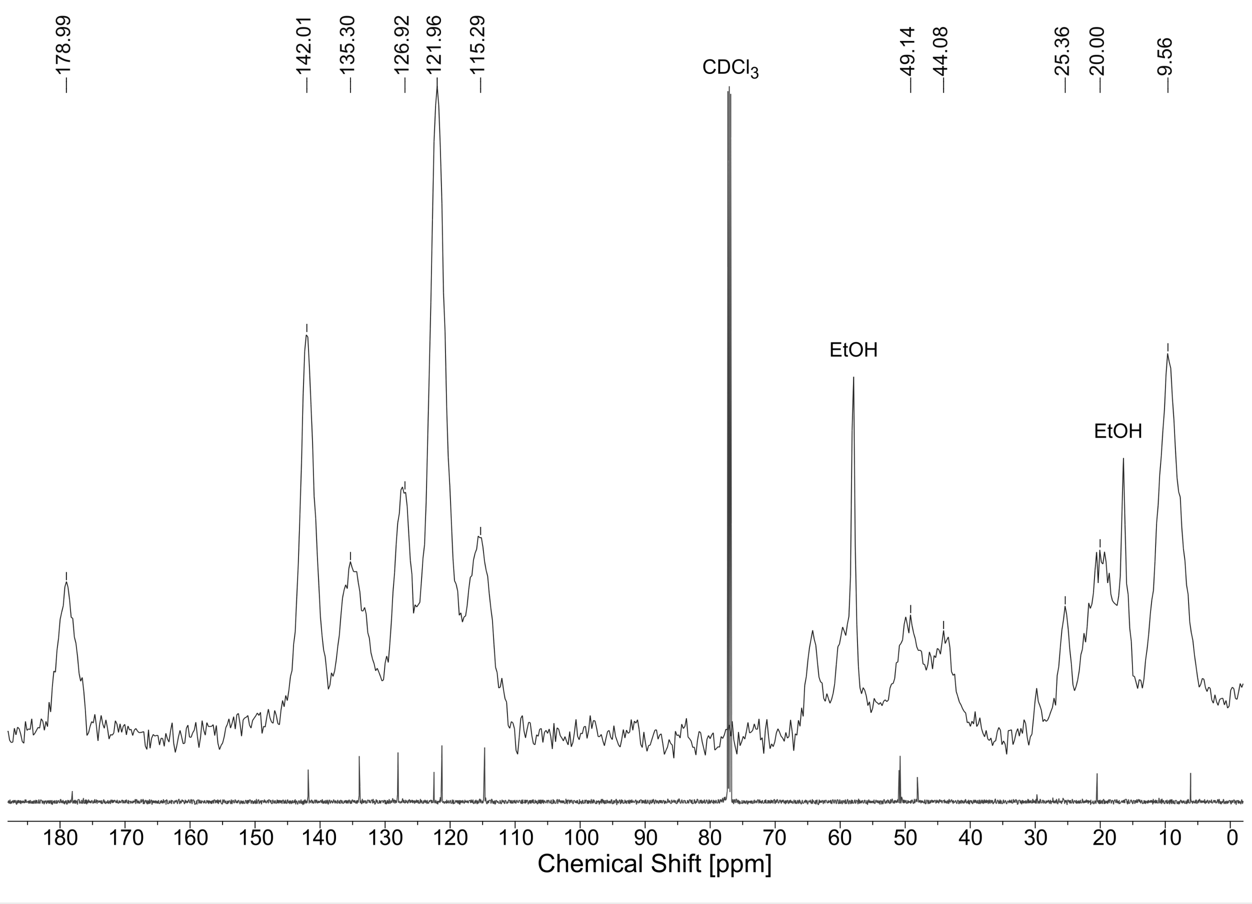

Figure 6: ^{13}C CP-MAS NMR spectrum of **MCM-ACR** overlaid with the high resolution ^{13}C NMR spectrum of precursor **1** (recorded in $CDCl_3$).

When studying the fluorescence properties of the materials obtained before and after the post-sol–gel modification, an instantaneous shift in color and fluorescence was observed when **MCM-ACR** and the scandium(III) triflate solution were combined. Compound **1**, as well as unmodified **MCM-ACR**, feature a clear blue fluorescence when excited at a wavelength of $\lambda_{ex.} = 366$ nm, whereas the complex formation with the scandium cation results in an intensely yellow colored product showing a greenish fluorescence (Figure 8). This effect is also clearly evident in the UV–vis and fluorescence spectra (Figure 9). Introduction of scandium(III) into the material yields a bathochromic effect in $\lambda_{abs.}$ and $\lambda_{em.}$ of about 20 nm and, more interestingly, a significantly increased absorption at around $\lambda_{abs.} = 328$ nm. The appearance of this distinct absorption may hint towards an electron transfer (LMCT) from the molecular orbital located at the carbonyl oxygen to the empty 3d orbital residing at the Sc(III) cation, a process which would be similar to those that have been described for carboxylate complexes of Eu(III) [21]. The fluorescence spectrum of the modified silica shows a distinct shoulder at around $\lambda_{em.} \approx 515$ nm. This indicates a complex radiative relaxation of the formed transition metal species, the fluorescence originating from at least two different transitions between the excited electronic states and the ground state. A reason for this

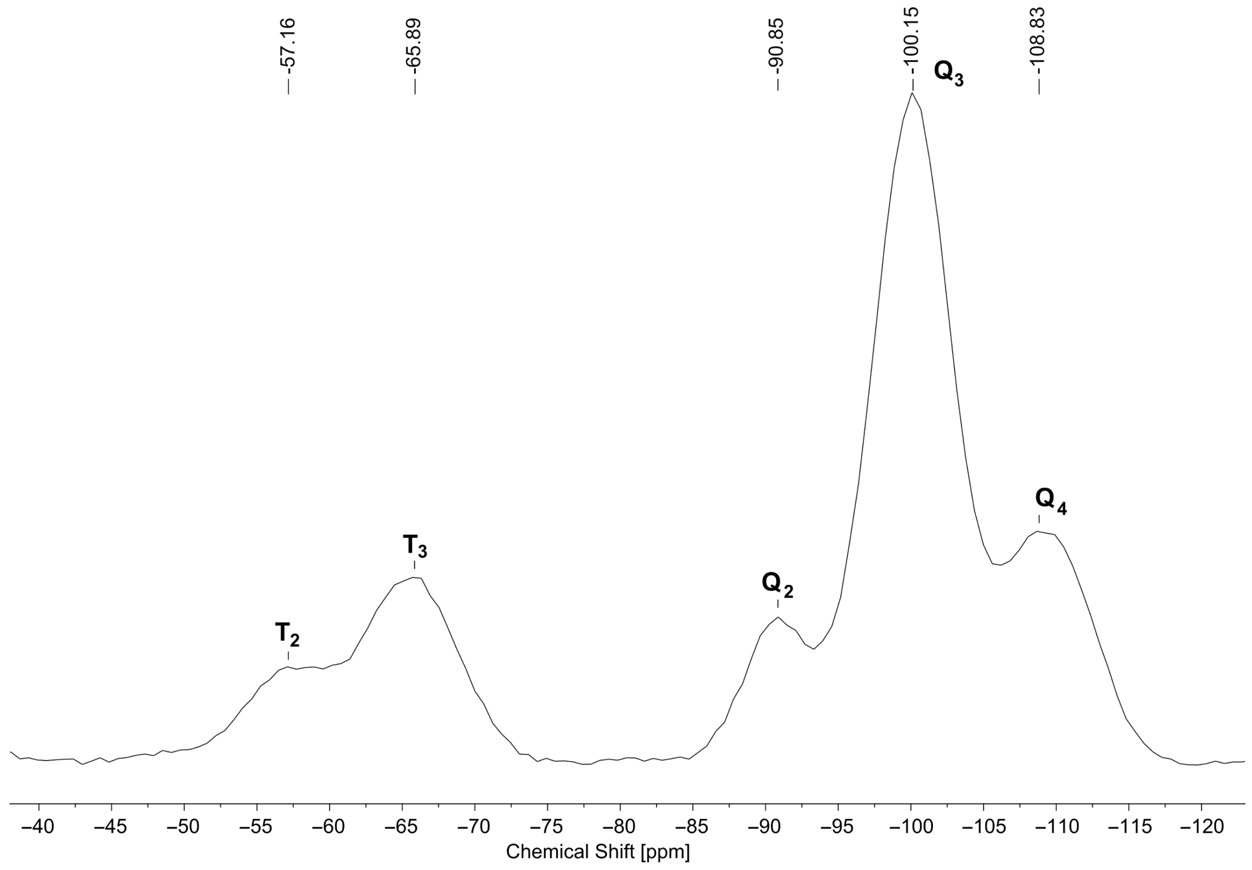

Figure 7: ^{29}Si CP-MAS NMR spectrum of **MCM-ACR**.

phenomenon might be the energy splitting caused by the coupled CO stretching within the acridone–Sc^{3+} complex [7]. The pure triflate is almost completely transparent in the UV–vis region and shows no fluorescence when measured both as a solid film and in solution, hence it is obvious that the optical properties of the material depend on the electronic structure of the acridone chromophore, the latter being significantly changed via formation of the complex as the scandium(III) ion strongly interacts with the oxygen atom of the C=O functional group. The complex itself seems to be very stable and inert to ligand exchange: Excessive washing with polar organic solvents and storing of an authentic sample for weeks, and even months, neither altered the appearance of the material nor decreased its fluorescence intensity.

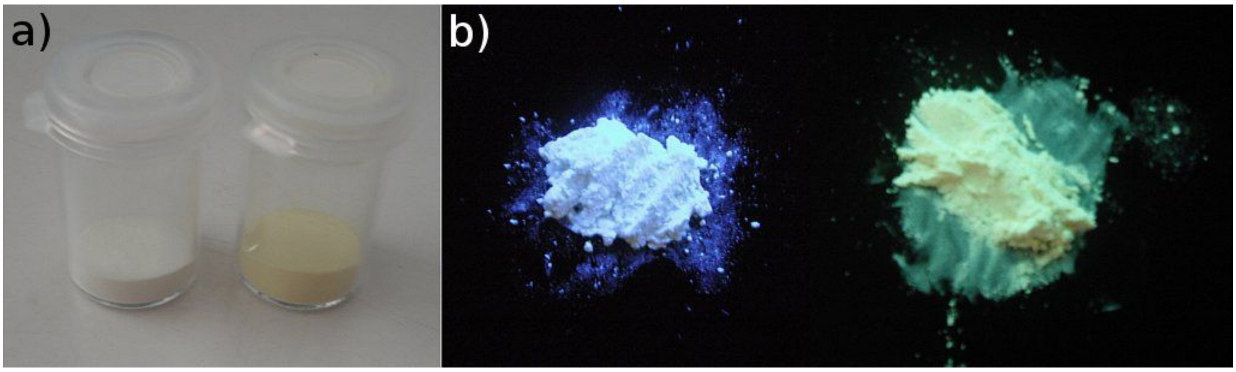

Figure 8: Visual appearance of **MCM-ACR** and **MCM-ACR** + Sc(OTf)$_3$ under normal (a) and UV light (b).

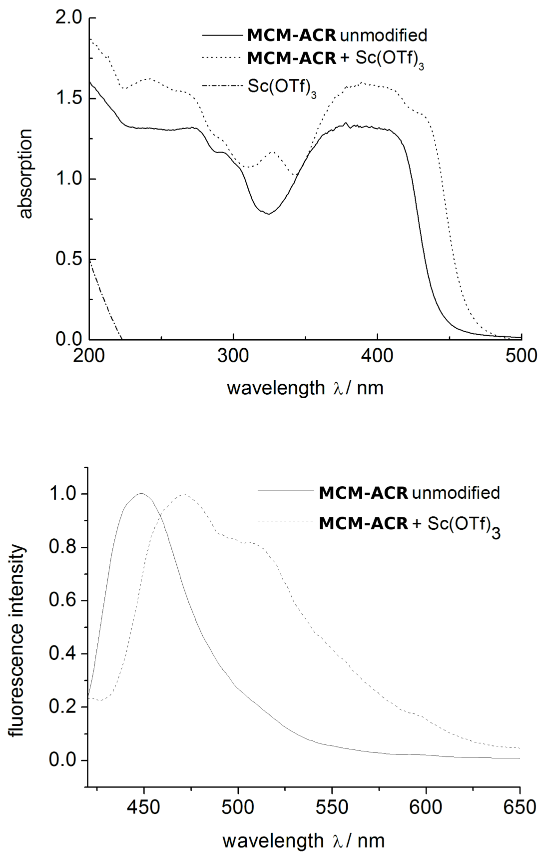

Figure 9: Overlay of the solid state UV-vis (top) and fluorescence (bottom) spectra of **MCM-ACR**, **MCM-ACR** + $Sc(OTf)_3$ and pure $Sc(OTf)_3$ (fluorescence excitation wavelength $\lambda_{ex.}$ = 400 nm). UV–vis-absorption intensities are not normalized to a given value; fluorescence has been normalized to an intensity of 1.0. $Sc(OTf)_3$ shows no significant fluorescence and therefore was omitted in the second diagram.

Conclusion

We have presented a novel fluorescent organosilane bearing an acridone fluorophore and its successful transformation into a MCM-41 type material via co-condensation with TEOS. As predicted, the hybrid material shows a change in its fluorescence properties when non-covalently modified through scandium complex formation. The miscibility of the organic precursor or its concentrated solution with an excess of the major silicon source has been determined to be crucial for the synthesis of the hybrid material given herein. Possibilities to vary the dye content by using different molar ratios of the precursors in the sol–gel process are to be investigated in the near future. Furthermore, efforts will be made to elucidate the optical properties of the materials after doping with lanthanides or heavy metal cations, e.g. Eu(III), Er(III) or Bi(III).

Experimental

General: All starting materials described herein were purchased from Sigma-Aldrich and used as received. Solvents for the organic syntheses were dried prior to use according to standard procedures [22]. Solid-state ^1H CP-MAS, ^{29}Si CP-MAS and ^{13}C CP-MAS NMR spectra were recorded on a Bruker DSX Avance NMR spectrometer at resonance frequencies of 400 MHz, 101 MHz and 80 MHz for ^1H, ^{13}C or ^{29}Si nuclei, respectively. Liquid phase ^1H and ^{13}C NMR spectra were recorded on Bruker Spectrospin DPX-400 and Avance 600 devices at resonance frequencies of 400 MHz or 151 MHz for ^1H or ^{13}C nuclei, respectively. These spectra are internally referenced to $SiMe_4$. The infrared spectra with a resolution of $\pm 2\ cm^{-1}$ were recorded using a PerkinElmer FT-ATR-IR 1000 spectrometer containing a diamond coated ZnSe-window. MALDI-ToF measurements were conducted on a Bruker Daltonics Ultraflex spectrometer. Elemental analyses were determined on a CHNS vario Microcube elemental analyzer (Elementar). X-ray powder diffraction (PXRD) patterns of the silica samples were recorded on a Siemens D5005 instrument using Ni-filtered Cu Kα radiation (λ = 1.5404 Å), with a step size of 1 °/min. N_2-Adsorption–desorption isotherms, pore size distributions as well as the textural properties of the hybrid materials were determined at 77 K by a Quantachrome Autosorb 1 sorption analyzer. Before analysis, the samples were activated at 120 °C overnight in the vacuum and then the adsorption–desorption procedure was conducted by passing nitrogen into the sample, which was kept under liquid nitrogen. The average pore size of the samples was estimated using the BJH approach based on the Kelvin equation while assuming a cylindrically shaped porous structure. The specific surface areas were calculated by means of the Brunauer–Emmett–Teller (BET) equation in the low relative pressure interval (<0.3) and the pore size distribution curves were analyzed with the adsorption branch by the BJH method. The morphology of the mesoporous particles was determined by a Philips CM 300 UT field emission transmission electron microscope (TEM) with 300 kV acceleration voltage and 0.17 nm point resolution. The UV–vis absorption and fluorescence of the precursor were measured using a Perkin–Elmer Lambda 900 and a Horiba Jobin–Yvon Fluorolog 3-22 τ in steps of 0.1 nm and 1.0 nm, respectively, the SiO_2-cuvettes used had a width of 1.0 cm. Solid state UV–vis measurements were carried out on a Perkin–Elmer Lambda 18 double beam UV–vis spectrometer with double monochromator by setting the wavelength range from 200 nm to 900 nm in a 1 nm step width. The optical unit included a prealigned tungsten-halogen lamp and a deuterium lamp with automatic source exchange. All powder samples were calibrated with a diffuse $BaSO_4$ referenced auto zero and were measured using a Biconical (Praying Mantis) Diffuse Reflectance Accessory in reflecting absorption mode. Solid state fluorescence data was recorded on a Perkin-Elmer LS55 with a step width of 0.5 nm. The thin film powder samples were prepared from a DCM suspension or solution by evaporation of the solvent on a glass substrate.

10-(Trimethoxysilylpropyl)acridin-9(10H)-one (1): Finely powdered dry acridone [23] (5.85 g, 30.0 mmol) was added portionwise to a stirred suspension of 1.1 equiv of sodium hydride (800 mg, 33.3 mmol) in dry THF (100 mL). The resulting yellow-greenish suspension was stirred for 15 min at 25 °C until the hydrogen evolution subsided. Subsequently, 1.1 equiv of 3-iodopropyltrimethoxysilane (9.67 g, 6.53 mL, 33.3 mmol) were added dropwise via a syringe through a rubber septum. The golden colored suspension was heated to reflux for 24 h before evaporation of the solvent. The residue was washed with dry pentane (3 × 10 mL), then re-dissolved in several portions of dichloromethane (total of 150 mL) and the combined organic solutions were filtered. Evaporation of the solvent gave **1** as a highly viscous orange oil (16.9 mmol, 6.77 g, 56%) showing a strong blue–green fluorescence under UV light. ^{1}H NMR (400 MHz, $CDCl_3$) δ 8.61 (d, $^3J_{HH}$ = 7.9 Hz, 2H), 7.76 (t, $^3J_{HH}$ = 7.8 Hz, 2H), 7.59 (d, $^3J_{HH}$ = 8.7 Hz, 2H), 7.32 (t, $^3J_{HH}$ = 7.5 Hz, 2H), 4.51–4.34 (m, 2H), 3.67 (s, 9H), 2.22–2.01 (m, 2H), 0.89 (t, $^3J_{HH}$ = 7.7 Hz, 2H); ^{13}C NMR (151 MHz, $CDCl_3$) δ 178.0, 141.8, 133.9, 127.9, 122.4, 122.2, 114.6, 50.8, 48.1, 20.4, 6.1; ATR-IR (ZnSe) $\tilde{\nu}$ [cm^{-1}]: 2940, 2840, 1635, 1599, 1491, 1462, 1378, 1342, 1291, 1264, 1169, 1045, 956, 937, 897, 810, 753, 673; MALDI-ToF for $C_{19}H_{23}NO_4Si$ (matrix CHCA, M^+): 356.6; UV–vis (CH_2Cl_2, $c \approx 10^{-6}$ M) $\lambda_{abs.}$ = 254, 381, 400 nm; Fluorescence (CH_2Cl_2, $c \approx 10^{-6}$ M, $\lambda_{ex.}$ = 250 nm): $\lambda_{em.}$ = 415, 431 nm.

Acridone functionalized hybrid silica material (MCM-ACR): The molar ratio of the different sol–gel components was determined in advance to be 9.0:1.0:24.0:1.4:1000 (TEOS:precursor **1**:base:C_{18}TAB:H_2O). In order to achieve a homogeneous co-condensation, the organic precursor ideally had to be dissolved prior to hydrolysis. An aqueous 70 wt % solution of H_2NEt (12.2 g, 190 mmol) was introduced into a stirred solution of C_{18}TAB (4.35 g, 11.1 mmol) in deionized water (142 mL). A two-phase mixture consisting of TEOS (14.8 g, 15.7 mL, 71.0 mmol) and **1** (3.15 g, 8.82 mmol) was rapidly added at 25 °C by syringe under vigorous stirring. The milky yellow solution, which soon contained a precipitate, was stirred at room temperature for 5 h before being heated to 100–110 °C (bath temperature) for a further 16 h. The resulting hot suspension was filtered, washed thoroughly with deionized water (a total amount of 1 L) and the solid residue was re-suspended in a 1:8 mixture of ethanol and concentrated HCl (200 mL). C_{18}TAB was extracted by stirring for 16 h at 85 °C. The obtained solid was filtered from the hot solution, washed with EtOH (500 mL) and dried in the vacuum to give the product as a pale yellow, very fine powder (6.60 g, 7.76 mmol according to a calculated molecular weight of 835.7 g·mol^{-1}). CHNS analysis found: C 21.25, H 3.56, N 1.66; calcd. for $(C_{16}H_{14}NO_{2.5}Si)\cdot(H_2O)_9\cdot(SiO_2)_{7.5}$: C 21.33, H 3.48, N 1.55. This gives a CHN content of approx. 24 wt % (related to the *N*-propylacridone moiety).

Post-sol–gel modification of MCM-ACR: Introduction of the scandium salt into the material was realized by stirring **MCM-ACR** (500 mg) in a 0.01 M solution of scandium(III) triflate in ethanol or acetonitrile (25 mL) for 16 h. The modified materials were thoroughly washed with ethanol or acetonitrile (5 × 5 mL) and water (5 × 5 mL) prior to drying and characterization.

Acknowledgements

We gratefully thank the Konrad-Adenauer-Stiftung (KAS) for funding the Ph. D. thesis of M. H. and the Carl-Zeiss-Stiftung for the financial support of Y. S. .

References

1. Wang, X.; Chen, C.-C.; Chen, S.-Y.; Mou, Y.; Cheng, S. *Appl. Catal., A* **2005,** *281,* 47–54. doi:10.1016/j.apcata.2004.11.011
2. Hu, Y.; Higashimoto, S.; Martra, G.; Zhang, J.; Matsuoka, M.; Coluccia, S.; Anpo, M. *Catal. Lett.* **2003,** *90,* 161–163. doi:10.1023/B:CATL.0000004111.02392.75
3. Corma, A. *Chem. Rev.* **1997,** *97,* 2373–2420. doi:10.1021/cr960406n
4. Zhou, Z.; Franz, A. W.; Hartmann, M.; Seifert, A.; Müller, T. J. J.; Thiel, W. R. *Chem. Mater.* **2008,** *20,* 4986–4992. doi:10.1021/cm800804t
5. Franz, A. W.; Zhou, Z.; Turdean, R.; Wagener, A.; Sarkar, B.; Hartmann, M.; Ernst, S.; Thiel, W. R.; Müller, T. J. J. *Eur. J. Org. Chem.* **2009,** 3895–3905. doi:10.1002/ejoc.200900332
6. Zhou, Z.; Franz, A. W.; Bay, S.; Sarkar, B.; Seifert, A.; Yang, P.; Wagener, A.; Ernst, S.; Pagels, M.; Müller, T. J. J.; Thiel, W. R. *Chem.–Asian J.* **2010,** *5,* 2001–2015. doi:10.1002/asia.201000098
7. Bahr, N.; Tierney, E.; Reymond, J.-L. *Tetrahedron Lett.* **1997,** *38,* 1489–1492. doi:10.1016/S0040-4039(97)00137-8
8. Fukuzumi, S.; Ohkubo, K. *J. Am. Chem. Soc.* **2002,** *124,* 10270–10271. doi:10.1021/ja026613o
9. Cejas, M. A.; Raymo, F. M. *Langmuir* **2005,** *21,* 5795–5802. doi:10.1021/la0502793
10. Sambhy, V.; Peterson, B. R.; Sen, A. *Langmuir* **2008,** *24,* 7549–7558. doi:10.1021/la800858z
11. Biazzotto, J. C.; Sacco, H. C.; Ciu, K. J.; Neri, C. R.; Ferreira, A. G.; Iamamoto, Y.; Serra, O. A. *J. Non-Cryst. Solids* **1999,** *247,* 134–140. doi:10.1016/S0022-3093(99)00050-2
12. Schneider, M.; Müllen, K. *Chem. Mater.* **2000,** *12,* 352–362. doi:10.1021/cm9910613
13. Lam, M. H. W.; Lee, D. Y. K.; Man, K. W.; Lau, C. S. W. *J. Mater. Chem.* **2000,** *10,* 1825–1828. doi:10.1039/b001914n
14. Lin, Y.-C.; Chen, C.-T. *Org. Lett.* **2009,** *11,* 4858–4861. doi:10.1021/ol901935g
15. Lin, W.; Cai, Q.; Pang, W.; Yue, Y. *Chem. Commun.* **1998,** 2473–2474. doi:10.1039/a807786j

16. Furukawa, H.; Takeuchi, S.; Moriguchi, I.; Teraoka, Y.; Kagawa, S. *Nippon Kagakkai Koen Yokoshu* **1998,** *75,* 284. http://sciencelinks.jp/j-east/article/199907/000019990799A0248134.php
17. Berezin, K. V.; Krivokhizhina, T. V.; Nechaev, V. V. *Opt. Spectrosc.* **2006,** *100,* 15–22. doi:10.1134/S0030400X0601005X
18. Spectral Database for Organic Compounds SDBS, National Institute of Advanced Industrial Science and Technology (AIST). http://www.aist.go.jp/ (accessed Feb 11, 2011).
19. Spange, S.; Zimmermann, Y.; Gräser, A. *Chem. Mater.* **1999,** *11,* 3245–3251. doi:10.1021/cm990308t
20. Bein, T.; Carver, R. F.; Farlee, R. D.; Stucky, G. D. *J. Am. Chem. Soc.* **1988,** *110,* 4546–4553. doi:10.1021/ja00222a010
21. An, B.-L.; Gong, M.-L.; Cheah, K.-W.; Zhang, J.-M.; Li, K.-F. *Chem. Phys. Lett.* **2004,** *385,* 345–350. doi:10.1016/j.cplett.2003.12.093
22. Riddick, J. A.; Bunger, W. B.; Sakano, T. K. *Organic Solvents: Physical Properties and Methods of Purification,* 4th ed.; Wiley: New York, 1986.
23. Allen, C. F. H.; McKee, G. H. W. *Organic Syntheses, Coll. Vol. 2* **1943,** 15. http://www.orgsyn.org/orgsyn/prep.asp?prep=cv2p0015

License and Terms

Beilstein Journal
of Nanotechnology

Ceria/silicon carbide core–shell materials prepared by miniemulsion technique

Lars Borchardt[1], Martin Oschatz[1], Robert Frind[1], Emanuel Kockrick[1],
Martin R. Lohe[1,2], Christoph P. Hauser[3], Clemens K. Weiss[3],
Katharina Landfester[3], Bernd Büchner[2] and Stefan Kaskel*[1]

Full Research Paper

Address:
[1]Department of Inorganic Chemistry, Dresden University of Technology, Bergstrasse 66, D-01062 Dresden, Germany, [2]Leibniz Institute for Solid State and Materials Research Dresden (IFW Dresden), Institute for Solid State Research, Helmholtzstrasse 20, 01069 Dresden, Germany and [3]Max Planck Institut für Polymerforschung, Ackermannweg 10, D-55128 Mainz, Germany

Email:
Lars Borchardt - lars.borchardt@chemie.tu-dresden.de;
Stefan Kaskel* - stefan.kaskel@chemie.tu-dresden.de

* Corresponding author

Keywords:
ceria; cerium dioxide; core shell; miniemulsion; oxycarbide; silicon carbide; TPO catalytic

Beilstein J. Nanotechnol. **2011,** *2,* 638–644.
doi:10.3762/bjnano.2.67

Received: 31 May 2011
Accepted: 25 August 2011
Published: 27 September 2011

This article is part of the Thematic Series "Micro- and mesoporous solids: From science to application".

Guest Editor: J. J. Schneider

Abstract

For the first time we present the synthesis of CeO_2/Si(O)C core–shell particles prepared by the miniemulsion technique. The Si(O)C core was obtained by means of a polycarbosilane precursor (SMP10), which was subsequently functionalized with ceria and pyrolyzed to the ceramic. The size of these particles could easily be adjusted by varying the surfactants and the surfactant concentration, or by the addition of comonomers. Hence particle sizes ranged from 100 to 1000 nm, tunable by the preparation conditions. All materials were characterized by photon cross correlation spectroscopy, scanning electron microscopy and elemental mapping investigations. Furthermore, first catalytic tests were carried out by temperature programmed oxidation (TPO) of methane, and the activity of this material in lowering the onset temperature of methane combustion by 262 K was documented.

Introduction

In recent years miniemulsions have been studied intensively [1-3]. Polymeric nanoparticles [1,2] from homo- or copolymers [3] as well as hybrid materials [3,4] such as magnetic [5-8] or silica/polymer nanoparticles [9,10] have been synthesized by this approach. The size of the generated particles can easily be controlled [11,12] through the amount of surfactant added to the system, allowing particle sizes usually in the range of 50–500 nm and with a narrow size distribution. Hydrophobic polymeric particles are usually prepared from a direct (oil-in-water) miniemulsion, with the monomer as the dispersed oil phase. The nanodroplets are generated by shearing this system with ultrasound. A highly hydrophobic osmotic pressure agent (costabilizer) is added to the oil phase, effectively suppressing diffusional degradation (Ostwald ripening) of the droplets.

Thus, the droplet sizes and the composition of the droplet components remain unchanged. This, in consequence, enables the preparation of copolymer particles of defined composition and the encapsulation of further, monomer soluble materials [4]. For the preparation of inorganic, ceramic materials usually the inverse miniemulsion technique has to be applied. Here, water soluble precursor compounds (e.g., Ti- or Si-glycolates, Zr or Ce-salts) for sol–gel synthesis and, if desired, templating surfactants, such as CTAB, are dissolved in water, acting as the dispersed phase. After miniemulsification and sol–gel reaction, porous oxide nanoparticles are obtained [13-17]. However, miniemulsions can also be useful for the synthesis of nonoxide ceramics, such as carbides or nitrides, which can serve as catalysts or catalyst support for highly exothermic or high temperature reactions. Important requirements concerning these materials are chemical inertness and temperature stability.

A material with high temperature stability, as well as excellent heat conductivity, hardness and mechanical stability is SiC [18]. Next to bulk SiC, also composites [19], porous [20-25], and nanosized [26] silicon carbide are becoming increasingly interesting. There are several reports in literature showing that these materials are able to compete with supports such as alumina, silica or activated carbons, particularly in exothermic reactions [27-30].

In particular, the use of polymeric precursors for the synthesis of SiC ceramics (polymer derived ceramics) [31,32] has been found to be an easy approach. Herein, we report the synthesis of nanosized silicon(oxy)carbide spheres by the miniemulsion technique with the aid of a polycarbosilane precursor. The first studies using this approach were reported by Kroke et al. [33]. Here we present a new method to achieve catalytic functionalization and control of the particle size for these spheres either by using different surfactants, surfactant concentrations or by copolymerization with comonomers such as styrene (Sty), methyl methacrylate (MMA) or acrylic acid. Furthermore the prevalent problem of sphere sintering during pyrolysis has been overcome by means of a coating procedure. In this contribution, we describe the functionalization of SiC spheres with ceria shells. Ceria is known as an oxidation catalyst for soot combustion reaction [34,35]. Thus, we report for the first time a CeO_2/SiC core–shell system with tunable particle sizes through a miniemulsion technique, and demonstrate its use as a catalyst for the oxidation of methane.

Results and Discussion

Polycarbosilane (PCS) nanospheres were synthesized from a miniemulsion of SMP-10 (allylic functionalized polycarbosilane) in water (Figure 1). In order to demonstrate efficient tailoring of the sphere size, we used several surfactants in varying concentration. The addition of comonomers was investigated with regard to their effects on particle sizes.

The results of photon cross-correlation spectroscopy (PCCS) reveal that PCS-spheres synthesized with 2.5 wt % (with respect to the inner phase) of the cationic surfactant cetyl trimethylammonium bromide (CTAB) or the anionic surfactant sodium dodecyl sulfate (SDS) have diameters of approximately 300 nm, whereas the use of nonionic Lutensol AT50 results in larger spheres of 500 nm (Figure 2A).

This is not surprising, as nonionic surfactants are less effective in stabilizing colloids. Thus a larger amount of nonionic surfactant is required to achieve the same particle size as with an ionic surfactant. The variation of SDS concentration in the range of 1–10 wt % does not influence the particle size, but in the case of CTAB an increasing amount of surfactant leads to increasing sphere sizes. This is contrary to our expectations, but FESEM (Field Emission Scanning Electron Microscopy) investigations verified that at high CTAB concentrations large particle aggregates are formed. Elucidation of the particular mechanism behind this effect is part of the current studies, but we assume that SMP-10 partially hydrolyzes during the synthesis, creating negative charges on the particle surface which may form ion pairs with the positively charged cetyl trimethylammonium cation, thus compensating the surface charges. Nevertheless it must be stressed again that it is possible to control particle sizes

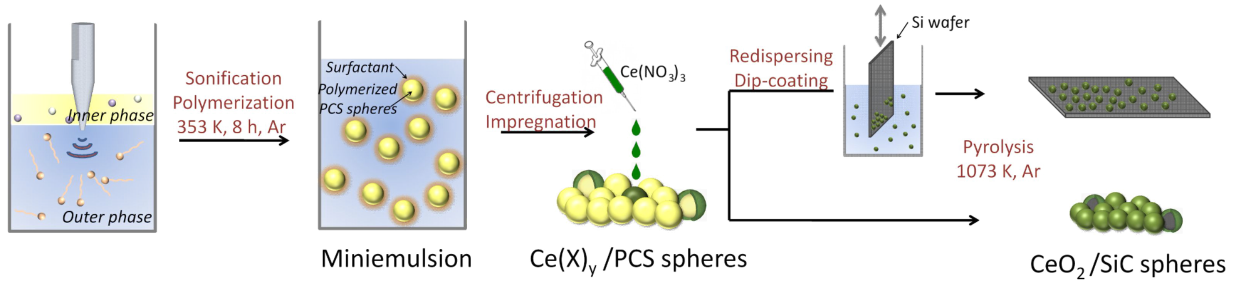

Figure 1: Scheme of the synthesis of CeO_2/Si(O)C core–shell nanoparticles via miniemulsion technique.

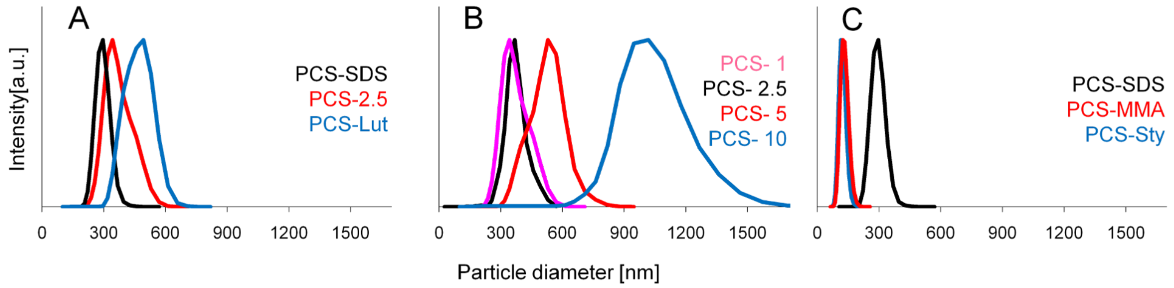

Figure 2: Photon cross-correlation spectroscopy (PCCS) measurement of PCS/water miniemulsions with A) different surfactants, B) different concentration of CTAB surfactant and C) different comonomers.

in a range of 300–1000 nm by varying the CTAB concentration. Furthermore we showed that for the synthesis of smaller particles the addition of comonomers is useful. The sizes of PCS spheres prepared with 50 wt % of styrene or MMA were reduced to 100 nm (surfactant 2.5 wt % SDS) (Figure 2C). Particles sizes as well as their elemental distribution were very uniform, indicating that copolymerization had occurred. The addition of acrylic acid did not influence the size of the resulting PCS spheres. Scanning electron micrographs verified all these trends but also showed that the PCS spheres synthesized with SDS (PCS-SDS, PCS-Sty, PCS-MMA) exhibited a narrower distribution of particle sizes than those synthesized with CTAB or Lutensol AT50 (Figure 3). The green PCS spheres exhibited a low specific surface area of ~9 $m^2 \cdot g^{-1}$.

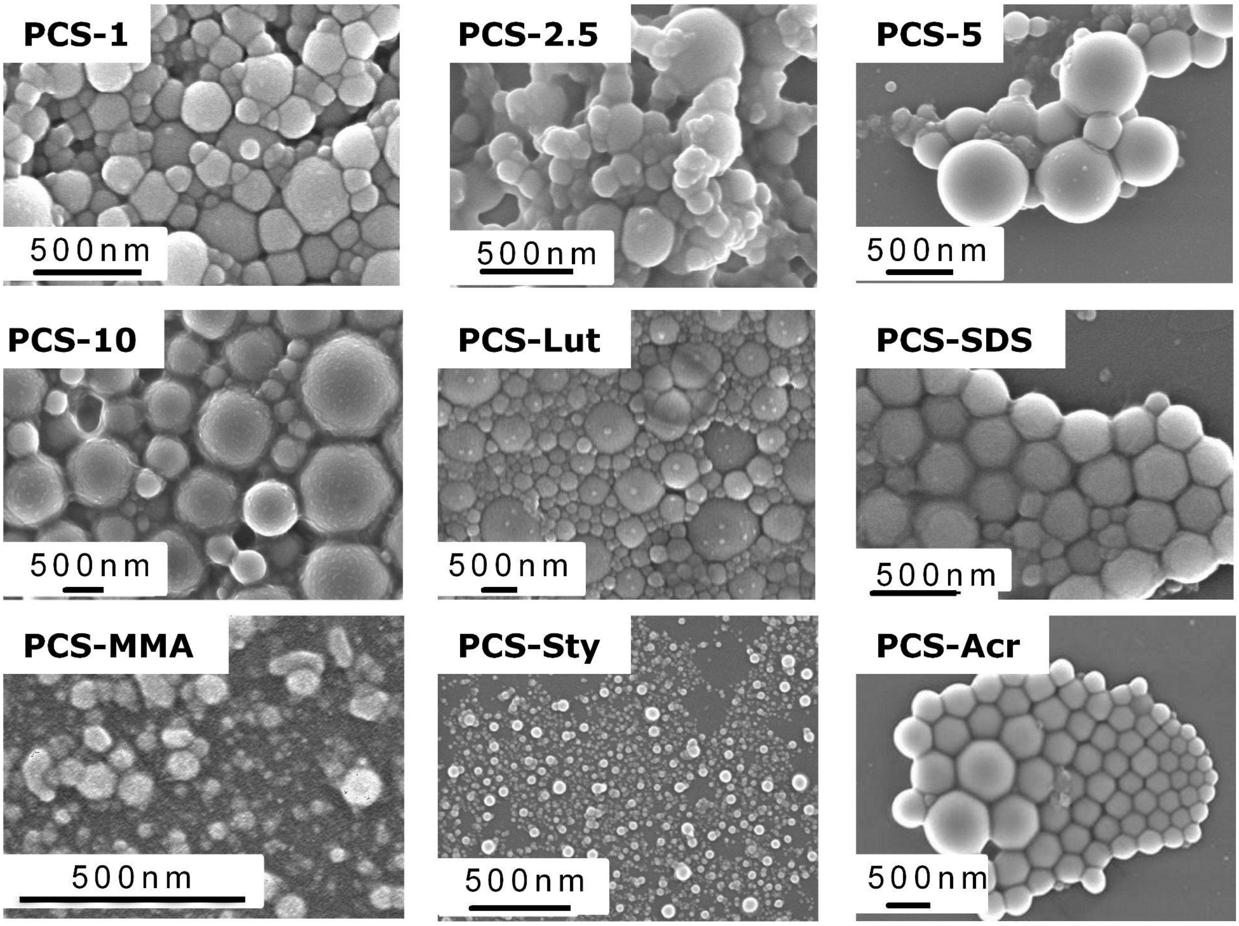

Figure 3: Scanning electron micrographs of PCS spheres synthesized with different amounts of CTAB (PCS-1 - PCS-10), different surfactants (PCS-Lut, PCS-SDS) and comonomers (PCS-MMA, PCS-Sty).

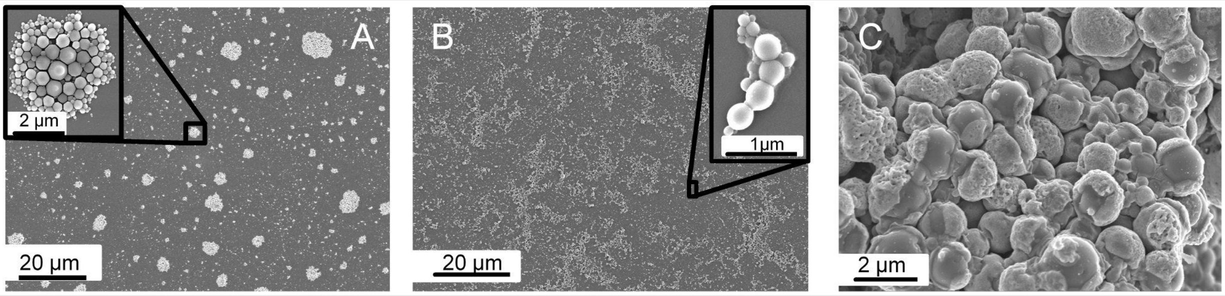

Figure 4: SEM micrographs of (A) unfunctionalized SiC-SDS spheres, (B) SiC-Acr/CeO_2 spheres prepared by molecular bonding approach and (C) SiC/CeO_2 spheres prepared by impregnation.

Functionalization and pyrolysis

The dispersion of PCS spheres can be destabilized either by adding acetone, by the evaporation of water at 353 K overnight, or by centrifugation. Subsequently, the resulting PCS spheres are either pyrolyzed instantaneously or functionalized before pyrolysis. The latter results in a core–shell-structured hybrid material. A promising method for the synthesis of core–shell hybrid materials in general was described by Landfester et al. [36]. They created surface functionalized polymer spheres coated with hydroxyapatite. Accordingly, we used the surface functionalized PCS/acrylic acid spheres for the growth of a CeO_2 shell. Additionally, dip coating of the unfunctionalized PCS spheres in an ethanolic $Ce(NO_3)_3$ solution was investigated. Functionalized as well as unfunctionalized PCS spheres were pyrolyzed at 1073–1573 K. Preliminary investigations showed that a simple bulk pyrolysis of PCS spheres, especially at high temperatures, either leads to particle aggregation or to large amounts of sintered spheres being obtained, which lose their spherical shape. Therefore pyrolysis was additionally performed on a silicon wafer in order to obtain single particles. All samples were X-ray amorphous, which is in agreement with the fact that crystalline SiC is usually generated from SMP-10 precursors at temperatures above 1573 K [22].

Figure 4A shows the individual particles and illustrates that the shape of the PCS spheres was conserved during pyrolysis. Figure 4B shows SiC-Acr spheres synthesized from PCS/acrylic acid. The carboxylate groups were used for molecular binding of ceria [36]. Although a CeO_2 shell cannot be seen on SEM pictures, the EDX-analysis of the discrete spheres confirms the presence of cerium (1.5 wt % Ce). Furthermore the catalytic tests, shown in the next chapter, prove the presence of ceria. The core–shell structure could be seen more clearly when CeO_2/Si(O)C particles that were synthesized by an impregnation approach were considered. From the scanning electron micrographs an average shell thickness of approximately 60 nm was obtained. Figure 4C illustrates the formation of these ceria shells on silicon carbide spheres. The cerium loading of these materials was increased up to 4 wt % Ce.

Element mapping with EDX was used in order to verify the core–shell structure. To achieve this, a sphere with a partially fractured shell (Figure 5A) was analyzed with regard to the distribution of cerium, oxygen and silicon. Figure 5C proves that cerium is only present in the shell of this hybrid material. The shell also contains a higher amount of oxygen than the core. The presence of oxygen at the inner sphere part can be

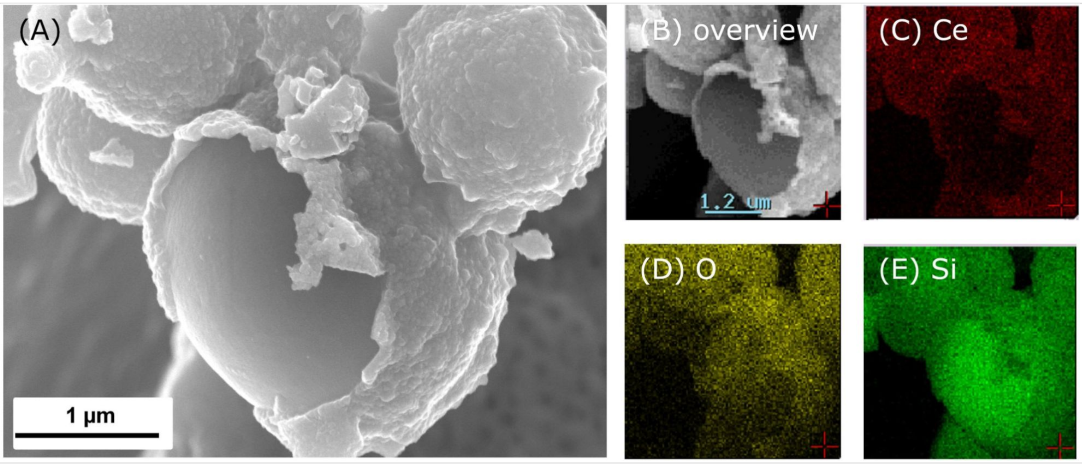

Figure 5: Elemental mapping investigations on CeO_2/Si(O)C core–shell nanoparticles prepared by impregnation.

explained by the formation of Si(O)C, which is well known for polymer derived silicon carbides [37]. It should be noted that oxygen impurities can also be introduced into the SiC core through the partial hydrolysis of the polycarbosilane precursor during the miniemulsion step, which is carried out in aqueous solution. The distribution of silicon is shown on Figure 5E. The overall composition of these core–shell particles is 4 wt % Ce, 19 wt % O, 44 wt % Si and 33 wt % C. As this data only hints at the presence of Ceria and the amounts are too small for detection in X-ray diffraction experiments, TEM investigations were carried out on different samples.

The cerium oxide particle phases were determined by comparing the lattice spacings measured from the TEM images with literature data. It can be shown that CeO_2 is present in the samples, but also phases with less oxygen, such as Ce_2O_3, can be found. In Figure 6 an image of a CeO_2 particle, the corresponding FFT and a filtered image are shown. The lattice spacing was determined in fourier space for the strongest peak and found to be 2.59 Å which is in good agreement with the data given for CeO_2 (2.60 Å, ICDD, No. 44-1001).

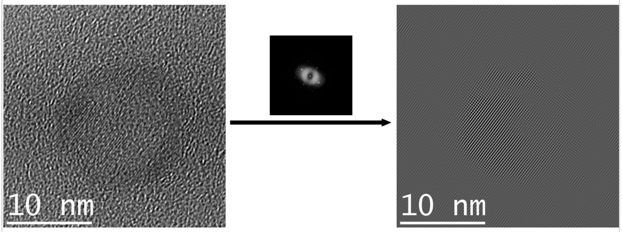

Figure 6: TEM image of a cerium oxide particle (left) with the corresponding diffractogram (middle) and a filtered image for better visibility of the lattice fringes (right).

Catalytic methane combustion

The catalytic activity was determined by temperature programmed oxidation (TPO) of methane. TPO was performed on SiC/CeO_2 and SiC-Acr/CeO_2. For comparison of the results, CeO_2 nanoparticles that were precipitated from aqueous solution and the unloaded Si(O)C shell particles were chosen. The results of the TPO measurements are presented in Figure 7. The onset temperatures for pure ceria nanoparticles and the unloaded particles, representing the uncatalyzed reaction, are 758 K and 1130 K, respectively [38]. The investigated ceria modified Si(O)C spheres show catalytic activity for the combustion of methane. The onset temperatures for SiC/CeO_2 and SiC-Acr/CeO_2 are 1018 K and 868 K, respectively. In comparison to the ceria nanoparticles the activity is lower due to the smaller amount of active material in the sample. Although SiC-Acr/CeO_2 has a smaller amount of active material (1.5 wt % Ce) than SiC/CeO_2 (4 wt %), it shows a higher activity, which can be explained by the more efficient immobilization of the cerium nitrate on the acrylic acid modified surface of the PCS spheres during functionalization. The specific surface area of SiC-Acr/CeO_2 (15 $m^2 \cdot g^{-1}$) is higher than that of SiC/CeO_2 (<0.01 $m^2 \cdot g^{-1}$), thus this also has to be considered as a contribution to the difference in catalytic activity. The enlarged specific surface area for SiC-Acr/CeO_2 is attributed to additional amorphous carbon in the spheres resulting from the combustion of acrylic acid during pyrolysis. However, the results are promising; especially considering that only 1.5 wt % of Ce was needed to decrease the onset temperature for methane combustion by 262 K.

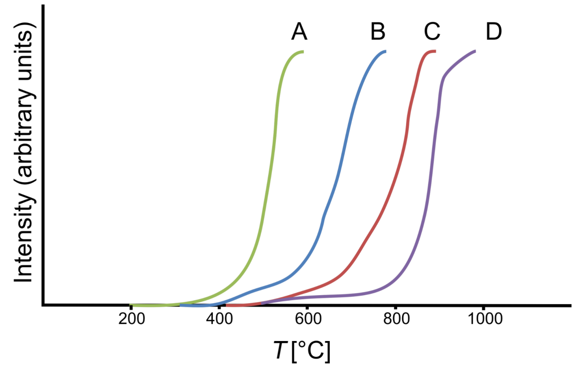

Figure 7: TPO measurements of CeO_2 nanoparticles (A), SiC-Acr/CeO_2 (B), SiC/CeO_2 (C) and the unloaded SiC shell, not containing Cerium (D).

Conclusion

We presented the synthesis of silicon(oxy)carbide spheres by a miniemulsion process. The size of these spheres can be adjusted through the use of different surfactants or surfactant concentrations. For a given surfactant concentration, nonionic surfactants, such as Lutensol AT50, cause larger particles to be formed than do ionic surfactants, such as SDS or CTAB. The increase of the surfactant concentration leads to larger spheres for particles synthesized with CTAB, whereas no influence was detected for spheres synthesized with SDS. The addition of comonomers such as styrene or MMA also lowers the particle size. Green PCS bodies were functionalized in two different ways with a ceria shell and were converted to silicon(oxy)carbide by pyrolysis under an inert atmosphere. The resulting hybrid materials were studied with scanning electron microscopy and elemental mapping, which verified the core–shell design of this new material. Finally, it was shown that these materials are suitable as catalysts for the oxidation of methane.

Experimental

Synthesis of PCS spheres

SMP10 (Starfire Systems), comonomer, 30 mg of hexadecane (Fluka, 98%) and 30 mg of AIBN (Fluka, 99%) were mixed and added to solutions of different amounts of surfactant in 30 g

Table 1: List of polycarbosilane nanospheres prepared by the miniemulsion technique.

Sample	SMP-10 [g]	Comonomer	[g]	Surfactant	[g]
PCS-1	1.65	-	-	CTAB[a]	0.0165
PCS-2.5	1.65	-	-	CTAB[a]	0.0413
PCS-5	1.65	-	-	CTAB[a]	0.0826
PCS-10	1.65	-	-	CTAB[a]	0.165
PCS-Lut	1.65	-	-	AT50[b]	0.0413
PCS-SDS	1.65	-	-	SDS[c]	0.0413
PCS-Sty	0.825	Styrene[d]	0.825	SDS[c]	0.0413
PCS-MMA	0.825	MMA[e]	0.825	SDS[c]	0.0413
PCS-Acr	0.825	Acrylic acid[f]	0.825	SDS[c]	0.0413

[a]cetyl trimethylammonium bromide (Acros, 99%), [b]Lutensol AT50 (BASF), [c]sodium dodecyl sulfate (Fluka, 99%), [d]styrene (Acros, 99%), [e]methyl methacrylate (Merck, 99%), [f]acrylic acid (ABCR, 99%).

water (Table 1). After stirring the mixture for 1 h, miniemulsification was achieved by ultrasonicating the mixture for 120 s with a Branson sonifier W450 Digital at 90% amplitude and 100% cycle. During sonication the mixture was cooled in an ice-bath. The miniemulsion was polymerized by heating to 353 K for 8 h in an argon atmosphere (Figure 1).

Functionalization

The miniemulsion was placed in a cabinet dryer for the removal of water. 60 mg of the resulting polycarbosilane (PCS) powder was added to a 0.75 M solution of 1 g $Ce(NO_3)_3 \cdot 6\ H_2O$ (Aldrich, 99%) in 3 mL ethanol, treated in an ultrasonic bath and finally separated by centrifugation.

In case of the surface functionalized PCS-Acr spheres (comonomer = acrylic acid), 3.5 mL of this PCS-Acr miniemulsion was added to an 0.1 M aqueous solution of 440 mg $Ce(NO_3)_3 \cdot 6H_2O$ (Aldrich, 99%) and stirred overnight at RT. The PCS-nanospheres were destabilized by adding acetone, centrifuged and washed with water.

Coating and pyrolysis

The functionalized PCS nanospheres were either pyrolyzed as synthesized or coated on a silicon wafer at 1073 K under an argon atmosphere (RT–573 K at 150 $K \cdot h^{-1}$, then 5 h at 573 K, followed by heating to 973 K at 30 $K \cdot h^{-1}$. After reaching 973 K, the sample was heated to 1073 K at 120 $K \cdot h^{-1}$ and maintained for 2 h). In case of coating, the nanospheres were redispersed in EtOH and coated (1.1 $mm \cdot s^{-1}$) onto a silicon wafer by means of a dip coater. Afterwards the wafer with the particles was pyrolyzed at 1073 K under an argon atmosphere.

Characterization

FESEM (Field Emission Scanning Electron Microscopy) and elemental mapping investigations on polymers and ceramics were carried out with a Stereoscan 260 SEM with EDX analysis system using SE (Secondary Electrons) and BSE (Backscattered Electrons) detectors, respectively. Elemental analyses using EDX were obtained as a mean value of five measurements at a magnification of 3000. TEM investigations were carried out by crushing the synthesized powders in a ball mill, followed by ultrasonically assisted suspension in ethanol or isopropanol. The resulting suspension was dropped onto a copper grid coated with holey carbon and dried using an infrared lamp. The TEM investigations were carried out on a Cs-corrected JEOL JEM-2010F. Particle sizes were determined with photon cross-correlation spectroscopy (PCCS) using a Nanophox particle sizer (Sympatec GmbH). The dispersions were diluted with demineralized water for the measurement. Catalytic investigations were carried out as described in previous studies [38].

Acknowledgements

The authors would like to thank Dr. Alicja Bachmatiuk and Dr. Mark H. Rümmeli (Leibniz Institute IFW Dresden) for guidance and help during the TEM measurements, as well as the Deutsche Forschungsgemeinschaft, especially the priority program 1181 Nanomat, for funding this work.

References

1. Crespy, D.; Landfester, K. *Beilstein J. Org. Chem.* **2010,** *6,* 1132. doi:10.3762/bjoc.6.130
2. Bradley, M. A.; Prescott, S. W.; Schoonbrood, H. A. S.; Landfester, K.; Grieser, F. *Macromolecules* **2005,** *38,* 6346. doi:10.1021/ma0473622
3. Landfester, K. *Angew. Chem., Int. Ed.* **2009,** *48,* 4488. doi:10.1002/anie.200900723
4. Landfester, K.; Weiss, C. K. *Adv. Polym. Sci.* **2010,** *229,* 1. doi:10.1007/12_2009_43
5. Holzapfel, V.; Lorenz, M.; Weiss, C. K.; Schrezenmeier, H.; Landfester, K.; Mailänder, V. *J. Phys.: Condens. Matter* **2006,** *18,* S2581. doi:10.1088/0953-8984/18/38/S04
6. Ramírez, L. P.; Landfester, K. *Macromol. Chem. Phys.* **2003,** *204,* 22. doi:10.1002/macp.200290052

7. Zheng, W.; Gao, F.; Gu, H. *J. Magn. Magn. Mater.* **2005,** *288,* 403. doi:10.1016/j.jmmm.2004.09.125
8. Xu, H.; Cui, L.; Tong, N.; Gu, H. *J. Am. Chem. Soc.* **2006,** *128,* 15582. doi:10.1021/ja066165a
9. Luna-Xavier, J.-L.; Guyot, A.; Bourgeat-Lami, E. *J. Colloid Interface Sci.* **2002,** *250,* 82. doi:10.1006/jcis.2002.8310
10. Zhang, S.-W.; Zhou, S.-X.; Weng, Y.-M.; Wu, L.-M. *Langmuir* **2005,** *21,* 2124. doi:10.1021/la047652b
11. Landfester, K.; Schork, F. J.; Kusuma, V. A. *C. R. Chim.* **2003,** *6,* 1337. doi:10.1016/j.crci.2003.07.019
12. Bechthold, N.; Tiarks, F.; Willert, M.; Landfester, K.; Antonietti, M. *Makromol. Chem., Macromol. Symp.* **2000,** *151,* 549. doi:10.1002/1521-3900(200002)151:1<549::AID-MASY549>3.0.CO;2-D
13. Schiller, R.; Weiss, C. K.; Landfester, K. *Nanotechnology* **2010,** *21,* 405603. doi:10.1088/0957-4484/21/40/405603
14. Rossmanith, R.; Weiss, C. K.; Geserick, J.; Hüsing, N.; Hörmann, U.; Kaiser, U.; Landfester, K. *Chem. Mater.* **2008,** *20,* 5768. doi:10.1021/cm800533a
15. Schiller, R.; Weiss, C. K.; Geserick, J.; Hüsing, N.; Landfester, K. *Chem. Mater.* **2009,** *21,* 5088. doi:10.1021/cm901858v
16. Nabih, N.; Schiller, R.; Lieberwirth, I.; Kockrick, E.; Frind, R.; Kaskel, S.; Weiss, C. K.; Landfester, K. *Nanotechnology* **2011,** *22,* 135606. doi:10.1088/0957-4484/22/13/135606
17. Kubiak, P.; Fröschl, T.; Hüsing, N.; Hörmann, U.; Kaiser, U.; Schiller, R.; Weiss, C. K.; Landfester, K.; Wohlfahrt-Mehrens, M. *Small* **2011,** *7,* 1690. doi:10.1002/smll.201001943
18. Schwetz, K. A. Silicon Carbide Based Hard Materials. In *Handbook of Ceramic Hard Materials;* Riedel, R., Ed.; Wiley-VCH: Weinheim, Germany, 2000; Vol. 1, pp 683–740. doi:10.1002/9783527618217.ch20
19. Krawiec, P.; Weidenthaler, C.; Kaskel, S. *Chem. Mater.* **2004,** *16,* 2869. doi:10.1021/cm034737+
20. Krawiec, P.; Geiger, D.; Kaskel, S. *Chem. Commun.* **2006,** 2469. doi:10.1039/b603284b
21. Krawiec, P.; Kaskel, S. *J. Solid State Chem.* **2006,** *179,* 2281. doi:10.1016/j.jssc.2006.02.034
22. Krawiec, P.; Schrage, C.; Kockrick, E.; Kaskel, S. *Chem. Mater.* **2008,** *20,* 5421. doi:10.1021/cm801035g
23. Lu, A.-H.; Schmidt, W.; Kiefer, W.; Schüth, F. *J. Mater. Sci.* **2005,** *40,* 5091. doi:10.1007/s10853-005-1115-8
24. Pol, V. G.; Pol, S. V.; Gedanken, A. *Chem. Mater.* **2005,** *17,* 1797. doi:10.1021/cm048032z
25. Shi, Y. F.; Meng, Y.; Chen, D. H.; Cheng, S. J.; Chen, P.; Yang, H. F.; Wan, Y.; Zhao, D. Y. *Adv. Funct. Mater.* **2006,** *16,* 561. doi:10.1002/adfm.200500643
26. Rendtel, A.; Hübner, H.; Herrmann, M.; Schubert, C. *J. Am. Ceram. Soc.* **1998,** *81,* 1109. doi:10.1111/j.1151-2916.1998.tb02457.x
27. Ledoux, M. J.; Pham-Huu, C. *CATTECH* **2001,** *5,* 226. doi:10.1023/A:1014092930183
28. Ledoux, M. J.; Hantzer, S.; Huu, C. P.; Guille, J.; Desaneaux, M.-P. *J. Catal.* **1988,** *114,* 176. doi:10.1016/0021-9517(88)90019-X
29. Pham-Huu, C.; Del Gallo, P.; Peschiera, E.; Ledoux, M. J. *Appl. Catal., A* **1995,** *132,* 77. doi:10.1016/0926-860X(95)00151-4
30. Kizling, M. B.; Stenius, P.; Andersson, S.; Frestad, A. *Appl. Catal., B* **1992,** *1,* 149. doi:10.1016/0926-3373(92)80021-Q
31. Laine, R. M.; Babonneau, F. *Chem. Mater.* **1993,** *5,* 260. doi:10.1021/cm00027a007
32. Colombo, P.; Modesti, M. *J. Am. Ceram. Soc.* **1999,** *82,* 573. doi:10.1111/j.1151-2916.1999.tb01803.x
33. Bakumov, V.; Schwarz, M.; Kroke, E. *J. Eur. Ceram. Soc.* **2009,** *29,* 2857. doi:10.1016/j.jeurceramsoc.2009.04.004
34. Miró, E. E.; Ravelli, F.; Ulla, M. A.; Cornaglia, L. M.; Querini, C. A. *Catal. Today* **1999,** *53,* 631. doi:10.1016/S0920-5861(99)00151-0
35. Trovarelli, A. *Catal. Rev. - Sci. Eng.* **1996,** *38,* 439. doi:10.1080/01614949608006464
36. Ethirajan, A.; Ziener, U.; Landfester, K. *Chem. Mater.* **2009,** *21,* 2218. doi:10.1021/cm9001724
37. Merle-Méjean, T.; Abdelmounim, E.; Quintard, P. *J. Mol. Struct.* **1995,** *349,* 105. doi:10.1016/0022-2860(95)08720-G
38. Kockrick, E.; Frind, R.; Rose, M.; Petasch, U.; Böhlmann, W.; Geiger, D.; Herrmann, M.; Kaskel, S. *J. Mater. Chem.* **2009,** *19,* 1543. doi:10.1039/b813669f

License and Terms

The definitive version of this article is the electronic one which can be found at:
doi:10.3762/bjnano.2.67

Beilstein Journal
of Nanotechnology

Template-assisted formation of microsized nanocrystalline CeO_2 tubes and their catalytic performance in the carboxylation of methanol

Jörg J. Schneider*[1], Meike Naumann[1], Christian Schäfer[1], Armin Brandner[2],
Heiko J. Hofmann[2] and Peter Claus[2]

Full Research Paper

Open Access

Address:
[1]Department of Chemistry, Eduard-Zintl-Institute, Inorganic Chemistry, Technische Universität Darmstadt, Petersenstr. 18, 64287 Darmstadt, Germany and [2]Department of Chemistry, Ernst-Berl-Institute, Technical Chemistry II, Technische Universität Darmstadt, Petersenstr. 20, 64287 Darmstadt, Germany

Email:
Jörg J. Schneider* - joerg.schneider@ac.chemie.tu-darmstadt.de

* Corresponding author

Keywords:
activation of CO_2; ceria; electrospinning; exotemplating; nanotubes

Beilstein J. Nanotechnol. **2011,** *2,* 776–784.
doi:10.3762/bjnano.2.86

Received: 06 June 2011
Accepted: 16 November 2011
Published: 30 November 2011

This article is part of the Thematic Series "Micro- and mesoporous solids: From science to application"

Associate Editor: J. Rühe

Abstract

Polymethylmethacrylate (PMMA)/ceria composite fibres were synthesized by using a sequential combination of polymer electrospinning, spray-coating with a sol, and a final calcination step to yield microstructured ceria tubes, which are composed of nanocrystalline ceria particles. The PMMA template is removed from the organic/inorganic hybrid material by radio frequency (rf) plasma etching followed by calcination of the ceramic green-body fibres. Microsized ceria (CeO_2) tubes, with a diameter of ca. 0.75 µm, composed of nanocrystalline agglomerated ceria particles were thus obtained. The 1-D ceramic ceria material was characterized by X-ray diffraction, scanning electron microscopy (SEM), high-resolution transmission electron microscopy (HRTEM), UV–vis and photoluminescence spectroscopy (PL), as well as thermogravimetric analysis (TGA). Its catalytic performance was studied in the direct carboxylation of methanol with carbon dioxide leading to dimethyl carbonate [$(CH_3O)_2CO$, DMC], which is widely employed as a phosgene and dimethyl sulfate substitute, and as well as a fuel additive.

Introduction

Ceria, CeO_2, is known as a semiconducting ceramic material with unique electronic properties, exhibiting a broad range of functional properties with potential for application in various areas [1-3]. Due to its extraordinary thermal and chemical stability, it is a promising material for catalytic, environmental and energy applications, such as in solid oxide fuel cells (SOFCs) [4,5], or for the elimination of pollutants from automobile exhaust gases, or for fluid catalytic cracking or dehydrogenation of ethylbenzene to styrene. With respect to catalysis, CeO_2 is a valuable support material for the low-temperature water–gas shift reaction and preferential oxidation of CO in hydrogen-enriched atmospheres. Herein, we will focus our attention on the direct carboxylation of methanol to dimethyl carbonate (DMC) catalyzed by nanostructured ceria. DMC is a noncorrosive and environmentally friendly solvent, which is used as alternative to highly toxic carbonylating and methylating agents. For catalytic applications, the performance of ceria is strongly dependent on its crystallinity and textural properties, including surface area and porosity. Although nanocrystalline ceria is known to be more active than amorphous ceria [6], it tends to agglomerate into larger crystallites under conditions of high-temperature catalysis. In this context, the preparation of high-surface-area ceria films by using a polymer-templating method was investigated in an effort to reduce such agglomeration [1,7-11]. Nanosized ceria can be synthesized by methods such as chemical vapour deposition (CVD), spray pyrolysis, hydrothermal synthesis or electrosynthesis [1,2,9]. These approaches lead to particulate, nanocrystalline powdered samples, with the exception of the CVD method, which gives thin ceria films [2-15]. One-dimensional (1-D) nanostructures such as nanowires, nanorods and nanotubes have attracted increasing attention owing to their reduced dimensionality and unique functional properties [16].

Electrospinning is a technology that allows the formation of polymer fibres with nanoscale dimensions [17-20]. Such nanofibres and nanotubes based on electrospun polymers offer a broad range of applications in areas such as photonics, sensorics, catalysis, medicine, pharmacy and functional textiles [17,20]. By employing these one-dimensional (1-D) polymer fibres as structure-directing templates for nanomaterial synthesis, 1-D oxide materials are accessible. This process is called TUFT (tubes by fibre templates) [17,18] and typically uses an electrospinning technique in which polymer and inorganic precursor solutions are electrosprayed *together* to give the final inorganic 1-D material.

By taking advantage of the higher catalytic activity of nanocrystalline ceria compared to amorphous ceria on one side [6], and the possibility to obtain stable 1-D microstructured oxide morphologies by electrospinning, we designed a material combining the advantages of a nano/micro-structured hierarchy, which offers a high catalytic activity on the nanoscale, combined with a low tendency for the isolated nanoparticles to further agglomerate when using a pre-assembly technique to form a microsized 1-D wire structure. We employed a template-directed synthesis using electrospun polymer fibres, followed by deposition of a nanoscaled inorganic ceria sol-precursor solution by spray coating onto the polymer fibre template. The sequential electrospinning and spraycoating process steps are finally followed by dry O_2 plasma etching and calcination to yield microsized ceria tubes composed of nanocrystalline, entangled ceria tubes which display a macroscopic matlike material morphology. Our process, however, is significantly different to the TUFT process in which both components, i.e., the polymer and the inorganic precursor component, are sprayed at the same time. The macroscopically sized ceramic mats, which are composed of porous hierarchically structured microsized nanocrystalline ceria tubes, were thus obtained by a sequential synthesis process. As a suitable application, the catalytic performance of these macrosized mats of nanostructured ceria tubes was investigated for the direct carboxylation of methanol with carbon dioxide leading to dimethyl carbonate (DMC).

Results and Discussion

Synthesis of polymer fibre templates

Polymer fibres were fabricated by electrospinning in a vertical electrode arrangement. The polymer solution was 15 wt % PMMA dissolved in a mixture of acetone and dimethyl formamide (60/40), which was electrospun at 26 kV through a nozzle with dimensions of 0.8 × 4.0 mm and a current flow of 4 μA was achieved. The electrospun polymer template has an average fibre diameter of 1.3–1.8 μm, which can be varied by changing the properties of the polymer solution used [17]. Typically, dense mats of fibres on the counter electrode (copper plate, 15 × 15 cm^2) were formed (Figure 1). The thickness of the obtained fibre mats depends on the spinning time.

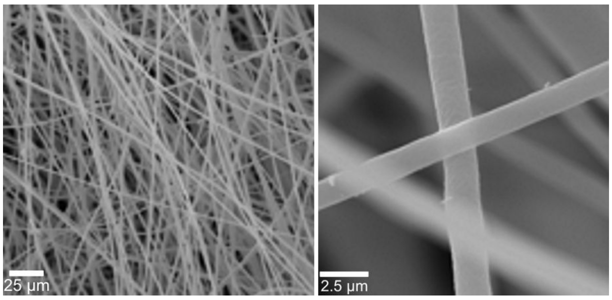

Figure 1: Scanning electron micrographs (SEM) of electrospun PMMA fibres, fabricated from a 15 wt % solution of PMMA in a mixture of acetone and dimethyl formamide (60/40). An average fibre diameter of 1.8 μm was obtained.

Synthesis and characterization of hierarchical microsized nanocrystalline ceria fibre mats

Formation of ceria tubes without surfactant

Ceria tubes were prepared by an exotemplating technique. After controlled ageing of a sol-precursor solution prepared from cerium ammonium nitrate $(NH_4)_2Ce(NO_3)_6$ in water and

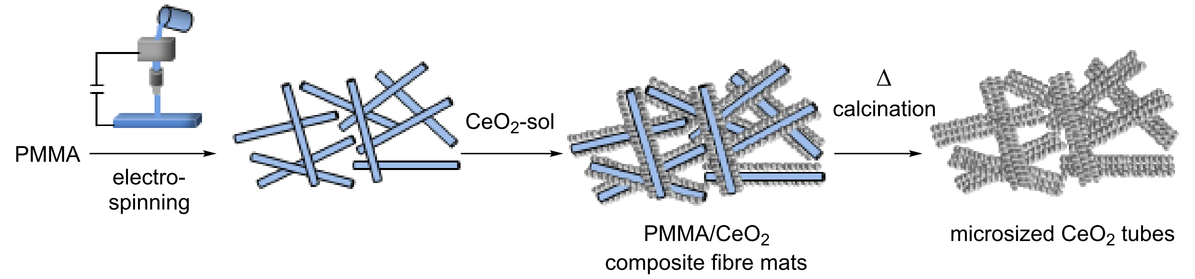

Scheme 1: Schematic representation of the exotemplating process for the preparation of CeO_2 fibre mats with a microtubular structure. After electrospinning of a PMMA solution, the resulting PMMA fibre mat is impregnated with the ceria sol suspension by spray coating and then precalcined giving a PMMA/CeO_2 green-body composite. A final calcination step leads to the microsized pure ceria fibre mats composed of ceria tubes.

ammonia at 50 °C for half an hour, the sol was allowed to infiltrate into the electrospun polymer-template fibre mats upon application by a spray-coating technique [9,20,21]. The obtained PMMA/ceria composite samples were then plasma etched in 20 vol % oxygen atmosphere (air) for 16 h to remove the majority of the polymer template. Removal of the PMMA solely by a thermal process, through calcination of the polymer/inorganic hybrid structure, results in a complete collapse of the resulting porous ceria structure and formation of a dense ceria film. The plasma etching process was followed by a final calcination of the "green-body structure" at 350 °C for 3 h. Scheme 1 shows the complete synthesis process in an overview. Figure 2 shows a SEM image of the thus-obtained ceria mats composed of ceria tubes after the final ceramisation step.

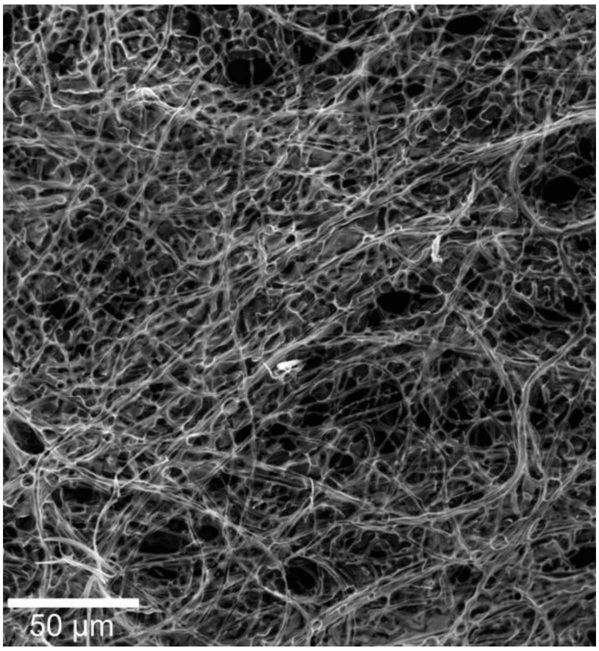

Figure 2: SEM image of the macrosized ceria mats, composed of ceria microtubes obtained by plasma treatment and further calcination at 350 °C for 3 h.

The nanocrystallinity of the ceria tubes was investigated by transmission electron microscopy (TEM, Figure 3). Samples were obtained by ultrasonification over a long period, which breaks down the microtubular structure, of which the ceria mats are composed, and results in spherical ceria particles, which are clustered into larger micrometre-sized aggregates.

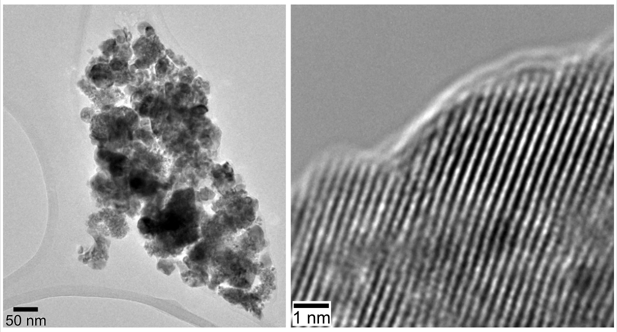

Figure 3: TEM and high-resolution TEM images of agglomerated nanosized ceria particles, which are the building blocks of the microscopic ceria tubes shown in Figure 2. These tubes are entangled into larger aggregates, which are the building blocks for the ceria mats. The particles are isolated from the dense mats by intense ultrasonification over a long period.

Figure 4 shows the XRD spectrum of such ceria nanoparticles [22]. The spectrum indicates a phase-pure face-centred-cubic fluorite-type CeO_2 (JCPDS 78-0694, No. 225). No other phases or impurities were detected.

Formation of ceria tubes with surfactant Pluronic P123®

To further improve the intimate contact between the aqueous ceria sol (see before) and the polymer fibre substrate during synthesis, the surfactant Pluronic P123® was added to the sol prior to spray coating. Pluronic P123® is a triblock copolymer based on individual poly(ethylene glycol)-poly(propylene glycol)-poly(ethylene glycol) blocks, which form spherical and cylindrical micelles, and which could thus allow for a better

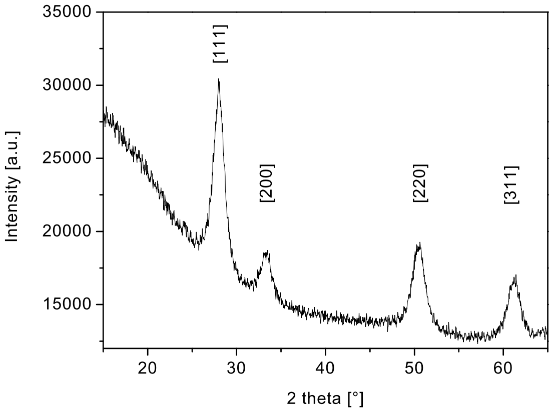

Figure 4: X-ray diffraction (XRD) pattern of nanostructured ceria.

contact of the inorganic ceria sol with the electrospun polymer fibres during impregnation. After spray-coating followed by sol–gel transformation to the ceramic green body at 80 °C overnight, the green body was further plasma etched (20 vol % O_2 atmosphere for 16 h), followed by a calcination step at 350 °C for 3 h, yielding the final macrostructured ceria mats (Scheme 2 and Figure 5). Surface area measurements employing the Brunauer–Emmett–Teller (BET) method, revealed a surface area of 126 $m^2 \cdot g^{-1}$ for this hierarchically structured ceria material.

After a final calcination step at 350 °C, the morphology of the ceria material changed considerably compared to the ceria material obtained by the previously described procedure without Pluronic P123® additive. Again, ceria tubes of microscopic size were obtained with comparable diameter as before (diameter ca. 0.75 μm). However, these were instead embedded in a thin ceria film which interconnects the individual ceria tubes, building up a filamentous network structure (Figure 6).

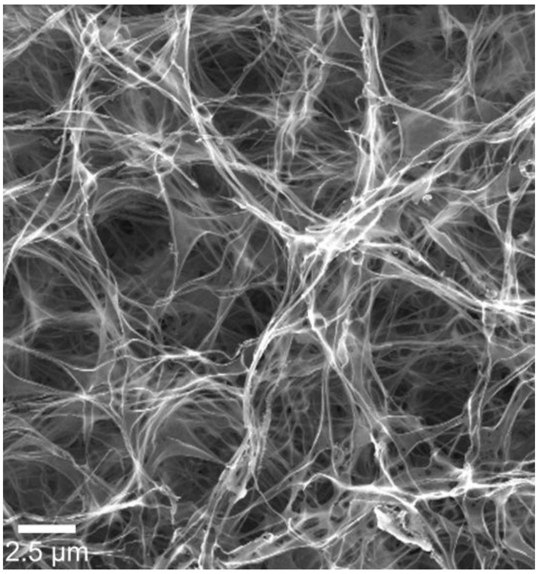

Figure 5: SEM image of the final ceria mats, obtained by plasma treatment and further calcination at 350 °C, for 3 h to remove the polymer template. The ceria-sol-impregnation step of the polymer fibres was performed with the addition of Pluronic P123®.

The crystalline nature of this ceria thin film interconnecting the tubes is shown in the TEM images (Figure 7). Obviously the block copolymer P123® is capable of acting as a template to guide the ceria sol around the polymer fibres, resulting in 1-D ceria tubes after polymer etching and calcinations, as found for the process without addition of the block copolymer. The 2-D ceria film formed due to the addition of the block copolymer P123® interconnects these ceria tubes, thus forming a network structure. Although we were not able to determine the thickness of the ceria film connecting the tubes, the image contrast in the TEM experiment (Figure 7, left side) is comparable to that of the carbon-grid substrate surface, corresponding to only a few nanometres.

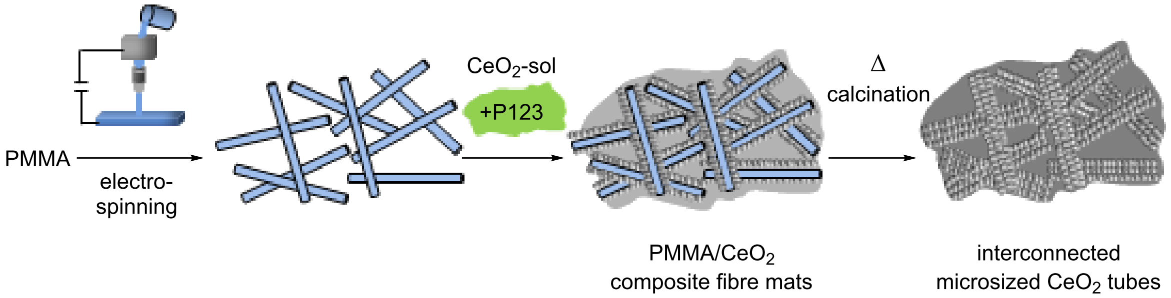

Scheme 2: Schematic representation of the exotemplating process for the preparation of CeO_2 fibremats by using triblock copolymer Pluronic P123®. After the formation of the PMMA fibremats by electrospinning, the ceria sol as well as P123® were added simultaneously, dried and plasma etched, giving a 2-D ceria/1-D ceria interconnected structure of the green-body composite. A final calcination step yielded the ceria tube structure in which the individual tubes are interconnected by a ceria thin film (dark grey).

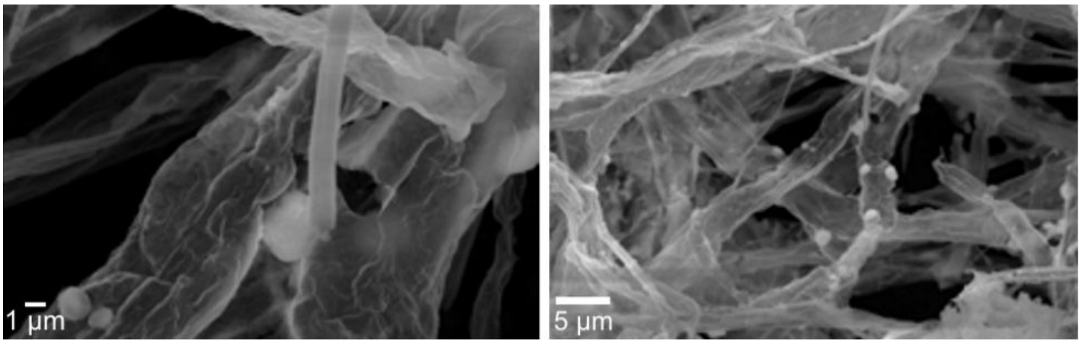

Figure 6: SEM images (different magnifications) of interconnected microsized ceria tubes. Samples were fabricated, using PMMA fibre templates, coated with a ceria sol containing surfactant Pluronic P123®.

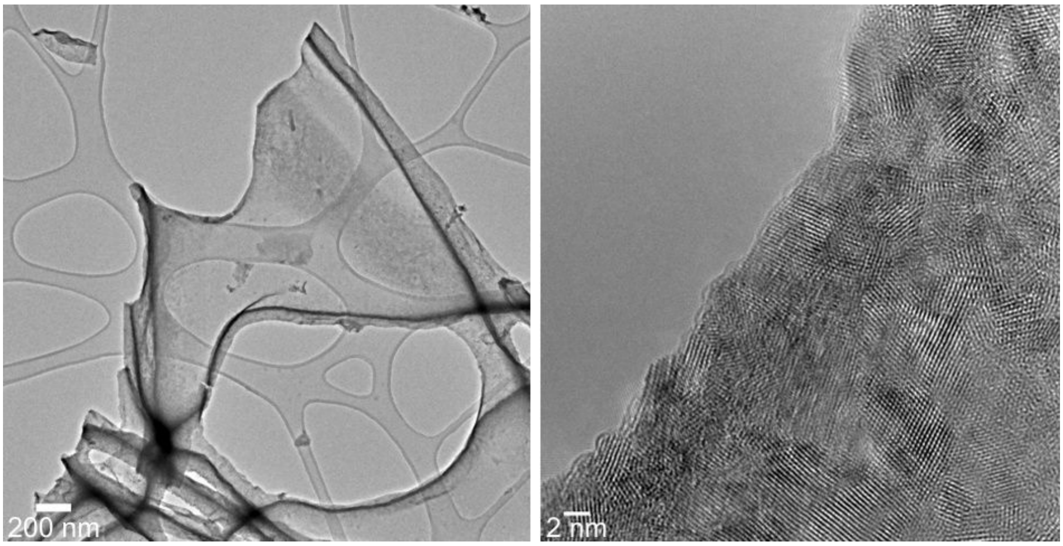

Figure 7: TEM (left) and HRTEM (right) images of nanostructured ceria thin film interconnecting the ceria tubes (with addition of Pluronic P123® to the sol) at different magnifications.

An average ceria particle size of about (5 ± 0.1) nm was deduced, by using the Scherrer equation, from the XRD measurements (Figure 8) of the ceria particles that constitute the film interconnecting the tubes. This is in good agreement with the ceria particle size obtained from the HRTEM studies but significantly larger than that observed for the ceria material obtained without Pluronic P123® surfactant. Again the only phase observed in the XRD is the crystalline cubic-fluorite-type phase of CeO_2.

To study the thermal processing behaviour during the conversion process of the green body into the final ceria ceramics in more detail, we investigated the PMMA polymer fibres impregnated with ceria sol, with and without Pluronic P123® surfactant (samples PMMA/sol and PMMA/sol + Pluronic P123®, Figure 9).

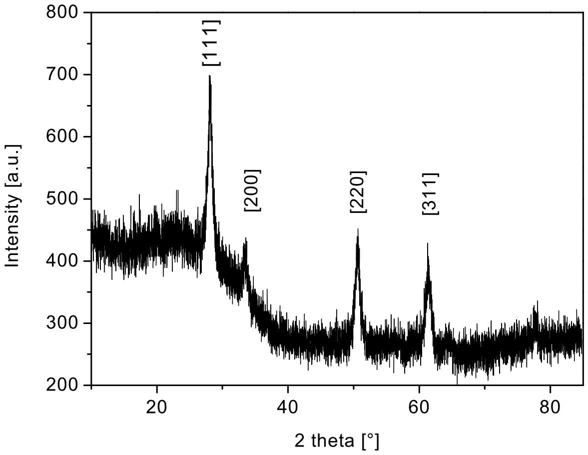

Figure 8: XRD spectra of nanostructured ceria (obtained with addition of Pluronic P123® to the sol).

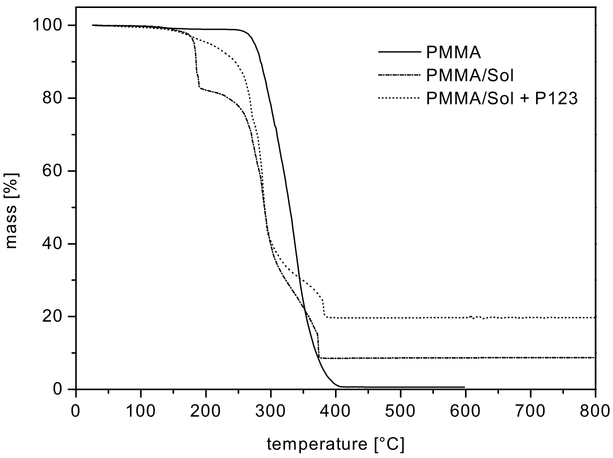

Figure 9: TGA measurements of bare PMMA fibres (PMMA, solid line), a PMMA/sol without Pluronic P123® (PMMA/sol, dashed-dotted line) and a PMMA/sol containing Pluronic P123® (PMMA/sol + P123, dotted line).

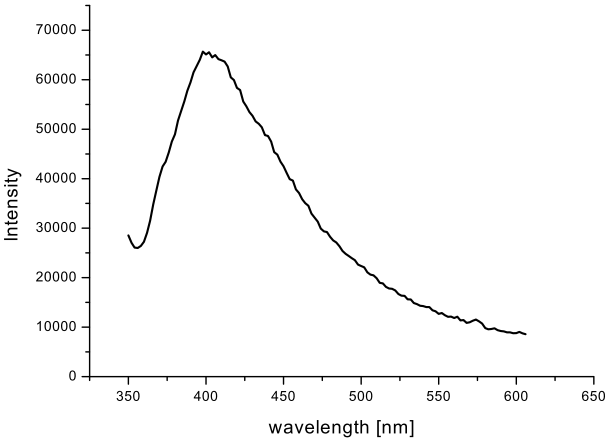

Figure 10: PL spectrum of microsized ceria tubes composed of nanostructured ceria (obtained with addition of Pluronic P123® to the sol) at an excitation wavelength of 325 nm.

At 400 °C PMMA fibres were completely decomposed and removed from the samples. For the PMMA/sol with P123® (PMMA/Sol + P123®) the transformation was already complete at 365 °C with a ceramic yield of nearly 20%. This finding is in contrast to the conversion of the PMMA/sol without additional P123® surfactant (PMMA/sol) in which the overall ceramic yield was 10% and therefore significantly lower. This difference can be attributed to an enhanced wetting of the surface of the polymer fibres, as well as in the interstices between the packed PMMA fibre mats, during the impregnation step. This leads to a significantly enhanced wetting of the PMMA polymer template and thus a denser material deposition of the ceria sol.

Photoluminescence (PL) measurements (Figure 10, excitation wavelength 325 nm) reveal a maximum at 415 nm [23]. The strong emission of CeO_2 at this wavelength is related to abundant defects such as dislocations, which are helpful for fast oxygen transport [23].

Catalytic studies

Ceria nanomaterials as supports for precious metals (e.g., Au, Pt) show interesting properties in CO oxidation in the water gas shift reaction as well as in oxygen storage [12-14,24,25]. These properties are due to the high occurrence of oxygen defects in crystalline ceria. The relatively high surface area together with the nano/microsized morphology compared to nanocrystalline ceria renders our new ceria morphology interesting for catalysis. As a test reaction the synthesis of dimethyl carbonate $(CH_3O)_2CO$ (DMC) by direct carboxylation of methanol was studied:

$$CO_2 + 2\,MeOH \rightarrow \left(CH_3O\right)_2 CO + H_2O$$

DMC is known as a green chemical and alternative to toxic and corrosive reagents, e.g., replacing phosgene or dimethyl sulfate (as a starting material for organic synthesis by carbonylation or methylation), as well as being an octane booster in gasoline and additive to diesel fuel (for particle emission decrease), and also a solvent [6,25-27]. Owing to its low toxicity, versatile reactivity and high dielectric constant, DMC also attracts interest as an electrolyte in lithium-ion batteries [28]. The formation of DMC by direct methanol carboxylation, however, is restricted by thermodynamic effects (equilibrium is far to the educt side) and, in addition to that, sometimes even by severe ceria catalyst agglomeration and decomposition [29]. The maximum yield of DMC observed is currently reported to be within 0.5 and 1 wt % [6,30,31]. CO_2 as C_1 feedstock is often used under supercritical conditions, affording an improved reactivity, polarity and solubility, thus enhancing its catalytic activity and selectivity [29,32]. Ceria shows both acidic and basic properties, which are important for its reactivity as a catalyst [29]. In addition, it is known that even though ceria and other electron deficient metal oxides, such as zirconia [30,31] and titania [33], are active in direct carboxylation of methanol to DMC, they are also easily deactivated, sometimes already before recycling experiments can be started, resulting in only marginal methanol conversion. It can be shown that this is due to ceria agglomeration and can be partially prevented by solid dilution of the active ceria catalyst with up to 20%, e.g., of alumina [34]. It would be interesting to find out whether a destructive agglomeration of the ceria catalyst could be diminished significantly by a nano/microsized ceria structure in which the nanoscaled particles are stabilized to a certain extent in a 1-D morphological order.

The direct carboxylation reactions of methanol were conducted in a multibatch system (five parallel reactors) with independent pressure and temperature control for each reactor set up. Samples with different surface treatments were tested (ceria sample 1 was obtained by template-directed synthesis with Pluronic P123® as surfactant, without additional plasma etching. Samples 2 and 3 were obtained as sample 1, but additional plasma etching was used with sample 3). Due to the plasma etching the tubular 1-D structure is more pronounced in sample 1 compared to 2 and 3. In all three samples the crystallite size is ca. 5 nm. So far, ceria with particle sizes between 15–60 nm have shown a maximum catalytic activity in the DMC synthesis reaction [30,31]. Therefore, a nanoparticulate reference sample of ceria with a crystallite size of 15 nm was prepared by the oxalate-gel precipitation technique [35]. Samples 1–3, as well as the ceria reference sample, maintained their structural integrity (ceria) before and after the catalytic reaction, as can be seen from the XRD spectra (see Figure 11 for sample 3, a similar behaviour was found for samples 1 and 2).

Sample 1 gave an overall mass fraction of 0.63 wt % DMC, which is 0.08 wt % less than for the 15 nm ceria reference sample (0.71 wt %). Samples 2 and 3 led to slightly lower yields of 0.42 wt % and 0.39 wt %, respectively, compared to the nanocrystalline ceria sample prepared by the oxalate-gel method. Related to methanol, the yields obtained from samples 1, 2 and 3 were 0.41, 0.28 and 0.26%, respectively, compared to 0.47 % from the 15 nm ceria reference sample (Figure 12, Table 1).

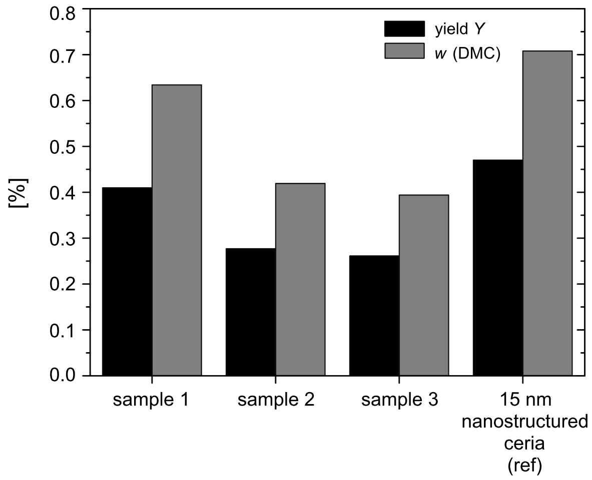

Figure 12: Comparison of the overall yield (*Y*) of nano/microsized ceria nanotubes (samples 1,2,3) versus nanostructured ceria particles (15 nm) as reference, and mass fractions of DMC in methanol (*w*) in the direct carboxylation reaction of methanol.

The 1-D ceria structures show slightly lower overall mass fractions of DMC and hence also lower yields than those of the ceria obtained by the oxalate-gel method. However, the catalyst activity is already close to the best values obtained from the reference sample. A crucial point relating to the morphology of the structure is their mechanical stability. We observed partial destruction of the 1-D structure during the catalytic reactions in the liquid reaction phase of the batch reactor setup. Currently we are setting up a gas-phase reaction system in order to study the DMC formation under gas phase conditions, with an aim to

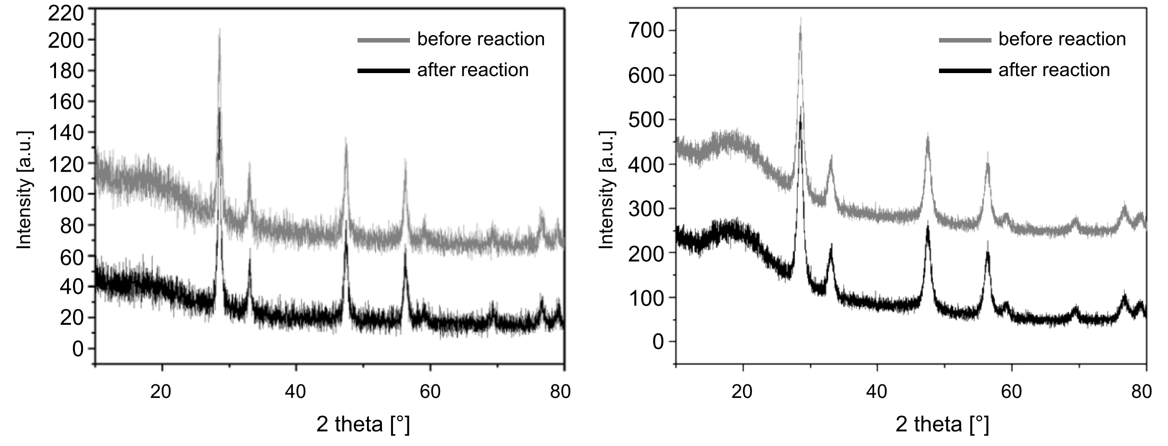

Figure 11: XRD spectra of the ceria reference sample (15 nm diameter) prepared by the standard oxalate-gel method (left) and sample 3 (right) obtained by template-directed synthesis with Pluronic P123® before and after reaction, are shown.

Table 1: Comparison of the experimental catalytic conditions in the direct carboxylation reaction of methanol for nano/microsized ceria nanotubes versus nanostructured ceria particles (15 nm diameter).[a]

catalyst sample	m_{cat} [mg]	w(DMC) [wt %]	Y [%]
1	104.2	0.63	0.41
2	96.1	0.42	0.28
3	99.9	0.39	0.26
ref	101.0	0.71	0.47

[a] Y = yield related to methanol; w(DMC) = mass fraction of DMC in MeOH; m_{cat} = catalyst mass (temperature = 150 °C, reaction time = 300 min; stirring rate = 600 rpm, pressure = 60 bar).

minimize the mechanical stress on the ceria-mat structure during the cycling experiments. This should avoid the mechanical breakdown of the nano/microsized 1-D structure into a nanoparticulate ceria material and could thus result in an even higher catalytic activity.

Conclusion

Template-directed synthesis of ceria nanotubes was accomplished, using electrospun PMMA polymer templates. Exotemplating by spray coating of an inorganic ceria sol was used as the technique to introduce the ceria *after* final calcination. Templating under presence of Pluronic P123® allows the formation of an interpenetrating network in which a thin ceria film interconnects the microsized ceria tubes. A combined process of plasma etching and calcination was chosen to remove the PMMA template material, avoiding thermal stress. The obtained highly crystalline 1-D ceria materials show a high activity in the direct carboxylation of methanol to dimethyl carbonate (DMC), but the mechanical stability of the 1-D material needs to be improved further.

Experimental

Synthesis of polymer template fibres

A solution of 15 wt % PMMA (type 7N, Röhm GmbH) in a mixture of acetone and dimethyl formamide (60/40; Merck KGaA) was electrospun from a glass syringe (5 mL) with tip dimensions of 0.8 × 40 mm at an electrode distance of 20 cm and 26 kV for 12 h. After 12 h, a dense web of PMMA fibres was collected on the copper counter electrode (15 × 15 cm^2).

Preparation of ceria nanotubes

1.37 g (2.5 mmol) cerium ammonium nitrate $(NH_4)_2Ce(NO_3)_6$ (Alfa Aesar, 98.0+%) was dissolved in 40 mL distilled water. 0.65 mL aqueous 25 wt % ammonia solution (Merck) was added and the solution was vigorously stirred for half an hour. 1 g Pluronic P123® (Sigma Aldrich) was added and dissolved at 50 °C. The sol was used immediately. The as-prepared cerium-containing sol was spray coated on the previously prepared polymer fibres by using a spray bottle (Roth, 50 mL). Afterwards, sol–gel transformation of the spray-coated sample was achieved in a furnace (Memmert) at 80 °C overnight. Plasma etching was performed by using a Diener Electronics PS Tech, Femto machine with 20 vol % O_2 (Messer Griesheim) as etching gas, for 18 h. Finally, the green body obtained was calcined at 350 °C for 3 h.

Preparation of ceria reference sample

Reference samples (ref) of ceria were prepared by oxalate-gel precipitation [35]. A freshly prepared solution of 1 mol·L^{-1} oxalic acid (≥99.0%, Sigma-Aldrich) in ethanol (≥99.8%, 1% methyl ethyl ketone, Carl Roth) was added under vigorous stirring to an ethanolic solution of cerium(III) nitrate hexahydrate (≥99.5%, p.a, Carl Roth, 0.33 mol·L^{-1}) with 20% molar excess. A white gel formed instantaneously and was subsequently aged for an additional two hours at room temperature under medium stirring. Afterwards the aged gel was heated at 80 °C on a heating blanket to dryness and calcined in air (25 $\text{mL·g}^{-1}\text{·min}^{-1}$) at 600 °C (RT, 1 h to 150 °C, 4.5 h to 600 °C, 4 h at 600 °C).

Direct carboxylation of methanol

For the catalytic reaction 10 mL methanol (250 mmol, ≥99.9%, Carl Roth, 0.02 wt % water) and 100 mg catalyst were charged into the reactor. After closure the reactors were rendered inert by flushing three times with argon (5.0, Linde) subsequently followed by pressurizing the reactor with 55 bar CO_2 (4.5, Linde) for one minute. The reactors were heated up to 150 °C and the temperature was held for the duration of the reaction. After reaction, the reactors were quenched to room temperature and the pressure was released slowly. Samples were taken and were characterized quantitatively by GC analysis with toluene as internal standard.

Materials characterization

Scanning electron microscopy (SEM) was performed on a FEI XL30 FEG at an operating voltage of 25 kV. For transmission electron microscopy (TEM) a FEI Technai F20 was used, with an operating voltage of 200 keV. X-ray diffraction (XRD) spectra were recorded on StoeCIE and StadiP (Co Kα1) instruments. Thermogravimetric analysis (TGA) was performed on a Netzsch TG 209 F1 instrument coupled with a QMS 403 C mass spectrometer. For BET measurements a NOVA 3000e (Quantachrome) was used. For PLE measurements, Horiba, Fluorog-3 (Xe, excitation wavelength 325 nm) was used. For UV–vis spectroscopy, Perkin Elmer, Lambda 900 was used. DLS was measured by using a Malvern Zetasizer Nano with a red laser of 633 nm.

Acknowledgements

We thank Dr. J. Engstler for the TEM measurements. TEM measuring time was made possible through the cooperative project ERC-TUD 001 at the Ernst-Ruska-Centre (ERC) for Microscopy and Spectroscopy with Electrons, Forschungszentrum, Jülich, Germany.

References

1. Devaraju, M. K.; Yin, S.; Sato, T. *ACS Appl. Mater. Interfaces* **2009,** *1,* 2694–2698. doi:10.1021/am900574m
2. Wang, H.; Zhu, J.-J.; Zhu, J.-M.; Liao, X.-H.; Xu, S.; Ding, T.; Chen, H.-Y. *Phys. Chem. Chem. Phys.* **2002,** *4,* 3794–3799. doi:10.1039/b201394k
3. Saitzek, S.; Blach, J.-F.; Villain, S.; Gavarri, J.-R. *Phys. Status Solidi A* **2008,** *205,* 1534–1539. doi:10.1002/pssa.200723419
4. Tang, L.; Salamon, M.; De Guire, M. R. *Sci. Adv. Mater.* **2010,** *2,* 79–89. doi:10.1166/sam.2010.1059
5. Chen, W.-T.; Chen, K.-B.; Wang, M.-F.; Wenig, S.-F.; Lee, C.-S.; Lin, M.-C. *Chem. Commun.* **2010,** *46,* 3286–3288. doi:10.1039/b923217f
6. Yoshida, Y.; Arai, Y.; Kado, S.; Kunimori, K.; Tomishige, K. *Catal. Today* **2006,** *115,* 95–101. doi:10.1016/j.cattod.2006.02.027
7. Crocker, M.; Graham, U. M.; Gonzalez, R.; Morris, E.; Jacobs, G.; Andrews, R. *Mater. Res. Soc. Symp. Proc.* **2005,** *876,* R4.
8. Brezesinski, T.; Erpen, C.; Iimura, K.-I.; Smarsly, B. *Chem. Mater.* **2005,** *17,* 1683–1690. doi:10.1021/cm0479180
9. Basu, S.; Devi, P. S.; Maiti, H. S. *J. Mater. Res.* **2004,** *19,* 3162–3171. doi:10.1557/JMR.2004.0442
10. Lyons, D. M.; Ryan, K. M.; Morris, M. *J. Mater. Chem.* **2002,** *12,* 1207–1212. doi:10.1039/b104677m
11. Byk Additives & Instruments, Nanotechnology Additives, Technical Information L-NI 1. http://www.nanoingermany.com/uploads/company_data/117/L-NI1_en.pdf (Accessed Nov 15, 2011.
12. Mädler, L.; Stark, W. J.; Pratsinis, S. E. *J. Mater. Res.* **2002,** *17,* 1356–1362. doi:10.1557/JMR.2002.0202
13. Yang, H.; Huang, C.; Tang, A.; Zhang, X.; Yang, W. *Mater. Res. Bull.* **2005,** *40,* 1690–1695. doi:10.1016/j.materresbull.2005.05.014
14. Pavlopoulos, D.; Al Khatiab, S.; Button, T. W.; Abell, J. S. *J. Phys.: Conf. Ser.* **2008,** *97,* 012098. doi:10.1088/1742-6596/97/1/012098
15. Du, N.; Zhang, H.; Chen, B.; Ma, X.; Yang, D. *J. Phys. Chem. C* **2007,** *111,* 12677–12680. doi:10.1021/jp074011r
16. Yan, L.; Xing, X.; Yu, R.; Deng, J.; Chen, J.; Liu, G. *Physica B* **2007,** *390,* 59–64. doi:10.1016/j.physb.2006.07.062
17. Greiner, A.; Wendorff, J. H. *Angew. Chem., Int. Ed.* **2007,** *46,* 5670–5703. doi:10.1002/anie.200604646
    Greiner, A.; Wendorff, J. H. *Angew. Chem.* **2007,** *119,* 5770–5805. doi:10.1002/ange.200604646
18. Greiner, A.; Wendorff, J. H. Functional Self-Assembled Nanofibers by Electrospinning. In *Self-Assembled Nanomaterials I–Nanofibers;* Shimizu, T., Ed.; Advances in Polymer Science, Vol. 219; Springer: Berlin, Heidelberg, 2008; pp 107–171. doi:10.1007/978-3-540-85103-5
19. Krogman, K. C.; Lowery, J. L.; Zacharia, N. S.; Rutledge, G. C.; Hammond, P. T. *Nat. Mater.* **2009,** *8,* 512–518. doi:10.1038/nmat2430
20. Verma, A.; Karar, N.; Bakhshi, A. K.; Chander, H.; Shivaprasad, S. M.; Agnihotry, S. A. *J. Nanopart. Res.* **2007,** *9,* 317–322. doi:10.1007/s11051-006-9085-6
21. Li, L.; Yang, H. K.; Moon, B. K.; Fu, Z.; Guo, C.; Jeong, J. H.; Yi, S. S.; Jang, K.; Lee, H. S. *J. Phys. Chem. C* **2009,** *113,* 610–617. doi:10.1021/jp808688w
22. West, A. R. *Grundlagen der Festkörperchemie;* Wiley-VCH: Weinheim, 1992.
23. Mochizuki, S.; Fujishiro, F. *Phys. Status Solidi B* **2009,** *246,* 2320–2328. doi:10.1002/pssb.200844419
24. Yang, X.; Shao, C.; Liu, Y.; Mu, R.; Guan, H. *Thin Solid Films* **2005,** *478,* 228–231. doi:10.1016/j.tsf.2004.11.102
25. Bhanage, B. M.; Fujita, S.-i.; Ikushima, Y.; Arai, M. *Appl. Catal., A* **2001,** *219,* 259–266. doi:10.1016/S0926-860X(01)00698-6
26. La, K. W.; Jung, J. C.; Kima, H.; Baeck, S.-H.; Song, I. K. *J. Mol. Catal. A: Chem.* **2007,** *269,* 41–45. doi:10.1016/j.molcata.2007.01.006
27. Abimanyu, H.; Kim, C. S.; Ahn, B. S.; Yoo, K. S. *Catal. Lett.* **2007,** *118,* 30–35. doi:10.1007/s10562-007-9091-z
28. Abimanyu, H.; Ahn, B. S.; Kim, C. S.; Yoo, K. S. *Ind. Eng. Chem. Res.* **2007,** *46,* 7936–7941. doi:10.1021/ie070528d
29. Tomishige, K.; Kunimori, K. *Appl. Catal., A* **2002,** *237,* 103–109. doi:10.1016/S0926-860X(02)00322-8
30. Tomishige, K.; Sakaihori, T.; Ikeda, Y.; Fujimoto, K. *Catal. Lett.* **1999,** *58,* 225–229. doi:10.1023/A:1019098405444
31. Tomishige, K.; Ikeda, Y.; Sakaihori, T.; Fujimoto, K. *J. Catal.* **2000,** *192,* 355–362. doi:10.1006/jcat.2000.2854
32. Sakakura, T.; Choi, C.-J.; Saito, Y.; Sako, T. *Polyhedron* **2000,** *19,* 573–576. doi:10.1016/S0277-5387(99)00411-8
33. Zhong, S.-H.; Kong, L.-L.; Li, H.-S.; Xiao, X.-F. *Ranliao Huaxue Xuebao* **2002,** *30,* 454.
34. Aresta, M.; Dibenedetto, A.; Pastore, C.; Cuocci, C.; Aresta, B.; Cometa, S.; De Giglio, E. *Catal. Today* **2008,** *137,* 125–131. doi:10.1016/j.cattod.2008.04.043
35. Sun, Q.; Zhang, Y.-L.; Chen, H.-Y.; Deng, J.-F.; Wu, D.; Cheny, S.-Y. *J. Catal.* **1997,** *167,* 92–105. doi:10.1006/jcat.1997.1554

License and Terms

Beilstein Journal
of Nanotechnology

Synthesis and catalytic applications of combined zeolitic/mesoporous materials

Jarian Vernimmen, Vera Meynen* and Pegie Cool

Review

Address:
Laboratory of Adsorption and Catalysis, Department of Chemistry,
University of Antwerp, Universiteitsplein 1, B-2610 Wilrijk, Belgium

Email:
Vera Meynen* - vera.meynen@ua.ac.be

* Corresponding author

Keywords:
catalysis; characterization; combined zeolitic/mesoporous materials;
synthesis

Beilstein J. Nanotechnol. **2011,** *2,* 785–801.
doi:10.3762/bjnano.2.87

Received: 01 August 2011
Accepted: 13 October 2011
Published: 30 November 2011

This article is part of the Thematic Series "Micro- and mesoporous solids:
From science to application".

Guest Editor: J. J. Schneider

Abstract

In the last decade, research concerning nanoporous siliceous materials has been focused on mesoporous materials with intrinsic zeolitic features. These materials are thought to be superior, because they are able to combine (i) the enhanced diffusion and accessibility for larger molecules and viscous fluids typical of mesoporous materials with (ii) the remarkable stability, catalytic activity and selectivity of zeolites. This review gives an overview of the state of the art concerning combined zeolitic/mesoporous materials. Focus is put on the synthesis and the applications of the combined zeolitic/mesoporous materials. The different synthesis approaches and formation mechanisms leading to these materials are comprehensively discussed and compared. Moreover, Ti-containing nanoporous materials as redox catalysts are discussed to illustrate a potential implementation of combined zeolitic/mesoporous materials.

Introduction

Nanoporous materials are characterized by their relatively high surface areas and pore volumes within a small amount of material. These properties, together with the fact that they have (uniform) channels and voids in the nanometer range, make them ideal candidates for implementation in several applications. In fact, nanoporous materials are used extensively in a wide variety of applications on industrial, pilot, and laboratory scale in many different research areas, such as fine and specialty chemistry [1-3], petrochemistry [4,5] and medicine [2,6-10]. They can be applied as catalysts [1-5,11], drying agents [5,12], adsorbers [5,13], sensors [14,15], controlled-drug-release agents [6,8], column-packing material [16], food additives [17], etc. According to IUPAC (International Union of Pure and Applied Chemistry) nomenclature, nanoporous materials are classified in categories of microporous (pore diameter <2 nm), mesoporous (pore diameter 2–50 nm) and macroporous (pore diameter >50 nm) structures. The enormous diversity in nanoporous structures as well as the fact that their properties can be tuned and modified depending on the type of application is responsible for the huge interest in these materials among different scientific communities. Therefore, research has been focused on the elucidation of the formation mechanism, the development of new, tailor-made nanoporous structures, and the implementation of the materials in various processes and applications. More specifically, in the last decade, the development of mesoporous materials with zeolitic features has received a lot of attention. These combined zeolitic/mesoporous materials are thought to be superior materials, since they are able to combine (i) the enhanced diffusion and accessibility for larger molecules and viscous fluids of mesoporous materials with (ii) the remarkable stability, catalytic activity and selectivity of zeolites.

This review gives an overview of the state of the art in the development of combined zeolitic/mesoporous materials. It is divided into two parts. In the first section, the synthesis methods and formation mechanisms of the combined zeolitic/mesoporous materials are described. In addition, a thorough evaluation of the different synthesis strategies leading towards combined zeolitic/mesoporous materials is carried out, in which their advantages and disadvantages are discussed and a comparison is drawn between the different methods. In the second part, Ti-containing nanoporous materials as redox catalysts are used as an example to illustrate the potential implementation of combined zeolitic/mesoporous materials. Although there is a huge variety of combined zeolitic/mesoporous materials with deviating properties (sorbent, acidic, redox, basic), the examples throughout this review, including the section on the implementation of combined zeolitic/mesoporous materials, are specifically focused on Ti-containing siliceous materials. This is because our research group has much experience with these types of materials. Moreover, the different aspects we want to highlight during this review can be perfectly demonstrated with Ti-containing combined zeolitic/mesoporous materials. Despite the focus on Ti-containing combined zeolitic/mesoporous materials, we are convinced that the conclusions and observations in this review are valid for the majority of combined zeolitic/mesoporous materials, irrespective of the active element.

Review

1 Combined zeolitic/mesoporous materials

1.1 Evolution towards combined zeolitic/mesoporous materials

The large-scale implementation of zeolites in industrial applications and the still-growing amount of publications involving zeolites prove that these materials are of prime importance in a wide variety of scientific fields. This is without a doubt due to their crystalline, microporous 3-D structure and their ability to accommodate many different heteroelements (other than Si and O). Their remarkable stability (mechanical, hydrothermal, thermal and chemical) and high catalytic activity and (shape) selectivity make zeolites unique materials. However, despite these wonderful properties, zeolites have one major drawback: Their microporous nature causes accessibility problems and diffusion limitations for large molecules and viscous fluids [2,18]. In the specific case of TS-1 [19], only molecules with a kinetic diameter of maximally 0.6 nm (e.g., benzene) can access the structure and reach the active sites. This drastically limits their implementation in, e.g., fine and specialty chemistry, pharmaceutical industry and biological applications, for which large, bulky molecules are often required. Possible solutions for this limitation are (i) to decrease the crystal sizes of the zeolites and/or (ii) to develop materials with larger pores [20]. The first option was applied to reduce the intracrystalline diffusion path length [21]. However, separation of these nanozeolites is difficult, since they tend to aggregate and form colloidal solutions. Moreover, nanozeolites often have different properties compared to their larger counterparts, such as a diminished crystallinity, resulting in a loss of catalytic activity and lower stability [20,21]. The second option is the creation of nanoporous materials with larger pores, namely mesoporous materials, such as SBA-15 [22,23], SBA-16 [23], M41S [24-26], MSU [27-31], MCF [32] and many others [33,34]. These mesoporous materials can overcome diffusion and accessibility problems, and this has opened up new perspectives in, for example, catalysis and medical applications. More detailed information on the formation mechanisms, the applications and the characteristics of mesoporous materials can be found in several excellent reviews [33-37]. Although there is large diversity in structural properties among mesoporous materials, these materials all have in common that their (metallo)silicate framework is not crystalline, but amorphous. This implies that their stability is inherently lower than that of zeolites [38]. Moreover, their amorphous nature and specific synthesis conditions often cause difficulties for the incorporation of heteroelements into their structure, which results in a lower catalytic activity than in the case of zeolites. For example, due to the harsh acidic medium that is required for the synthesis of SBA-15, leaching of heteroelements such as Ti is unavoidable during in situ syntheses, limiting their catalytic activity [39-42]. Moreover, in some occasions the amorphous siliceous framework hampers the solid incorporation of heteroelements in the specific coordination needed for catalysis. For example, the incorporation of Ti in tetrahedral positions, as in TS-1 zeolites, is difficult in Ti-MCM-41 since the structure contains a lot of defects, resulting in the formation of a substantial amount of octahedrally coordinated Ti [35,43].

Therefore, in the last decade, research has been focused on the combination of mesoporosity and zeolitic features [20,44-50]. Many promising materials, such as MTS-9 [51] and Ti-MMM-1 [52] have already been developed. The ultimate goal is to develop a "true" hierarchical mesoporous zeolite, meaning a mesoporous material with zeolitic walls, wherein the micro- and mesopores are interconnected in order to form a hierarchical structure. Such mesoporous zeolites are expected to be superior materials since they will be able to catalyze the typical reactions in which standard zeolites are used, but instead of being limited by the microporous nature, they will be able to convert larger molecules as well [44]. Moreover, the presence of a hierarchical pore system is also considered to be beneficial, since the presence of two interconnected pore systems with different dimensions ensures (i) a high mass transfer through the mesopores; (ii) a high surface area available for interaction of the molecules with the active sites and (iii) the catalytic features (i.e., shape selectivity) of the micropores [44,45]. However, a proper connectivity between the various levels of pores is vital to maximize the benefit of hierarchy in catalyzed reactions. J. Pérez-Ramírez et al. [48] discussed the different degrees of hierarchy that can be obtained in a combined zeolitic/mesoporous material (Figure 1). In Figure 1a, the reference zeolite system is depicted, which gives rise to mass transfer and accessibility problems for large molecules. In Figure 1b, four nanozeolites are bridged by interparticle mesoporous voids. In Figure 1c and Figure 1d on the other hand, "real" mesopores exist in combination with micropores, but in the case of Figure 1d the mesopores are only accessible via the micropores. Here, it is clear that not all configurations with a combined micro- and mesoporosity inherently give rise to an enhanced molecular transport to or from the active sites in the micropores. However, this does not mean that these combined zeolitic/mesoporous materials without (or with only minor) "true" hierarchical ordering cannot be beneficial for certain reactions. In fact, often a uniform pore size distribution and a high level of porosity are much more relevant than a perfectly ordered nanoporous material. The disordered mesoporous material, KIT-1 [53], is the perfect example illustrating that the absence of any ordering does not necessarily imply that the material cannot be useful, and in fact it may be even better than its ordered analog (MCM-41) in certain cases [54-56]. Considering combined zeolitic/mesoporous materials, there are several examples of materials that give rise to an enhanced catalytic performance in comparison with their purely zeolitic and/or mesoporous counterparts [51,52,57-59]. MTS-9 for example [51], gives rise to a higher catalytic activity in the epoxidation of styrene than Ti-MCM-41 and shows a selectivity and activity similar to TS-1 zeolite. In the hydroxylation of 2,3,6-trimethylphenol, MTS-9 is more active than both Ti-MCM-41 and TS-1. However, there are also examples of combined zeolitic/mesoporous materials, wherein there is no significant improvement when a comparison is drawn with standard zeolites or mesoporous materials [60-62]. Cheneviere et al. [60] showed that their developed mesoporous TS-1 material does not give rise to the expected improved catalytic properties of a hierarchical catalyst in oxidation reactions with aqueous H_2O_2, probably because of its increase in hydrophilic character in comparison with a conventional zeolite. Thus, whether a combined zeolitic/mesoporous material shows great potential or not, does not necessarily depend only on its "true" hierarchical character. The type of application as well as the structural characteristics of the material, and therefore also the synthesis method, are without a doubt equally important aspects.

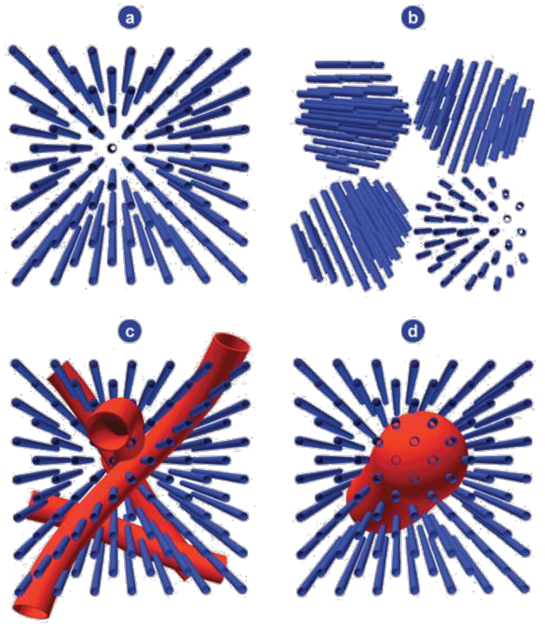

Figure 1: Different degrees and types of hierarchy can be defined in porous materials [48]. Reproduced by permission of The Royal Society of Chemistry.

1.2 Synthesis of combined zeolitic/mesoporous materials

Table 1 gives an overview of the most important synthesis approaches to obtain combined zeolitic/mesoporous materials [44-49]. There also exist other, more exotic approaches, such as nuclear track imprinting [63], but since their use is not very widespread, they will not be dealt with here. The synthesis methods can be roughly divided into three different classes, namely postsynthetic, templating and nontemplating approaches. In the postsynthetic approach, a zeolite or mesoporous material is first formed before being subjected to an additional treatment. The main difference between templating and nontemplating synthesis strategies is whether or not a mesotemplate is used in order to create combined zeolitic/mesoporous

Table 1: Overview of the most important synthesis strategies for the formation of combined zeolitic/mesoporous materials.

postsynthetic	templating		nontemplating
demetallation	**hard**[a]	**soft**[a]	mesotemplate-free synthesis (sol–gel)
recrystallization	carbon	MOS[b]: one-pot, two-pot	self-formation mechanism of hierarchy
deposition	aerogel, polymer, resin	POS[c]: one-pot, two-pot	
delamination	biological materials		

[a]The classification of “hard” (or solid or textural) and “soft” templates is based on the physical nature of the mesotemplates. [b]MOS: molecular organized systems; [c]POS: polymeric organized systems.

materials (the classification is analogous to purely mesoporous materials) [44]. Note that the majority of the templating and nontemplating methods listed in Table 1 are exactly the same as in the synthesis of purely mesoporous materials, meaning that these approaches have simply been extrapolated to the synthesis of combined zeolitic/mesoporous materials by replacing the silica source with zeolitic nanoparticles (two-pot templating approach). In addition, there are also unique approaches that have been specifically developed for the formation of combined zeolitic/mesoporous materials, such as the one-pot templating synthesis in which the micro- and mesotemplate are added to the same reaction vessel.

An alternative classification of the different synthesis approaches that is often applied is the distinction between the bottom-up and top-down synthesis strategies [48]. On the one hand, the bottom-up methods build the materials from the precursors up, meaning that they start from building units and chemicals in order to constructively form the combined zeolitic/mesoporous materials. On the other hand, the top-down approaches are focused on the controlled removal of material from an already existing structure in order to create combined zeolitic/mesoporous materials. In the subsequent part, the different methods (listed in Table 1) along with their advantages and disadvantages, will be discussed. The examples will be mainly focused on Ti-containing combined zeolitic/mesoporous materials.

1.2.1 Postsynthetic approach

Demetallation: In demetallation, a metal is selectively removed from the framework of a zeolite by postsynthetic steaming, chemical treatment, or acid or base leaching, resulting in randomly created voids in the mesoporous range [45,50]. The oldest form of demetallation and at the same time the first technique applied for creating mesopores in zeolites is dealumination [64]. By subjecting Al-containing zeolites to a hydrothermal treatment (steaming) and/or acid leaching, the Si–O–Al bonds are hydrolyzed, resulting in a partial destruction of the silicate framework. The dealumination process occurs randomly and depends highly on the amount of Al incorporated in the structure and on the applied extraction method. Although the created mesopores are beneficial and dealumination is a simple, widely used (industrial) procedure, the main drawbacks [44,45,50] of this method are (i) the partial amorphization of the zeolite framework; (ii) the loss of catalytic activity as part of the active element is removed; (iii) the fact that the mesopores are rather cavities that are not interconnected to form a mesoporous network; (iv) the random nature of the mesopore formation; (v) the fact that the porosity of dealuminated zeolites is seriously altered in an uncontrolled way during regeneration at high temperature; (vi) the partial blockage of the active sites by deposition of amorphous material inside the meso- and micropores and (vii) the restriction to Al-containing zeolites.

A very promising alternative and highly reproducible method is desilication [48,50,65-67]. Extraction of Si atoms by base treatments (also denoted as pore-directing agents, PDAs) leads to a significant amount of intracrystalline mesoporosity while preserving the intrinsic acidity and structural integrity of the zeolite framework. Also during this process, Al present in the zeolite framework plays a key role: For the ZSM-5 zeolite, Groen et al. demonstrated that the optimal Si/Al ratio is 25–30 (Figure 2) [66]. However, the fact that Al needs to be present in the framework immediately exposes the drawback of this synthesis approach, namely that the desilication is limited by the initial Si/Al framework. A good alternative is the combination of dealumination and desilication, since this allows an extra flexibility regarding the Si/Al ratios and a decoupled modification of mesoporous and acidic features [65]. Moreover, recently Verboekend et al. [68] showed that by complementing the alkaline solution with external (large size) PDAs full compositional flexibility can be achieved in the preparation of mesoporous zeolites by the desilication method. By proper control of the synthesis conditions, even Al-free zeolites can undergo a successful desilication treatment. A few studies on detitanation [69,70] and deboronation [71,72] have also been reported.

Recrystallization: Recrystallization is a typical top-down approach since it starts from a full-grown zeolite or a purely mesoporous structure, which is then impregnated by either a

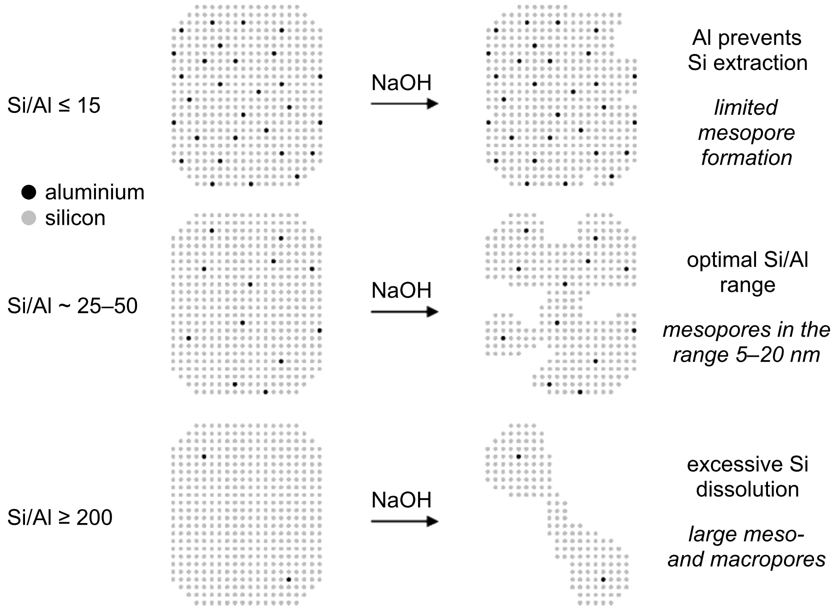

Figure 2: A simplified representation of the influence of the Al content on the desilication of ZSM-5. Reprinted with permission from [66]. Copyright 2004 American Chemical Society.

mesotemplate [73,74] or a microtemplate [75,76], and subjected to a hydrothermal treatment. This results in dissolution of the silica, which will then interact with the template and recrystallize in a mesoporous or zeolitic phase depending on the added template. The degree of crystallinity or mesoporosity can be altered by changing the reaction conditions. In general, recrystallization will give rise to composite zeolitic/mesoporous materials rather than true hierarchical materials [50]. In the case of recrystallization of a mesoporous material, it is important to start from a structure with thick walls (such as SBA-15) or to fill the mesopores with a support material (such as the mesotemplate [77]) in order to prevent a collapse of the mesopores during zeolitization. An example of a combined zeolitic/mesoporous material synthesized by the recrystallization route is UL-TS-1, which is formed by heating TPAOH-impregnated, amorphous, Ti-containing mesoporous materials for several days at 120 °C [78,79].

Postsynthetic deposition of zeolitic nanoparticles into mesoporous materials: In this method, a presynthesized mesoporous material is impregnated with a zeolite precursor solution [44,79-85]. This solution is obtained by terminating the zeolite formation in an early stage, often before the hydrothermal treatment, so that the zeolitic nanoparticles cannot evolve into a full-grown zeolite [51]. For MFI zeolites, the nanoparticles size is typically around 4 nm, although there is no consensus on the shape of the particles [86-88]. The mesoporous supports are generally large-pore materials, such as SBA-15 and MCF (mesocellular foam) so that the nanoparticles can be accommodated inside the mesopores. The impregnation of the nanoparticles can occur through wet, incipient wetness and dry impregnation. During a wet impregnation, the mesoporous material is completely soaked in a solution of nanoparticles, while in the case of a dry impregnation a volume of solution identical to, or even smaller than, the total pore volume is added. An incipient wetness impregnation lies between these two extremes.

By applying this synthesis strategy, a combined zeolitic/mesoporous material is obtained with zeolite-like (microporous) nanoplugs and/or a zeolite-like coating (inside the pores and/or on the outside of the material). In the case of a mesoporous material with zeolitic nanoplugs in the mesopores, a plugged hexagonal templated [89,90] (PHTS)-like material can be formed (Figure 3a) [85]. PHTS is a mesoporous material, which is obtained by increasing the silica/surfactant ratio in the SBA-15 synthesis. The excess amount of silica source gives rise to the formation of amorphous microporous plugs inside the mesochannels of SBA-15, resulting in a PHTS material with both open and narrowed pores. In the case of a coating inside the pores of the mesoporous support, a decrease in the mesopore diameter is observed (Figure 3b) [85]. Notice that this synthesis approach not only leads to the formation of a combined zeolitic/mesoporous material, but also enables the study of the zeolite nanoparticles. A drawback of this method is that the active sites are only located in the coating/plugs and not throughout the mesoporous structure itself [85]. In addition, as previously mentioned, the small dimensions of the nanoparti-

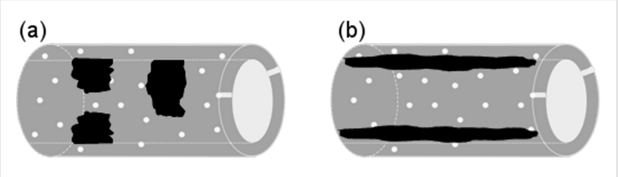

Figure 3: Schematic representation of (a) a plugged and (b) a coated material, obtained by the postsynthetic deposition of zeolite nanoparticles into SBA-15. Reprinted with permission from [85]. Copyright 2011 American Chemical Society.

cles often alter the properties of the materials as compared to the full-grown zeolite (e.g., hydrophilicity) [83,85,91]. Nevertheless, examples of beneficial materials obtained by the postsynthetic deposition approach also exist, namely the TS-1 coated MCF structure developed by D. Trong-On [79,82], which shows a higher activity for the oxidation of 1-naphthol than the mesoporous Ti-MCF material and the TS-1 zeolite.

Delamination: This technique is only applicable for those zeolites (i.e., MCM-22 and ferrierite) that have lamellar structures (Figure 4) [47,92-94]. First, the as synthesized zeolite precursor [MCM-22(P)] (with the microtemplate still in the structure) is allowed to interact with a surfactant, resulting in a swollen, intercalated structure. After removal of the surfactant, the intercalated structure is exfoliated and collapses to form a highly mesoporous material made of randomly packed zeolite sheets with the microporous structure of the parent zeolite [ITQ-2] preserved. Here, all active sites are directly accessible from the external surface, but only a limited control over the resulting mesopore size is possible. Ti-containing ITQ-2 structures can be obtained by grafting of titanocene complexes. These turn out to be excellent catalysts for the epoxidation of olefins [95].

1.2.2 Templating approach

In templating approaches, combined zeolitic/mesoporous materials are obtained by using appropriate templates. Strictly speaking, the term "templating approach" relates to the mesotemplate and not to the microtemplate. This is because in all the templating strategies, only the type of mesotemplate is changed and not the microtemplate.

In general, a distinction is made between hard (or solid, or textural) and soft templates, which reflects the physical nature of the mesotemplates, analogous to the distinction that is made in the syntheses of the purely mesoporous materials. The most frequently used hard templates are carbon-based, biological and polymeric ones, whereas the soft templates are the typical molecular organized systems (MOS) and polymeric organized systems (POS), mostly identical to the surfactants applied for the formation of purely mesoporous materials. Other surfactants are also being developed specifically for their beneficial influence on the formation of mesoporous materials with zeolitic character.

Hard templating route: Here, the zeolite is grown in the presence of a solid material. First, a solution of zeolite nanoparticles (precursor solution of a full-grown zeolite: See postsynthetic deposition) is prepared, before being combined with a hard template. Then, the mixture is subjected to a hydrothermal treatment so that the zeolite can be formed in or around the solid "mould". Finally, the zeolite structure-directing agent as well as the hard template are removed, resulting in the formation of a mesoporous zeolite with a structure that is fully determined by the morphology of the hard template and the zeolite [20,47,48,50].

Carbon-based templates are the most common type of hard template. The concept of using carbon in combination with zeolites was first applied to obtain nanosized zeolites in the so-called confined-space synthesis, whereby zeolites were grown inside the voids of porous carbon [47,96]. However, by altering the synthesis conditions, it is also possible to completely encapsulate the porous carbon matrix [97], resulting

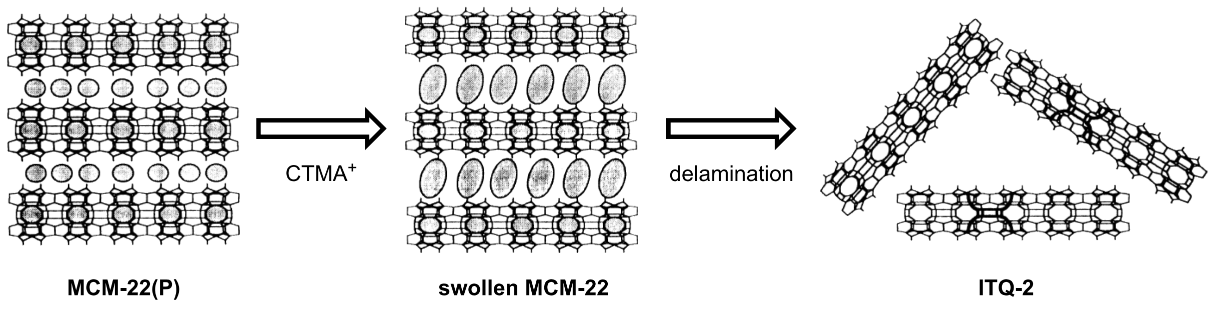

Figure 4: Schematic representation of the delamination process (CTMA$^+$ = cetyltrimethylammonium ion). Reprinted from [93]. Copyright 2000, with permission from Elsevier.

in the formation of mesoporous zeolite crystals (Figure 5) [98]. A wide variety of carbon templates can be used, such as carbon black [99-101], ordered mesoporous carbons (CMKs) [102,103], carbon nanotubes [104], and carbon nanofibers [105]. The choice of template is crucial for the final material, since the mesoporous zeolites essentially become replicas of the carbon pore system in which they grow. For example, with carbon black, the resulting pores will be nonuniform with no interconnection. However, this does not mean that these materials are not useful: Park et al. [101] described the use of carbon-templated mesoporous TS-1 for the epoxidation of cyclic olefines. Carbon nanotubes, on the other hand, give rise to uniform, straight mesopores, but are a more expensive alternative. The most promising, but also most expensive, carbon templates are the CMKs. These carbons are replicas or inverse replicas of existing mesoporous silicates, such as MCM-48 (CMK-1) [106] and SBA-15 (CMK-3 [107] and CMK-5 [108]). By impregnation of the CMKs with zeolite nanoparticles, replicated mesoporous materials (RMMs) are formed with a tunable degree of zeolitic character and a wide choice in mesoporosity [102]. This synthesis strategy is very appealing, since it is applicable to practically all zeolites and offers a fairly good control over the porosity. However, it is an expensive technique with potential health, safety and environmental issues, because of the high production costs and the need for extensive combustion to remove the carbon [50].

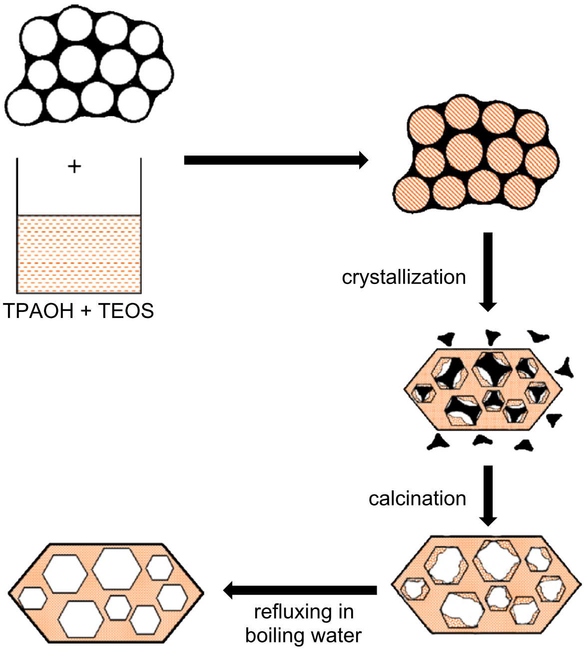

Figure 5: Schematic representation of the carbon-based hard-templating route for the formation of mesoporous silicalite-1 (MFI) zeolite. In the first step, the zeolite precursor solution is combined with a mesoporous carbon template (= black matrix). Then the zeolite is crystallized and the crystals entirely or partially encapsulate the porous carbon. In addition, amorphous silica is also formed. The carbon matrix is removed by calcination. Finally, the amorphous silica is dissolved by refluxing the material in boiling water, resulting in the formation of mesoporous silicalite-1. Reprinted from [98]. Copyright 2007, with permission from Elsevier.

Aerogel, polymer, resin and biological templates can also be used as hard templates [20,47], although the number of publications is lower than for carbon-templated combined zeolitic/mesoporous materials. Carbonized as well as noncarbonized resorcinol–formaldehyde (RF) aerogels can be applied [109-112]. They both have a tunable degree of porosity, for example, by altering the RF-ratio. Nevertheless, the noncarbonized RF aerogels are inherently less porous than the carbonized ones. Another option is to use polystyrene [113], latex [114] or resin spheres or beads [115], although they are mostly used for macrotemplating. Also biological templates, such as starch [116], bacterial threads [117], wood cells [118], leaves and stems of plants [119], have been put forward as relatively inexpensive and abundantly available templates.

Soft templating route: When synthesizing combined zeolitic/mesoporous materials by the soft templating route, mesopores are formed by using, in most cases, the same surfactants (MOS/POS) as for regular mesoporous materials [33]. The large difference with the standard synthesis of mesoporous materials is that zeolite nanoparticles (zeolite precursor solution) are used as the silica (and heteroelement) source [44,47,48]. The goal is that the nanoparticles organize themselves around the surfactant assemblies and that they form the zeolitic walls of the resulting combined zeolitic/mesoporous material. A distinction is made between one-pot [52,57,120-122] and two-pot [51,123-135] templating strategies. In the latter case, the zeolite nanoparticles are formed beforehand in a separate reaction vessel. Subsequently, these nanoparticles are added to a mesotemplate solution, hence the term "two-pot". In a one-pot synthesis on the other hand, the micro- and mesotemplates, together with the silica (and heteroelement) source, are all added to the same reaction vessel (at the same time). In this way, the mesopores and zeolite formation is intended to occur in one pot and ideally simultaneously. An example of a successful two-pot synthesis is the formation of MTS-9, a mesoporous titanosilicate with primary and secondary building units similar to TS-1 [51], and which shows a strong oxidation ability in the (substituted-) phenol hydroxylation and exhibits a high hydrothermal stability. Also one-pot templating approaches have already given rise to promising materials, such as Ti-MMM-1 [52], which is a much more selective catalyst for the oxidation of octane and cyclohexane than are Ti-MCM-41 or TS-1. Although various highly active materials have been developed through the soft templating method, in practice it is not clear whether the resulting materials are true hierarchical mesoporous zeolites. Indeed, unambiguous proof regarding this matter is often not supplied. In one of our papers [136], we demonstrated that it is not possible to obtain a true hierarchical mesoporous zeolite by applying a simple one-pot templating synthesis strategy, based on a TS-1 recipe. Here, part of the microtemplate (tetrapropylammoniumhydroxide) was replaced by a standard mesotemplate (cetyltrimethylammoniumbromide). We showed that because of the inherent competition between zeolite and mesopore formation, the creation of a mesoporous zeolite is inhibited. However, although no true hierarchical structure can be obtained, optimizing the synthesis parameters does lead to the formation of a combined zeolitic/mesoporous material with a pronounced zeolitic character and a high mesoporosity, denoted as meso-TSM [136,137]. This material can be used as redox catalyst in the epoxidation of cyclohexene [85].

An advanced one-pot templating synthesis that does guarantee the formation of a true hierarchical mesoporous zeolite [138-141] is the use of tailor-made organic–inorganic hybrid surfactants. Here, a silylated surfactant is applied in combination with a synthesis gel with the composition of a zeolite. The covalent bonding between the zeolite precursors and the organosilane surfactant avoids the expelling of the surfactant-based mesostructure out of the crystallization of the zeolite phase during the synthesis (Figure 6). The number of publications on these tailor-made surfactants keeps on rising [60,142-146]. Recently, Ryoo and coworkers [143-146] developed new types of bifunctional surfactants (di- and polyquaternary ammonium surfactants) that combine the functionalities of a mesotemplate with those of a zeolite structure-directing agent. In this way, a single surfactant is able to direct the formation of mesoporous zeolites. The main drawback of this method is the use of non-commercially available, exotic and therefore expensive surfactants.

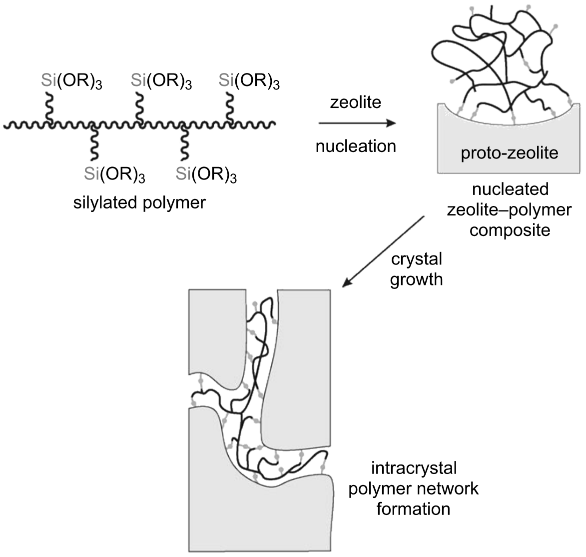

Figure 6: Conceptional approach for the synthesis of a mesoporous zeolite with a silylated surfactant as mesotemplate. Reprinted from [141]. Copyright 2006, with permission from John Wiley and Sons.

Table 2: Prices of templates used for the synthesis of nanoporous materials [50].

template	price per kg template (€)	price per kg final material (€)
CTMABr	530	387
P123	100	55
carbon nanofibers	2520	1814
carbon particles	6150	4551

1.2.3 Nontemplating approach

Since the price of mesotemplates is quite high (Table 2) [50] and their use gives rise to possible environmental risks, researchers have also explored the development of combined zeolitic/mesoporous materials by nontemplating approaches [147-154]. More specifically, these approaches are in the absence of templates for the mesopores, but the zeolite structure-directing agent is still used.

Mesotemplate-free synthesis: In 2008, Stevens et al. [147] reported the formation of a mesoporous material by acidic hydrothermal assembly of silicalite-1 nanoparticles in the absence of a mesotemplate. The crucial step in this synthesis is the acidification of the solution containing the zeolite precursor, which results in a ligand loss of the microtemplate [83]. In this way, the nanoparticles are not able to develop into a full-grown zeolite. Instead, they form assemblies by edge-sharing (Figure 7a), similar to the case in sol–gel synthesis [155], resulting in interparticle mesoporosity. The drawback in this synthesis approach is that it is a random process, which means that a proper control of the porosity is rather difficult and ordering of the mesopores is not possible. Moreover, in the specific case of silicalite-1, the resulting material does not show any long-range zeolitic character [147]. However, when using Beta nanoparticles [148], it is possible to obtain a combined zeolitic/mesoporous material with pronounced zeolitic features, although not as a “true” hierarchical system.

Another example of a template-free synthesis is the formation of TUD-C and TUD-M materials [149-152] (Figure 7b). The synthesis is also executed with zeolite nanoparticles, but in a basic medium instead of under acidic conditions. Here, the microtemplate will not only direct the micropore formation, but

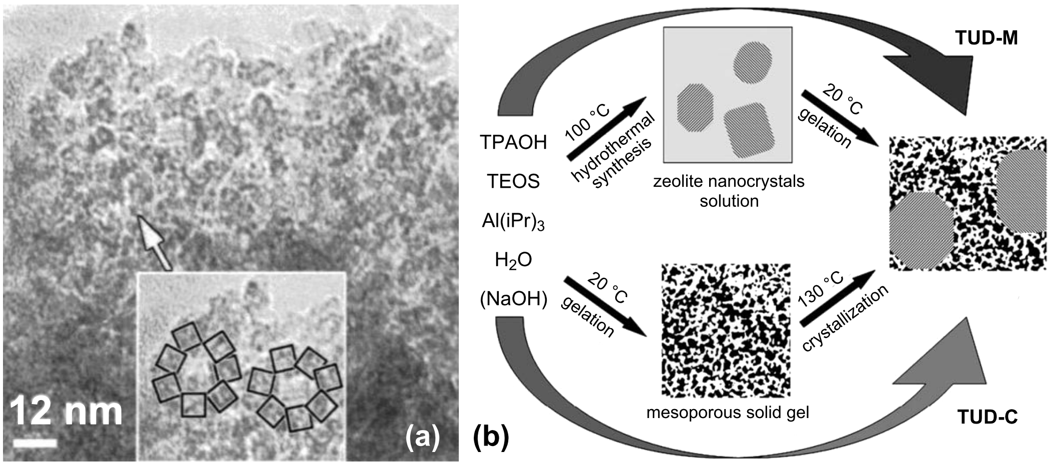

Figure 7: (a) Edge-sharing principle in the template-free synthesis in acidic medium [147] and (b) schematic representation of the TUD-C and TUD-M synthesis [152]. Reprinted from [147,152]. Copyright 2008 and 2009, with permission from Elsevier.

will also act as a scaffolding agent enabling the creation of a material combining zeolitic domains with a disordered amorphous mesoporous matrix. An advantage of this mesotemplate-free method in comparison with the former one is that leaching of the heteroelements (e.g., Al and Ti) will occur to a minor extent due to the basic synthesis conditions.

Self-formation mechanism of hierarchy: The phenomenon of self-formation of porosity was first seen in the synthesis of metal oxides starting from metal alkoxides in water droplets (Figure 8) [154,156]. Here, the hydrolysis and condensation induce the formation of small molecules, namely water and alcohol, which then create porosity in a random manner. Recently Su and coworkers [153,154] extended this method to the synthesis of zeolites (TS-1; Beta; ZSM-5), whereby amorphous metaloxides are impregnated with microtemplates. This results in the formation of combined micro-, meso- and macroporous materials with zeolitic features. Since this approach is very new, the exact formation mechanism and detailed structural properties of the materials need to be explored in more detail before drawing any conclusion on its applicability.

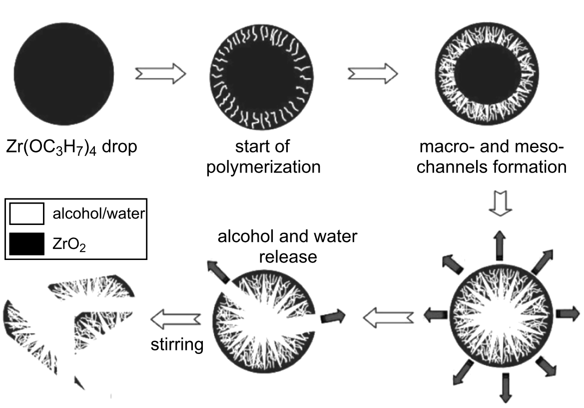

Figure 8: Schematic representation of the formation of micro-meso-macroporous metal oxides (zirconia) [154]. Reproduced by permission of The Royal Society of Chemistry.

1.2.4 Conclusion

As pointed out in the preceding paragraphs, each synthesis strategy for the formation of combined zeolitic/mesoporous materials has its advantages and disadvantages. Table 3 summarizes the most important characteristics of the different approaches. The choice of which synthesis strategy is the most suitable one should always depend on the type of application that is being aimed at and on the resources available. A trade-off needs to be made between these two aspects in order to decide which route to follow. Nevertheless, it should be pointed out that the combined zeolitic/mesoporous materials often have properties deviating from those of the zeolites and the amorphous mesoporous materials, depending on the applied synthesis method. This is due to the frequently occuring local differences in the active elements caused by differences in the extent of the zeolitic character as well as differences in diffusional behavior. A lot more research and in-depth characterization of the combined zeolitic/mesoporous materials is needed to fully understand their potential and the differences between these types of materials and their zeolitic and mesoporous counterparts.

2 Catalysis and Ti-containing siliceous materials

Proper control of the synthesis parameters, elucidation of the formation mechanism and thorough characterization of

Table 3: Comparison of the feasibility of the most important strategies for the synthesis of combined zeolitic/mesoporous materials (based on all the references used in this review).

approach	zeolitic character	level of mesoporosity	control over the mesopore structure	degree of interconnection	applicability to different types of zeolites and mesoporous materials	production costs
demetallation	high	medium	medium	low	medium–high	medium
recrystallization	medium	medium	medium	low	high	high
deposition	low	medium–high	high	low	high	high
delamination	high	low	low	low	low	high
hard templating	high	high	high	low–high	high	high–medium
soft templating	low–medium	high	medium–high	low–medium	high	high
template-free	low–medium	medium	low	medium	medium	medium
self-formation	—[a]	—[a]	low	—[a]	—[a]	medium

[a] Insufficient knowledge/examples/studies reported to make an assessment.

nanoporous materials are essential to lead to the successful implementation of nanoporous materials in (industrial) chemical processes. The field in which nanoporous materials are applied most frequently is in heterogeneous catalysis. Therefore, in the next few paragraphs, the use of Ti-containing siliceous materials as catalysts will be discussed. Focus is particularly put on the already existing industrial applications and on those (lab-scale) applications with a high potential.

2.1 Link between catalysis and Ti-coordination

In the specific case of Ti-containing materials, the catalytic activity is ascribed to the presence of Ti(IV) in its structure [157]. These Ti(IV) sites are considered as redox-active centers [11,158]. Therefore, the typical reactions that can be catalyzed by Ti-containing materials are reactions in which electron exchange plays a key role, i.e., oxidation and reduction reactions [157]. Next to the amount of Ti present in the nanoporous materials, an equally important aspect that will have a large influence on the catalysis is the Ti coordination. Table 4 gives an overview of the different techniques that can be applied to determine the coordination. TiO_x species can be present in a number of different coordinations, namely 4-, 5- and 6-fold [157]. Among these configurations, the isolated, 4-fold or tetrahedrally coordinated form is the most preferred one since this means that Si is perfectly isomorphically substituted by Ti in the structure, like in the full-grown zeolite TS-1 (Figure 9). This specific coordination gives rise to a high, and often unique, catalytic activity in oxidation processes (see further). A 5- and 6-fold coordination is often less wanted, since these species tend to form clusters (oligomerization) [167] and are correlated with defect sites in the titanosilicate structure [168]. When this oligomerization process goes even further, small TiO_2 (crystalline anatase) particles can occur as extra-framework material, which is not built in the structure. Although crystalline TiO_2 particles are well-known for their interesting semiconductor properties and their photocatalytic activity in photodegradation processes [169], TiO_2 formation often needs to be avoided in the synthesis of Ti-containing nanoporous siliceous materials since its presence can be detrimental for the catalytic activity associated with tetrahedrally coordinated Ti [170,171].

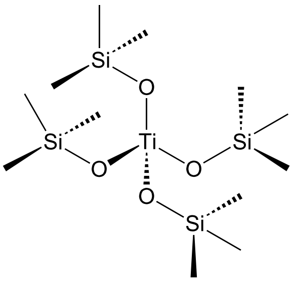

Figure 9: Isolated, tetrahedrally coordinated Ti(IV) site. Reprinted from [168]. Copyright 2008, with permission from Elsevier.

Table 4: Overview of characterization techniques for the determination of Ti-coordination.

technique	references
UV–vis diffuse reflectance spectroscopy	[159]
photoluminescence IR spectroscopy	[160]
X-ray absorption spectroscopy (e.g., EXAFS, XANES, etc.)	[161-163]
vibrational spectroscopy (infrared and Raman)	[164,165]
electron paramagnetic resonance	[166]

2.2 Redox catalysis

Titanium-silicalite-1 – A versatile redox catalyst: Titanium-silicalite-1 is a textbook example of a successful heterogeneous catalyst. This zeolite is considered as one of the most versatile redox catalysts available [157,172]. TS-1 currently finds application in various oxidation processes with H_2O_2 as oxidant (Figure 10), such as the epoxidation of alkenes [173], hydroxylation of aromatics [174-176], cyclization reactions [177], oxidation of alcohols [178,179] and ammoximation of ketones [180]. The strength of TS-1 as catalyst is attributed to (i) its shape-selectivity; (ii) its hydrophobic nature, enabling the preferential adsorption of the hydrophobic substrates also in the presence of water and (iii) its isolated, tetrahedrally coordinated Ti sites, preventing the undesired decomposition of H_2O_2 [181]. The active species in all the oxidation processes are believed to be an oxo-titanium complex formed by the interaction of H_2O_2 with Ti ions [162,181]. However, there is still no consensus on the exact structure of the Ti-peroxide complex in TS-1 (Figure 11).

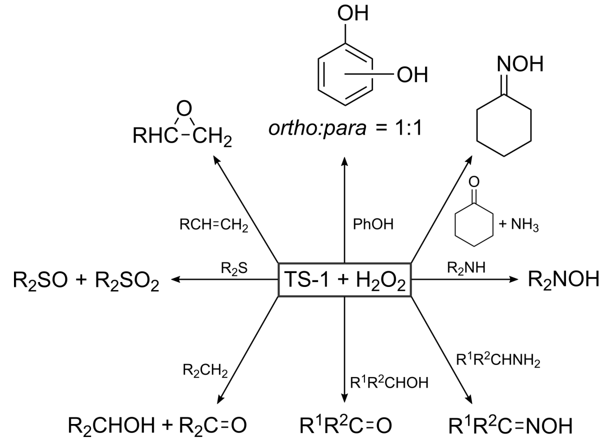

Figure 10: Schematic overview of the versatility of TS-1 as redox catalyst [172]. Reproduced with permission of Russian Chemical Reviews.

Three processes have been industrialized over the past years, and this clearly reflects the importance of TS-1 for oxidation catalysis (the three upper reactions in Figure 10) [171,172,182,183]:

1. Hydroxylation of phenol: This reaction occurs in aqueous or aqueous-organic medium producing a mixture of hydroquinone (*p*-dihydroxybenzene) and catechol (*o*-dihydroxybenzene), which can be used as a reducing agent and precursor in fine chemistry. Water and tarlike compounds are the major byproducts. Conversion and selectivity are significantly higher than those achieved by acidic and radical catalysts. Therefore, since 1986, a plant near Ravenna, Italy, is producing 10,000 tons per year of diphenols with the aid of TS-1 as catalyst.
2. Ammoximation of cyclohexanone: This reaction is of major interest as cyclohexanone oxime is the intermediate in the manufacturing of caprolactam, the monomer for nylon 6. Conversion and selectivity of cyclohexanone to oxime is over 99% and the yield based on H_2O_2 is over 90%. Both Enichem as well as Sumitomo Chemical Co. operate such a TS-1 based caprolactam plant.
3. Epoxidation of propylene: Propylene oxide is one of the largest propene derivatives in production, ranking second behind polypropylene, and is primarily used as a reactive chemical intermediate. The “older” synthesis processes, such as the chlorohydrin route, generate a huge amount of byproducts, for example, for each ton of propylene oxide, 2 t of $CaCl_2$ is obtained. In addition, 1.4 t of chlorine, 1.0 t of $Ca(OH)_2$ and a large excess of water are needed. However, recently, BASF/Dow and Degussa-Evonik/Headwaters developed a new technology based on the use of aqueous solutions of H_2O_2 and a fixed-bed TS-1 reactor. At the end of 2008, the largest plant using this new process was started up in Antwerp by BASF/Dow.

Although the implementation of TS-1 has been successful, there are still some challenges left. Firstly, the use of H_2O_2 as oxidant is rather costly, which requires a low catalyst cost and very high process performance in order to meet economic targets. Therefore, researchers have been studying the possibility of H_2O_2 generation in situ, from H_2 and O_2 [182]. Secondly, like all zeolites, TS-1 suffers from accessibility and diffusion limitation problems for large and bulky molecules. For example, molecules with a kinetic diameter equal to or larger than cyclo-

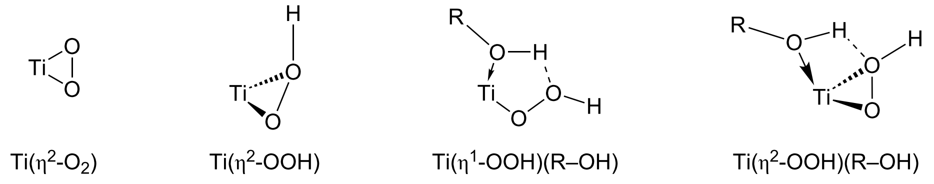

Figure 11: Different oxo-titanium species in TS-1. R–OH is a co-adsorbed alcohol molecule, stabilizing the hydroperoxide complex.

hexene are practically excluded from epoxidation reactions with TS-1 [85,184]. In general, high-value fine chemicals are usually too large to fit into the pores of the MFI structure of TS-1. This is one of the driving forces to synthesize larger pore titanosilicates.

Large-pore Ti-containing siliceous materials: As anticipated, larger pore Ti-activated siliceous materials, such as Ti-MCM-41 and Ti-SBA-15, are indeed able to catalyze oxidation reactions with bulky reactants [85,157,167,172,185,186]. Especially in epoxidations with large alkenes, such as limonene [167,186], mesoporous materials give rise to much higher activities than TS-1. However, although these mesoporous materials have clear advantages, they also suffer some major drawbacks: (i) They are less stable than TS-1, and especially the hydrothermal stability is significantly lower, and (ii) their hydrophilic nature, which is caused by their amorphous structure, leads to a lower catalytic activity [183,187]. This hydrophilicity will prevent efficient adsorption of the nonpolar/organic reactants, since the mesoporous materials show more affinity for water (from the aqueous H_2O_2 solution). By using an organic peroxide, such as *t*-butylhydroperoxide (TBHP), as oxidant, the catalytic activities can be remarkably improved [188]. Likewise, silylation of the surface of mesoporous materials, resulting in a more hydrophobic structure, is also a solution in many cases [189]. However, this does not solve the stability problems.

Combined zeolitic/mesoporous materials are expected to help to overcome these stability and hydrophilicity issues. Some successful examples have already been reported in the literature [51,52,58,59,78,79,82,122]. For example, MTS-9 [52] shows a high hydrothermal stability (over 120 hours in boiling water) and a high oxidation ability for small (phenol and styrene) as well as larger molecules (2,3,6-trimethylphenol) with 30% aqueous H_2O_2 as oxidant. As mentioned above, this material is formed in a two-pot templating strategy, wherein preformed, nanosized titanosilicate precursors are combined with polymer surfactants. Its high activity has been ascribed to the TS-1-like Ti-species present in MTS-9 and the fact that its relatively thick pore walls (4.8 nm) contain primary and secondary structural building units, similar to TS-1. Another nice example is Ti-MMM-2 [122], a one-pot templated material with a microporous TS-1 phase and a mesoporous Ti-MCM-48 phase. This material shows a higher activity (61%) than both TS-1 (16%) and Ti-MCM-48 (42%) for the epoxidation of cyclohexene with TBHP (in decane) as oxidant. Although the difference in catalytic activity was compared to the purely mesoporous material and the zeolite, no data concerning the stability are reported, nor data with H_2O_2 as oxidant. The fact that an organic peroxide is used as oxidant instead of H_2O_2, meaning a more hydrophobic medium instead of a hydrophilic one, can by itself lead to differences in the catalytic performance of nanoporous materials (as mentioned above for the purely mesoporous materials). Reichinger et al. [59] investigated the effect of the reaction medium by performing the cyclohexene epoxidation in both a hydrophobic and a hydrophilic environment. The studied material was a mesoporous structure assembled from TS-1 nanoparticles. This material outperformed TS-1 and Ti-MCM-41 in the cyclohexene epoxidation, both under hydrophobic conditions (TBHP and decane) and under hydrophilic conditions (H_2O_2 and water/ CH_3OH). However, in the epoxidation of the smaller molecule 1-hexene, the (more hydrophilic) combined zeolitic/mesoporous material failed completely in the hydrophilic medium whereas the hydrophobic TS-1 zeolite showed a high catalytic activity. These experiments perfectly exemplify the need for (i) a suitable combination of the reagents and the pore dimensions of the catalyst and (ii) the importance of compatibility between the characteristics of the materials and the reactions conditions (e.g., hydrophilicity). Here, also no information on the stability of the combined materials was given. On the other hand, not all combined zeolitic/mesoporous materials outperform their purely zeolitic or mesoporous counterparts. We recently studied three types of combined zeolitic/mesoporous materials in the epoxidation of cyclohexene with H_2O_2 [85]. Here, two materials were obtained by postsynthetic deposition of TS-1 nanoparticles on SBA-15 (SBA-TS-15-pH 1 and SBA-TS-15-pH 13) and one structure was formed by a one-pot templating approach (meso-TSM). Both SBA-TS-15 materials showed similar (low) activity as compared to TS-1, while the performance of meso-TSM lay in between TS-1 and Ti-MCM-41. In the case of meso-TSM, combined zeolitic/mesoporous materials did not give rise to an enhanced performance in comparison with their purely mesoporous counterparts. Also Chenevieve et al. [60] observed that their titanosilicates with a mesoporous or microporous hierarchical structure did not possess the superior catalytic properties expected for hierarchical catalysts: In particular, the gain in diffusion properties was totally inhibited by the increase in hydrophilic character of the material.

Notice that divergent catalytic behavior is observed, which highly depends on the properties of the materials and on the synthesis method for the formation of the titanosilicates. Moreover, important information on these Ti-containing combined zeolitic/mesoporous materials concerning stability, regenerability and scaling up is often lacking or not yet investigated. Therefore, more research concerning their structural properties and catalytic behavior is necessary to fully explore and understand the catalytic potential of the combined zeolitic/mesoporous materials. At the moment, it is still too early to tell whether industrialization of these combined zeolitic/mesoporous materials as redox catalysts can be expected in the near future. However, major progress is to be expected in this area of research.

Conclusion

This review highlighted the most common synthesis approaches for the formation of combined zeolitic/mesoporous materials. These materials have been gaining a lot of interest during the last decade, since they are an attempt to combine the superior properties of zeolites (high stability, catalytic activity and selectivity) with those of mesoporous materials (improved diffusion and accessibility for larger molecules and viscous fluids). Some of the synthesis strategies have been extrapolated from the synthesis of purely mesoporous materials (e.g., the two-pot templating approach) whereas others have been newly developed or specifically designed for the formation of combined zeolitic/mesoporous materials (e.g., one-pot templating approach with organosilane surfactants and postsynthetic routes). All synthesis methods have their advantages and disadvantages, meaning that there is no obviously superior synthesis strategy. Therefore, the applied synthesis approach should depend on the final application, the desired properties of the materials and the resources available. Moreover, a lot more research on the combined zeolitic/mesoporous materials is needed to fully understand the discrepancies between these types of materials and their zeolitic and mesoporous counterparts. With regards to the Ti-containing combined zeolitic/mesoporous materials as redox catalysts, a lot of progress has been made in recent years with the development of interesting materials, especially for oxidation reactions of bulky molecules. However, sufficient information on the local structural properties and diffusion behavior of the various synthesized materials in relation to the synthesis methodology is still lacking. In addition, important information concerning the stability, regenerability and scaling up of these combined materials is still missing, making it difficult to draw a conclusion on their potential (industrial) implementation. Therefore, further investigation is necessary in order to fully explore the (catalytic) potential of the combined zeolitic/mesoporous materials.

Acknowledgements

J. Vernimmen thanks the Fund for Scientific Research-Flanders (FWO-Vlaanderen) for financial support.

References

1. Kholdeeva, O. A.; Mel'gunov, M. S.; Shmakov, A. N.; Trukhan, N. N.; Kriventsov, V. V.; Zaikovskii, V. I.; Malyshev, M. E.; Romannikov, V. N. *Catal. Today* **2004,** *91–92,* 205–209. doi:10.1016/j.cattod.2004.03.034
2. Corma, A. *J. Catal.* **2003,** *216,* 298–312. doi:10.1016/S0021-9517(02)00132-X
3. Kulkarni, S. J. *Stud. Surf. Sci. Catal.* **1998,** *113,* 151–161. doi:10.1016/S0167-2991(98)80282-6
4. Bartholomew, C. H.; Farrauto, R. J. *Fundamentals of industrial catalytic processes,* 2nd ed.; John Wiley & Sons: Hoboken, N. J., 2006.
5. Dyer, A. *An introduction to zeolite molecular sieves;* John Wiley & Sons: Chichester, N. Y., 1988.
6. Doadrio, A. L.; Sousa, E. M. B.; Doadrio, J. C.; Pérez Pariente, J.; Izquierdo-Barba, I.; Vallet-Regi, M. *J. Controlled Release* **2004,** *97,* 125–132. doi:10.1016/j.jconrel.2004.03.005
7. Pasqua, L.; Cundari, S.; Ceresa, C.; Cavaletti, G. *Curr. Med. Chem.* **2009,** *16,* 3054–3063. doi:10.2174/092986709788803079
8. Sousa, A.; Souza, K. C.; Sousa, E. M. B. *Acta Biomater.* **2008,** *4,* 671–679. doi:10.1016/j.actbio.2007.11.003
9. Vallet-Regi, M. *Chem.–Eur. J.* **2006,** *12,* 5934–5943. doi:10.1002/chem.200600226
10. Zhou, C. F.; Zhu, J. H. *Chemosphere* **2005,** *58,* 109–114. doi:10.1016/j.chemosphere.2004.08.056
11. Arends, I. W. C. E.; Sheldon, R. A. *Appl. Catal., A* **2001,** *212,* 175–187. doi:10.1016/S0926-860X(00)00855-3
12. Djaeni, M.; Bartels, P.; Sanders, J.; van Straten, G.; van Boxtel, A. J. B. *Drying Technol.* **2007,** *25,* 225–239. doi:10.1080/07373930601161096
13. Kang, T.; Park, Y.; Choi, K.; Lee, J. S.; Yi, J. *J. Mater. Chem.* **2004,** *14,* 1043–1049. doi:10.1039/b315829b
14. Satsuma, A.; Yang, D. J.; Shimizu, K. *Microporous Mesoporous Mater.* **2011,** *141,* 20–25. doi:10.1016/j.micromeso.2009.12.002
15. Coronas, J.; Santamaria, J. *Chem. Eng. Sci.* **2004,** *59,* 4879–4885. doi:10.1016/j.ces.2004.08.001
16. Shindo, T.; Kudo, H.; Kitabayashi, S.; Ozawa, S. *Microporous Mesoporous Mater.* **2003,** *63,* 97–104. doi:10.1016/S1387-1811(03)00435-9
17. Shariatmadari, F. *World's Poult. Sci. J.* **2008,** *64,* 76–84. doi:10.1017/S0043933907001730
18. Taguchi, A.; Schüth, F. *Microporous Mesoporous Mater.* **2005,** *77,* 1–45. doi:10.1016/j.micromeso.2004.06.030
19. Taramasso, M.; Perego, G.; Notari, B. Preparation of porous crystalline synthetic material comprised of silicon and titanium oxides. U.S. Patent 4410501, Oct 18, 1983.
20. Tao, Y.; Kanoh, H.; Abrams, L.; Kaneko, K. *Chem. Rev.* **2006,** *106,* 898–910. doi:10.1021/cr040204o
21. Tosheva, L.; Valtchev, V. P. *Chem. Mater.* **2005,** *17,* 2494–2513. doi:10.1021/cm047908z
22. Zhao, D.; Feng, J.; Huo, Q.; Melosh, N.; Fredrickson, G. H.; Chmelka, B. F.; Stucky, G. D. *Science* **1998,** *279,* 548–552. doi:10.1126/science.279.5350.548
23. Zhao, D.; Huo, Q.; Feng, J.; Chmelka, B. F.; Stucky, G. D. *J. Am. Chem. Soc.* **1998,** *120,* 6024–6036. doi:10.1021/ja974025i
24. Kresge, C. T.; Leonowicz, M. E.; Roth, W. J.; Vartuli, J. C.; Beck, J. S. *Nature* **1992,** *359,* 710–712. doi:10.1038/359710a0
25. Beck, J. S.; Vartuli, J. C.; Roth, W. J.; Leonowicz, M. E.; Kresge, C. T.; Schmitt, K. D.; Chu, C. T.-W.; Olsen, D. H.; Sheppard, E. W.; McCullen, S. B.; Higgins, J. B.; Schlenker, J. L. *J. Am. Chem. Soc.* **1992,** *114,* 10834–10843. doi:10.1021/ja00053a020

26. Vartuli, J. C.; Schmidt, K. D.; Kresge, C. T.; Roth, W. T.; Leonowicz, M. E.; McCullen, S. B.; Hellring, S. D.; Beck, J. S.; Schlenker, J. L.; Olson, D. H.; Sheppard, E. W. *Chem. Mater.* **1994,** *6,* 2317–2326. doi:10.1021/cm00048a018
27. Bagshaw, S. A.; Prouzet, E.; Pinnavaia, T. J. *Science* **1995,** *269,* 1242–1244. doi:10.1126/science.269.5228.1242
28. Prouzet, E.; Cot, F.; Nabias, G.; Larbot, A.; Kooyman, P.; Pinnavaia, T. J. *Chem. Mater.* **1999,** *11,* 1498–1503. doi:10.1021/cm9810281
29. Kim, S.-S.; Liu, Y.; Pinnavaia, T. J. *Microporous Mesoporous Mater.* **2001,** *44–45,* 489–498. doi:10.1016/S1387-1811(01)00225-6
30. Park, I.; Pinnavaia, T. J. *Microporous Mesoporous Mater.* **2009,** *118,* 239–244. doi:10.1016/j.micromeso.2008.08.027
31. Blin, J. L.; Léonard, A.; Su, B.-L. *J. Phys. Chem. B* **2001,** *105,* 6070–6079. doi:10.1021/jp0036442
32. Schmidt-Winkel, P.; Lukens, W. W., Jr.; Yang, P.; Margolese, D. I.; Lettow, J. S.; Ying, J. Y.; Stucky, G. D. *Chem. Mater.* **2000,** *12,* 686–696. doi:10.1021/cm991097v
33. de A. A. Soler-Illia, G. J.; Sanchez, C.; Lebeau, B.; Patarin, J. *Chem. Rev.* **2002,** *102,* 4093–4138. doi:10.1021/cr0200062
34. Meynen, V.; Cool, P.; Vansant, E. F. *Microporous Mesoporous Mater.* **2009,** *125,* 170–223. doi:10.1016/j.micromeso.2009.03.046
35. Corma, A. *Chem. Rev.* **1997,** *97,* 2373–2419. doi:10.1021/cr960406n
36. Valdés-Solís, T.; Fuertes, A. B. *Mater. Res. Bull.* **2006,** *41,* 2187–2197. doi:10.1016/j.materresbull.2006.04.018
37. Liu, T.; Burger, C.; Chu, B. *Prog. Polym. Sci.* **2003,** *28,* 5–26. doi:10.1016/S0079-6700(02)00077-1
38. Cassiers, K.; Linssen, T.; Mathieu, M.; Benjelloun, M.; Schrijnemakers, K.; Van Der Voort, P.; Cool, P.; Vansant, E. F. *Chem. Mater.* **2002,** *14,* 2317–2324. doi:10.1021/cm0112892
39. Wu, P.; Tatsumi, T.; Komatsu, T.; Yashima, T. *Chem. Mater.* **2002,** *14,* 1657–1664. doi:10.1021/cm010910v
40. Newalkar, B. L.; Olanrewaju, J.; Komarneni, S. *Chem. Mater.* **2001,** *13,* 552–557. doi:10.1021/cm000748g
41. Zhang, W. H.; Lu, J. Q.; Han, B.; Li, M. J.; Xiu, J. H.; Ying, P. L.; Li, C. *Chem. Mater.* **2002,** *14,* 3413–3421. doi:10.1021/cm011686c
42. Chen, Y. Y.; Huang, Y. L.; Xiu, J. H.; Han, X. W.; Bao, X. H. *Appl. Catal., A* **2004,** *273,* 185–191. doi:10.1016/j.apcata.2004.06.030
43. Koyano, K.; Tatsumi, T. *Microporous Mater.* **1997,** *10,* 259–271. doi:10.1016/S0927-6513(97)00016-3
44. Meynen, V.; Cool, P.; Vansant, E. F. *Microporous Mesoporous Mater.* **2007,** *104,* 26–38. doi:10.1016/j.micromeso.2006.12.003
45. van Donk, S.; Janssen, A. H.; Bitter, J. H.; de Jong, K. P. *Catal. Rev. - Sci. Eng.* **2003,** *45,* 297–319. doi:10.1081/CR-120023908
46. Hartmann, M. *Angew. Chem., Int. Ed.* **2004,** *43,* 5880–5882. doi:10.1002/anie.200460644
47. Egeblad, K.; Christensen, C. H.; Kustova, M.; Christensen, C. H. *Chem. Mater.* **2008,** *20,* 946–960. doi:10.1021/cm702224p
48. Pérez-Ramírez, J.; Christensen, C. H.; Egeblad, K.; Christensen, C. H.; Groen, J. C. *Chem. Soc. Rev.* **2008,** *37,* 2530–2542. doi:10.1039/b809030k
49. Cejka, J.; Mintova, S. *Catal. Rev. - Sci. Eng.* **2007,** *49,* 457–509. doi:10.1080/01614940701583240
50. Chal, R.; Gérardin, C.; Bulut, M.; van Donk, S. *ChemCatChem* **2011,** *3,* 67–81. doi:10.1002/cctc.201000158
51. Meng, X.; Li, D.; Yang, X.; Yu, Y.; Wu, S.; Han, Y.; Yang, Q.; Jiang, D.; Xiao, F.-S. *J. Phys. Chem. B* **2003,** *107,* 8972–8980. doi:10.1021/jp027405l
52. Poladi, R. H. P. R.; Landry, C. C. *Microporous Mesoporous Mater.* **2002,** *52,* 11–18. doi:10.1016/S1387-1811(02)00272-X
53. Ryoo, R.; Kim, J. M.; Ko, C. H.; Shin, C. H. *J. Phys. Chem.* **1996,** *100,* 17718–17721. doi:10.1021/jp9620835
54. Yue, Y. H.; Sun, Y.; Gao, Z. *Catal. Lett.* **1997,** *47,* 167–171. doi:10.1023/A:1019084400340
55. Yun, S. N.; Ryoo, R. *J. Catal.* **2000,** *195,* 237–243. doi:10.1006/jcat.2000.2999
56. Ahn, W. S.; Lee, D. H.; Kim, T. J.; Kim, J. H.; Seo, G.; Ryoo, R. *Appl. Catal., A* **1999,** *181,* 39–49. doi:10.1016/S0926-860X(98)00384-6
57. Huang, L.; Guo, W.; Deng, P.; Xue, Z.; Li, Q. *J. Phys. Chem. B* **2000,** *104,* 2817–2823. doi:10.1021/jp990861y
58. Lin, K.; Sun, Z.; Lin, S.; Jiang, D.; Xiao, F.-S. *Microporous Mesoporous Mater.* **2004,** *72,* 193–201. doi:10.1016/j.micromeso.2004.04.025
59. Reichinger, M.; Schmidt, W.; van den Berg, M. W. E.; Aerts, A.; Martens, J. A.; Kirschhock, C. E. A.; Gies, H.; Grünert, W. *J. Catal.* **2010,** *269,* 367–375. doi:10.1016/j.jcat.2009.11.023
60. Chenevieve, Y.; Chieux, F.; Caps, V.; Tuel, A. *J. Catal.* **2010,** *269,* 161–168. doi:10.1016/j.jcat.2009.11.003
61. de Jong, K. P.; Zecevic, J.; Friedrich, H.; de Jongh, P. E.; Bulut, M.; van Donk, S.; Kenmogne, R.; Finiels, A.; Hulea, V.; Fajula, F. *Angew. Chem., Int. Ed.* **2010,** *49,* 10074–10078. doi:10.1002/anie.201004360
62. Kenmogne, R.; Finiels, A.; Hulea, V.; Zecevic, J.; Friedrich, H.; de Jongh, P. E.; de Jong, K. P.; van Donk, S.; Fajula, F. Hydrocraking of long chain alkanes over Y zeolite with trimodal porosity. In *5th International FEZA Conference: abstracts,* 5th International FEZA Conference, València, Spain, July 3–7, 2011; Universitat Politècnica de València: València, 2011; pp 129–130.
63. Valtchev, V.; Balanzat, E.; Mavrodinova, V.; Diaz, I.; El Fallah, J.; Goupil, J. M. Mesopores Generation in ZSM-5 Crystals by Nuclear Tracks Imprinting. In *5th International FEZA Conference: abstracts,* 5th International FEZA Conference, València, July 3–7, 2011; Universitat Politècnica de València: València, 2011; pp 105–106.
64. Janssen, A. H.; Koster, A. J.; de Jong, K. P. *Angew. Chem., Int. Ed.* **2001,** *40,* 1102–1104. doi:10.1002/1521-3773(20010316)40:6<1102::AID-ANIE11020>3.3.CO;2-Y
65. Groen, J. C.; Moulijn, J. A.; Pérez-Ramírez, J. *J. Mater. Chem.* **2006,** *16,* 2121–2131. doi:10.1039/b517510k
66. Groen, J. C.; Jansen, J. C.; Moulijn, J. A.; Pérez-Ramirez, J. *J. Phys. Chem. B* **2004,** *108,* 13062–13065. doi:10.1021/jp047194f
67. Groen, J. C.; Zhu, W.; Brouwer, S.; Huynink, S. J.; Kapteijn, F.; Moulijn, J. A.; Pérez-Ramírez, J. *J. Am. Chem. Soc.* **2007,** *129,* 355–360. doi:10.1021/ja065737o
68. Verboekend, D.; Pérez-Ramírez, J. *Chem.–Eur. J.* **2011,** *17,* 1137–1147. doi:10.1002/chem.201002589
69. Goa, Y.; Yoshitake, H.; Wu, P.; Tatsumi, T. *Microporous Mesoporous Mater.* **2004,** *70,* 93–101. doi:10.1016/j.micromeso.2004.03.007
70. Pavel, C. C.; Park, S. H.; Dreier, A.; Tesche, B.; Schmidt, W. *Chem. Mater.* **2006,** *18,* 3813–3820. doi:10.1021/cm052261j
71. Kuhn, J.; Gross, J.; Kapteijn, F. *Microporous Mesoporous Mater.* **2009,** *125,* 39–45. doi:10.1016/j.micromeso.2009.01.021
72. Forni, L.; Fornasari, G.; Trifiro, F.; Aloise, A.; Katovic, A.; Giordano, G.; Nagy, J. B. *Microporous Mesoporous Mater.* **2007,** *101,* 161–168. doi:10.1016/j.micromeso.2006.12.013

73. Ivanova, I. I.; Kuznetsov, A. S.; Yuschenko, V. V.; Knyazeva, E. E. *Pure Appl. Chem.* **2004,** *76,* 1647–1658. doi:10.1351/pac200476091647
74. Wang, S.; Dou, T.; Li, Y. P.; Zhang, Y.; Li, X. F.; Yan, Z. C. *Catal. Commun.* **2005,** *6,* 87–91. doi:10.1016/j.catcom.2004.11.005
75. Campos, A. A.; Martins, L.; de Oliviera, L. L.; da Silva, C. R.; Wallau, M.; Urquieta-González, E. A. *Catal. Today* **2005,** *107–108,* 759–767. doi:10.1016/j.cattod.2005.07.007
76. Campos, A. A.; Dimitrov, L.; da Silva, C. R.; Wallau, M.; Urquieta-González, E. A. *Microporous Mesoporous Mater.* **2006,** *1–3,* 92–103. doi:10.1016/j.micromeso.2006.05.006
77. Trong-On, D.; Kaliaguine, S. *Angew. Chem., Int. Ed.* **2001,** *40,* 3248–3251. doi:10.1002/1521-3773(20010903)40:17<3248::AID-ANIE3248>3.0.CO;2-M
78. Trong-On, D.; Lutic, D.; Kaliaguine, S. *Microporous Mesoporous Mater.* **2001,** *44–45,* 435–444. doi:10.1016/S1387-1811(01)00218-9
79. Ungureanu, A.; Trong-On, D.; Dumitriu, E.; Kaliaguine, S. *Appl. Catal., A* **2003,** *254,* 203–223. doi:10.1016/S0926-860X(03)00484-8
80. Meynen, V.; Beyers, E.; Cool, P.; Vansant, E. F.; Mertens, M.; Weyten, H.; Lebedev, O. I.; Van Tendeloo, G. *Chem. Commun.* **2004,** 898–899. doi:10.1039/b400636d
81. Meynen, V.; Cool, P.; Vansant, E. F.; Kortunov, P.; Grinberg, F.; Kärger, J.; Mertens, M.; Lebedev, O. I.; Van Tendeloo, G. *Microporous Mesoporous Mater.* **2007,** *99,* 14–22. doi:10.1016/j.micromeso.2006.08.029
82. Trong-On, D.; Ungureanu, A.; Kaliaguine, S. *Phys. Chem. Chem. Phys.* **2003,** *5,* 3534–3538. doi:10.1039/b304834a
83. Chiesa, M.; Meynen, V.; Van Doorslaer, S.; Cool, P.; Vansant, E. F. *J. Am. Chem. Soc.* **2006,** *128,* 8955–8963. doi:10.1021/ja061630p
84. Mazaj, M.; Stevens, W. J. J.; Logar, N. Z.; Ristic, A.; Tusar, N. N.; Arcon, I.; Daneu, N.; Meynen, V.; Cool, P.; Vansant, E. F.; Kaucic, V. *Microporous Mesoporous Mater.* **2009,** *117,* 458–465. doi:10.1016/j.micromeso.2008.07.025
85. Vernimmen, J.; Guidotti, M.; Silvestre-Albero, J.; Jardim, E. O.; Mertens, M.; Lebedev, O. I.; Van Tendeloo, G.; Psaro, R.; Rodriguez-Reinoso, F.; Meynen, V.; Cool, P. *Langmuir* **2011,** *27,* 3618–3625. doi:10.1021/la104808v
86. Ravishankar, R.; Kirschhock, C. E. A.; Knops-Gerrits, P.-P.; Feijen, E. J. P.; Grobet, P. J.; Vanorpen, P.; De Schryver, F. C.; Miehe, G.; Fuess, H.; Schoeman, B. J.; Jacobs, P. A.; Martens, J. A. *J. Phys. Chem. B* **1999,** *103,* 4960–4964. doi:10.1021/jp990296z
87. Kragten, D. D.; Fedeyko, J. M.; Sawant, K. R.; Rimer, J. D.; Vlachos, D. G.; Lobo, R. F. *J. Phys. Chem. B* **2003,** *107,* 10006–10016. doi:10.1021/jp035110h
88. Erdem-Senatalar, A.; Thompson, R. W. *J. Colloid Interface Sci.* **2005,** *291,* 396–404. doi:10.1016/j.jcis.2005.05.002
89. Van Der Voort, P.; Ravikovitch, P. I.; de Jong, K. P.; Neimark, A. V.; Janssen, A. H.; Benjelloun, M.; Van Bavel, E.; Cool, P.; Weckhuysen, B. M.; Vansant, E. F. *Chem. Commun.* **2002,** 1010–1011. doi:10.1039/B201424F
90. Van Der Voort, P.; Ravikovitch, P. I.; de Jong, K. P.; Van Bavel, E.; Janssen, A. H.; Neimark, A. V.; Weckhuysen, B. M.; Vansant, E. F. *J. Phys. Chem. B* **2002,** *106,* 5873–5877. doi:10.1021/jp025642i
91. Zamani, S.; Chiesa, M.; Meynen, V.; Xiao, Y.; Prelot, B.; Zajac, J.; Verpoort, F.; Cool, P.; Van Doorslaer, S. *J. Phys. Chem. C* **2010,** *114,* 12966–12975. doi:10.1021/jp103794x
92. Corma, A.; Fornés, V.; Pergher, S.; Maesen, Th. L. M.; Buglass, J. G. *Nature* **1998,** *396,* 353–356. doi:10.1038/24592
93. Corma, A.; Fornés, V.; Guil, J. M.; Pergher, S.; Maesen, Th. L. M.; Buglass, J. G. *Microporous Mesoporous Mater.* **2000,** *38,* 301–309. doi:10.1016/S1387-1811(00)00149-9
94. Díaz, U.; Fornés, V.; Corma, A. *Microporous Mesoporous Mater.* **2006,** *90,* 73–80. doi:10.1016/j.micromeso.2005.09.025
95. Corma, A.; Díaz, U.; Fornés, V.; Jordá, J. L.; Domine, M.; Rey, F. *Chem. Commun.* **1999,** 779–780. doi:10.1039/a900763f
96. Madsen, C.; Jacobsen, C. J. H. *Chem. Commun.* **1999,** 673–674. doi:10.1039/a901228a
97. Jacobsen, C. J. H.; Madsen, C.; Houzvicka, J.; Schmidt, I.; Carlsson, A. *J. Am. Chem. Soc.* **2000,** *122,* 7116–7117. doi:10.1021/ja000744c
98. Li, H.; Sakamoto, Y.; Liu, Z.; Ohsuna, T.; Terasaki, O.; Thommes, M.; Che, S. *Microporous Mesoporous Mater.* **2007,** *106,* 174–179. doi:10.1016/j.micromeso.2007.02.054
99. Egeblad, K.; Kustova, M.; Klitgaard, S. K.; Zhu, K. K.; Christensen, C. H. *Microporous Mesoporous Mater.* **2007,** *101,* 214–223. doi:10.1016/j.micromeso.2006.11.001
100. Schmidt, I.; Krogh, A.; Wienberg, K.; Carlsson, A.; Brorson, M.; Jacobsen, C. J. H. *Chem. Commun.* **2000,** 2157–2158. doi:10.1039/b006460m
101. Ok, D.-Y.; Jiang, N.; Prasetyanto, E. A.; Jin, H.; Park, S.-E. *Microporous Mesoporous Mater.* **2011,** *141,* 2–7. doi:10.1016/j.micromeso.2010.12.031
102. Sakthivel, A.; Huang, S.-J.; Chen, W.-H.; Lan, Z.-H.; Chen, K.-H.; Kim, T.-W.; Ryoo, R.; Chiang, A. S. T.; Liu, S.-B. *Chem. Mater.* **2004,** *16,* 3168–3175. doi:10.1021/cm035293k
103. Fang, Y.; Hu, H. *Catal. Commun.* **2007,** *8,* 817–820. doi:10.1016/j.catcom.2006.09.018
104. Tang, K.; Wang, Y. G.; Song, L. J.; Duan, L. H.; Zhang, X. T.; Sun, Z. L. *Mater. Lett.* **2006,** *60,* 2158–2160. doi:10.1016/j.matlet.2005.12.088
105. Janssen, A. H.; Schmidt, I.; Jacobsen, C. J. H.; Koster, A. J.; de Jong, K. P. *Microporous Mesoporous Mater.* **2003,** *65,* 59–75. doi:10.1016/j.micromeso.2003.07.003
106. Kruk, M.; Jaroniec, M.; Ryoo, R.; Joo, S. H. *J. Phys. Chem. B* **2000,** *33,* 7960–7968. doi:10.1021/jp000861u
107. Shin, H. J.; Ryoo, R.; Kruk, M.; Jaroniec, M. *Chem. Commun.* **2001,** 349–350. doi:10.1039/b009762o
108. Che, S. N.; Lund, K.; Tatsumi, T.; Iijima, S.; Joo, S. H.; Ryoo, R.; Terasaki, O. *Angew. Chem., Int. Ed.* **2003,** *42,* 2182–2185. doi:10.1002/anie.200250726
109. Tao, Y.; Tanaka, H.; Ohkubo, T.; Kanoh, H.; Kaneko, K. *Adsorpt. Sci. Technol.* **2003,** *21,* 199–203. doi:10.1260/026361703769013925
110. Tao, Y.; Hattori, Y.; Matumoto, A.; Kanoh, H.; Kaneko, K. *J. Phys. Chem. B* **2005,** *109,* 194–199. doi:10.1021/jp0464167
111. Fang, Y. M.; Hu, H. Q.; Chen, G. H. *Microporous Mesoporous Mater.* **2008,** *113,* 481–489. doi:10.1016/j.micromeso.2007.12.006
112. Yao, J. F.; Huang, Y.; Wang, H. T. *J. Mater. Chem.* **2010,** *20,* 9827–9831. doi:10.1039/c0jm01003k
113. Holland, B. T.; Abrams, L.; Stein, A. *J. Am. Chem. Soc.* **1999,** *121,* 4308–4309. doi:10.1021/ja990425p
114. Rhodes, K. H.; Davis, S. A.; Caruso, F.; Zhang, B. J.; Mann, S. *Chem. Mater.* **2000,** *12,* 2832–2834. doi:10.1021/cm000438y
115. Tosheva, L.; Mihailova, B.; Valtchev, V.; Sterte, J. *Microporous Mesoporous Mater.* **2000,** *39,* 91–101. doi:10.1016/S1387-1811(00)00179-7

116. Zhang, B. J.; Davis, S. A.; Mann, S. *Chem. Mater.* **2002,** *14,* 1369–1375. doi:10.1021/cm011251p
117. Zhang, B. J.; Davis, S. A.; Mendelson, N. H.; Mann, S. *Chem. Commun.* **2000,** 781–782. doi:10.1039/b001528h
118. Dong, A.; Wang, Y.; Tang, Y.; Ren, N.; Zhang, Y.; Yue, Y.; Gao, Z. *Adv. Mater.* **2002,** *14,* 926–929. doi:10.1002/1521-4095(20020618)14:12<926::AID-ADMA926>3.0.CO;2-1
119. Valtchev, V.; Smaihi, M.; Faust, A.-C.; Vidal, L. *Chem. Mater.* **2004,** *16,* 1350–1355. doi:10.1021/cm035100t
120. Ke, X.; Xu, L.; Zeng, C.; Zhang, L.; Xu, N. *Microporous Mesoporous Mater.* **2007,** *106,* 68–75. doi:10.1016/j.micromeso.2007.02.034
121. Karlsson, A.; Stöcker, M.; Schmidt, R. *Microporous Mesoporous Mater.* **1999,** *27,* 181–192. doi:10.1016/S1387-1811(98)00252-2
122. Solberg, S. M.; Kumar, D.; Landry, C. C. *J. Phys. Chem. B* **2005,** *109,* 24331–24337. doi:10.1021/jp054187y
123. Petkov, A.; Hölzl, M.; Metzger, T. H.; Mintova, S.; Bein, T. *J. Phys. Chem. B* **2005,** *109,* 4485–4491. doi:10.1021/jp0444969
124. Han, Y.; Meng, X.; Guan, H.; Yu, Y.; Zhao, L.; Xu, X.; Yang, X.; Wu, S.; Li, N.; Xiao, F.-S. *Microporous Mesoporous Mater.* **2003,** *57,* 191–198. doi:10.1016/S1387-1811(02)00590-5
125. Bagshaw, S. A.; Baxter, N. I.; Brew, D. R. M.; Hosie, C. F.; Yuntong, N.; Jaenicke, S.; Khuan, C. G. *J. Mater. Chem.* **2006,** *16,* 2235–2244. doi:10.1039/b602255c
126. Liu, Y.; Pinnavaia, T. J. *J. Mater. Chem.* **2004,** *14,* 1099–1103. doi:10.1039/b315193j
127. Liu, J.; Zhang, X.; Han, Y.; Xiao, F.-S. *Chem. Mater.* **2002,** *14,* 2536–2540. doi:10.1021/cm0103951
128. Yang, X.; Han, Y.; Lin, K.; Tian, G.; Feng, Y.; Meng, X.; Di, Y.; Du, Y.; Zhang, Y.; Xiao, F.-S. *Chem. Commun.* **2004,** 2612–2613. doi:10.1039/b410305j
129. Han, Y.; Li, N.; Zhao, L.; Li, D.; Xu, X.; Wu, S.; Di, Y.; Li, C.; Zou, Y.; Yu, Y.; Xiao, F.-S. *J. Phys. Chem. B* **2003,** *107,* 7551–7556. doi:10.1021/jp026899j
130. Meng, X.; Fan, W.; Kubota, Y.; Tatsumi, T. *J. Catal.* **2006,** *244,* 192–198. doi:10.1016/j.jcat.2006.09.007
131. Mrak, M.; Tusar, N. N.; Logar, N. Z.; Mali, G.; Kljajic, A.; Arcon, I.; Launay, F.; Gedeon, A.; Kaucic, V. *Microporous Mesoporous Mater.* **2006,** *95,* 76–85. doi:10.1016/j.micromeso.2006.05.002
132. Jin, C.; Li, G.; Wang, X.; Wang, Y.; Zhao, L.; Sun, D. *Microporous Mesoporous Mater.* **2008,** *111,* 236–242. doi:10.1016/j.micromeso.2007.07.037
133. Eimer, G. A.; Diaz, I.; Sastre, E.; Casuscelli, S. G.; Crivello, M. E.; Herrero, E. R.; Pérez-Pariente, J. *Appl. Catal., A* **2008,** *343,* 77–86. doi:10.1016/j.apcata.2008.03.028
134. Kremer, S. P. B.; Kirschhock, C. E. A.; Tielen, M.; Collignon, F.; Grobet, P. J.; Jacobs, P. A.; Martens, J. A. *Adv. Funct. Mater.* **2002,** *12,* 286–292. doi:10.1002/1616-3028(20020418)12:4<286::AID-ADFM286>3.0.CO;2-M
135. Kirschhock, C. E. A.; Kremer, S. P. B.; Vermant, J.; Van Tendeloo, G.; Jacobs, P. A.; Martens, J. A. *Chem.–Eur. J.* **2005,** *11,* 4306–4313. doi:10.1002/chem.200401329
136. Vernimmen, J.; Meynen, V.; Herregods, S. J. F.; Mertens, M.; Lebedev, O. I.; Van Tendeloo, G.; Cool, P. *Eur. J. Inorg. Chem.* **2011,** 4234–4240. doi:10.1002/ejic.201100268
137. Vernimmen, J.; Meynen, V.; Mertens, M.; Lebedev, O. I.; Van Tendeloo, G.; Cool, P. *J. Porous Mater.*, in press. doi:10.1007/s10934-011-9470-0
138. Srivastava, R.; Choi, M.; Ryoo, R. *Chem. Commun.* **2006,** 4489–4491. doi:10.1039/b612116k
139. Choi, M.; Cho, H. S.; Srivastava, R.; Venkatesan, C.; Choi, D.-H.; Ryoo, R. *Nat. Mater.* **2006,** *5,* 718–723. doi:10.1038/nmat1705
140. Shetti, V. N.; Kim, J.; Srivastava, R.; Choi, M.; Ryoo, R. *J. Catal.* **2008,** *254,* 296–303. doi:10.1016/j.jcat.2008.01.006
141. Wang, H.; Pinnavaia, T. J. *Angew. Chem., Int. Ed.* **2006,** *45,* 7603–7606. doi:10.1002/anie.200602595
142. Mukti, R. R.; Hirahara, H.; Sugawara, A.; Shimojima, A.; Okubo, T. *Langmuir* **2010,** *26,* 2731–2735. doi:10.1021/la902764s
143. Choi, M.; Na, K.; Kim, J.; Sakamoto, Y.; Terasaki, O.; Ryoo, R. *Nature* **2009,** *461,* 246–249. doi:10.1038/nature08288
144. Na, K.; Park, W.; Seo, Y.; Ryoo, R. *Chem. Mater.* **2011,** *23,* 1273–1279. doi:10.1021/cm103245m
145. Na, K.; Choi, M.; Park, W.; Sakamoto, Y.; Terasaki, O.; Ryoo, R. *J. Am. Chem. Soc.* **2010,** *132,* 4169–4177. doi:10.1021/ja908382n
146. Na, K.; Jo, C.; Kim, J.; Cho, K.; Jung, J.; Seo, Y.; Messinger, R. J.; Chmelka, B. F.; Ryoo, R. *Science* **2011,** *333,* 328–332. doi:10.1126/science.1204452
147. Stevens, W. J. J.; Meynen, V.; Bruijn, E.; Lebedev, O. I.; Van Tendeloo, G.; Cool, P.; Vansant, E. F. *Microporous Mesoporous Mater.* **2008,** *110,* 77–85. doi:10.1016/j.micromeso.2007.09.007
148. Van Oers, C. J.; Stevens, W. J. J.; Bruijn, E.; Mertens, M.; Lebedev, O. I.; Van Tendeloo, G.; Meynen, V.; Cool, P. *Microporous Mesoporous Mater.* **2009,** *120,* 29–34. doi:10.1016/j.micromeso.2008.08.056
149. Wang, J.; Groen, J. C.; Yue, W.; Zhou, W.; Coppens, M.-O. *Chem. Commun.* **2007,** 4653–4655. doi:10.1039/b708822a
150. Wang, J.; Groen, J. C.; Yue, W.; Zhou, W.; Coppens, M.-O. *J. Mater. Chem.* **2008,** *18,* 468–474. doi:10.1039/b711847c
151. Wang, J.; Groen, J. C.; Coppens, M.-O. *J. Phys. Chem. C* **2008,** *112,* 19336–19345. doi:10.1021/jp805276j
152. Wang, J.; Xue, W.; Zhou, W.; Coppens, M.-O. *Microporous Mesoporous Mater.* **2009,** *120,* 19–28. doi:10.1016/j.micromeso.2008.08.060
153. Yang, X.-Y.; Li, Y.; Lemaire, A.; Wei, Y-X.; Liu, Z.-M.; Van Tendeloo, G.; Su B-L. Hierarchically Micro-Meso-Macro Porous Aluminosilicates with Strong Acidity and Highly Catalytic activity Constructed from Zeolites Nanocrystals. Oral presentation at *IZC-IMMS 2010 conference*, Sorrento, Italy, July 4–9, 2010.
154. Yang, X.-Y.; Léonard, A.; Lemaire, A.; Tian, G.; Su, B.-L. *Chem. Commun.* **2011,** *47,* 2763–2786. doi:10.1039/c0cc03734f
155. Brinker, C. F.; Scherer, G. W. *Sol–Gel Science. The Physics and Chemistry of Sol–Gel Processing;* Academic Press Inc.: London, 1990.
156. Yuan, Z.-Y.; Su, B.-L. *J. Mater. Chem.* **2006,** *16,* 663–677. doi:10.1039/b512304f
157. Ratnasamy, P.; Srinivas, S. *Catal. Today* **2009,** *141,* 3–11. doi:10.1016/j.cattod.2008.03.009
158. Sheldon, R. A.; Arends, I. W. C. E.; Lempers, H. E. B. *Catal. Today* **1998,** *41,* 387–407. doi:10.1016/S0920-5861(98)00027-3
159. Guidotti, M.; Ravasio, N.; Psaro, R.; Gianotti, E.; Coluccia, S.; Marchese, L. *J. Mol. Catal. A: Chem.* **2006,** *250,* 218–225. doi:10.1016/j.molcata.2006.01.032

160. Yang, G.; Lan, X.; Zhuang, J.; Ma, D.; Zhou, L.; Liu, X.; Han, X.; Bao, X. *Appl. Catal., A* **2008,** *337,* 58–65. doi:10.1016/j.apcata.2007.11.037
161. Wold, A. *Chem. Mater.* **1993,** *5,* 280–283. doi:10.1021/cm00027a008
162. Li, Y. G.; Lee, Y. M.; Porter, J. F. *J. Mater. Sci.* **2002,** *37,* 1959–1965. doi:10.1023/A:1015234812360
163. Perego, C.; Carati, A.; Ingallina, P.; Mantegazza, M. A.; Bellussi, G. *Appl. Catal., A* **2001,** *221,* 63–72. doi:10.1016/S0926-860X(01)00797-9
164. Wang, Y.; Lin, M.; Tuel, A. *Microporous Mesoporous Mater.* **2007,** *102,* 80–85. doi:10.1016/j.micromeso.2006.12.019
165. Soult, A. S.; Pooré, D. D.; Mayo, E. I.; Stiegman, A. E. *J. Phys. Chem. B* **2001,** *105,* 2687–2693. doi:10.1021/jp002645r
166. Hasegawa, Y.; Ayame, A. *Catal. Today* **2001,** *71,* 177–187. doi:10.1016/S0920-5861(01)00428-X
167. Bonino, F.; Damin, A.; Ricchiardi, G.; Ricci, M.; Spanò, G.; D'Aloisio, R.; Zecchina, A.; Lamberti, C.; Prestipino, C.; Bordiga, S. *J. Phys. Chem. B* **2004,** *108,* 3573–3583. doi:10.1021/jp036166e
168. Thomas, J. M.; Sankar, G. *J. Synchrotron Radiat.* **2001,** *8,* 55–60. doi:10.1107/S090904950001935X
169. Shi, C.; Zhu, B.; Min, M.; Long, J. *Eur. J. Inorg. Chem.* **2009,** 4433–4440. doi:10.1002/ejic.200900508
170. Bordiga, S.; Damin, A.; Bonino, F.; Ricchiardi, G.; Zecchina, A.; Tagliapietra, R.; Lamberti, C. *Phys. Chem. Chem. Phys.* **2003,** *5,* 4390–4393. doi:10.1039/b306041c
171. Chaudhari, K.; Bal, R.; Srinivas, D.; Chandwadkar, A. J.; Sivasanker, S. *Microporous Mesoporous Mater.* **2001,** *50,* 209–218. doi:10.1016/S1387-1811(01)00454-1
172. Kholdeeva, O. A.; Trukhan, N. N. *Russ. Chem. Rev.* **2006,** *75,* 411–432. doi:10.1070/RC2006v075n05ABEH001210
173. Romano, U.; Esposito, A.; Maspero, F.; Neri, C.; Clerici, M. G. *Stud. Surf. Sci. Catal.* **1990,** *55,* 33–41. doi:10.1016/S0167-2991(08)60131-7
174. Liu, H.; Lu, G.; Guo, Y.; Guo, Y. *Appl. Catal., A* **2005,** *293,* 153–161. doi:10.1016/j.apcata.2005.07.021
175. Thangaraj, A.; Kumar, R.; Ratnasamy, P. *J. Catal.* **1991,** *131,* 294–297. doi:10.1016/0021-9517(91)90347-7
176. Kumar, R.; Mukherjee, P.; Bhaumik, A. *Catal. Today* **1999,** *49,* 185–191. doi:10.1016/S0920-5861(98)00423-4
177. Bhaumik, A. *Chem. Commun.* **1998,** 463–464. doi:10.1039/a708528a
178. Maspero, F.; Romano, U. *J. Catal.* **1994,** *146,* 474–482. doi:10.1006/jcat.1994.1085
179. Cundy, C. S.; Forrest, J. O. *Microporous Mesoporous Mater.* **2004,** *72,* 67–80. doi:10.1016/j.micromeso.2004.04.006
180. Tvaruzkova, Z.; Zilkova, N. *Appl. Catal., A* **1993,** *103,* L1–L4. doi:10.1016/0926-860X(93)85167-N
181. Clerici, M. G. Titanium Silicalite-1. In *Metal Oxide Catalysis;* Jackson, S. D.; Hargreaves, S. J., Eds.; Wiley-VCH: Weinheim, Germany, 2009; pp 705–754.
182. Cavani, F.; Teles, J. H. *ChemSusChem* **2009,** *2,* 508–534. doi:10.1002/cssc.200900020
183. Ratnasamy, P.; Srinivas, D.; Knözinger, H. *Adv. Catal.* **2004,** *48,* 1–169. doi:10.1016/S0360-0564(04)48001-8
184. De Vos, D. E.; Sels, B. F.; Jacobs, P. A. *Adv. Synth. Catal.* **2003,** *345,* 457–473. doi:10.1002/adsc.200390051
185. Chen, S.-Y.; Tang, C.-Y.; Yang, L.-Y.; Tatsumi, T.; Cheng, S. *J. Mater. Chem.* **2011,** *21,* 2255–2265. doi:10.1039/c0jm03111a
186. Gianotti, E.; Bisio, C.; Marchese, L.; Guidotti, M.; Ravasio, N.; Psaro, R.; Coluccia, S. *J. Phys. Chem. C* **2007,** *111,* 5083–5089. doi:10.1021/jp067506+
187. Fraile, J. M.; Garcia, J. I.; Mayoral, J. A.; Vispe, E. *Appl. Catal., A* **2003,** *245,* 363–376. doi:10.1016/S0926-860X(02)00643-9
188. Blasco, T.; Corma, A.; Navarro, M. T.; Pérez-Pariente, J. *J. Catal.* **1995,** *156,* 65–74. doi:10.1006/jcat.1995.1232
189. Guidotti, M.; Batonneau-Gener, I.; Gianotti, E.; Marchese, L.; Mignard, S.; Psaro, R.; Sgobba, M.; Ravasio, N. *Microporous Mesoporous Mater.* **2008,** *111,* 39–47. doi:10.1016/j.micromeso.2007.07.010

License and Terms

The definitive version of this article is the electronic one which can be found at:
doi:10.3762/bjnano.2.87

Beilstein Journal
of Nanotechnology

Mesoporous $MgTa_2O_6$ thin films with enhanced photocatalytic activity: On the interplay between crystallinity and mesostructure

Jin-Ming Wu[1], Igor Djerdj[2], Till von Graberg[3] and Bernd M. Smarsly*[3]

Full Research Paper

Open Access

Address:
[1]Department of Materials Science and Engineering, Zhejiang University, Hangzhou 310027, China, [2]Ruđer Bošković Institute, Bijenička 54, 10000 Zagreb, Croatia and [3]University of Giessen, Institute of Physical Chemistry, Heinrich-Buff-Ring 58, D-35392 Giessen, Germany

Email:
Bernd M. Smarsly* - bernd.smarsly@phys.chemie.uni-giessen.de

* Corresponding author

Keywords:
magnesium tantalate; mesoporous materials; photocatalytic activity; self-assembly; thin films

Beilstein J. Nanotechnol. **2012,** *3,* 123–133.
doi:10.3762/bjnano.3.13

Received: 10 September 2011
Accepted: 31 January 2012
Published: 13 February 2012

This article is part of the Thematic Series "Micro- and mesoporous solids: From science to application".

Guest Editor: J. J. Schneider

Abstract

Ordered mesoporous, crystalline $MgTa_2O_6$ thin films with a mesoscopic nanoarchitecture were synthesized by evaporation-induced self-assembly (EISA) in combination with a sol–gel procedure. Utilization of novel templates, namely the block copolymers KLE (poly(ethylene-*co*-butylene)-*b*-poly(ethylene oxide)) and PIB6000 ($CH_3C(CH_3)_2(CH_2C(CH_3)_2)_{107}CH_2C(CH_3)_2C_6H_4O$-$(CH_2CH_2O)_{100}H$), was the key to achieving a stable ordered mesoporous structure even upon crystallization of $MgTa_2O_6$ within the mesopore walls. The effect of the calcination temperature on the ability of the mesoporous films to assist the photodegradation of rhodamine B in water was studied. As a result, two maxima in the photocatalytic activity were identified in the calcination temperature range of 550–850 °C, peaking at 700 °C and 790 °C, and the origin of this was investigated by using temperature-dependent X-ray scattering. Optimal activity was obtained when the mesoporous film was heated to 790 °C; at this temperature, crystallinity was significantly high, with $MgTa_2O_6$ nanocrystals of 1.6 nm in size (averaged over all reflections), and an ordered mesoporous structure was maintained. When considering the turnover frequency of such photocatalysts, the optimized activity of the present nanoarchitectured $MgTa_2O_6$ thin film was ca. four times that of analogous anatase TiO_2 films with ordered mesopores. Our study demonstrated that high crystallinity and well-developed mesoporosity have to be achieved in order to optimize the physicochemical performance of mesoporous metal-oxide films.

Introduction

Because of its excellent microwave dielectric properties, $MgTa_2O_6$ is one of the ternary oxides that have been well studied for application as dielectric resonators operating at microwave frequencies [1-9]. In the form of thin films, it is also considered to be one of the most promising candidates for use in polarizers in optical communications and other optical devices [5]. The traditional ceramic method of synthesizing $MgTa_2O_6$, i.e., solid-state reaction, requires high temperatures of 1200–1400 °C, which produces coarse grains and an inhomogeneous composition [6-8]. Crystalline $MgTa_2O_6$ powders were fabricated at 850 °C by a molten-salt method and at 550 °C by a wet-chemical approach [9]. Thin films containing mainly $MgTa_2O_6$ and $Mg_4Ta_2O_9$ phases can be formed by reactions between MgO(001) substrates and Ta–O vapors, which are produced by electron-beam evaporation of a Ta_2O_5 powder target in a high-vacuum system, at temperatures of 700–1000 °C [5].

In 1998, Kato and Kudo reported that $MgTa_2O_6$ that had been synthesized by calcination of mixtures of Ta_2O_5 and $MgCO_3$ showed photocatalytic water-decomposition activity without cocatalysts [10]. Due to the inherent coarse-grain structure of $MgTa_2O_6$ powders fabricated by the solid-state reaction, their photocatalytic activity is quite low. With the help of a block polymer P123, a Mg–Ta oxide powder with highly ordered mesopores was previously synthesized [11]. After removal of the P123 template by washing in water, the wormholelike microporous $MgTa_2O_6$ powder, though amorphous, showed enhanced water-decomposition activity when compared to the crystalline $MgTa_2O_6$ prepared by a solid-state reaction. The high activity is ascribed to the thin walls (2.8 nm) separating the mesopores, as the excited electrons and holes only have to travel a short distance to the surface [11]. The use of photocatalysts in the form of thin films avoids the laborious recycling procedure, and this has promoted the development of high-efficiency $MgTa_2O_6$ thin films. One can expect enhanced photocatalytic activity from $MgTa_2O_6$ thin films with well-crystallized nanocrystallites and ordered mesopores, which guarantee the photocatalyst access to the target molecules and also possess a high specific surface area. Unfortunately, because of the high crystallization temperature and low decomposition temperature of most commercially available templates, the fabrication of ordered mesoporous $MgTa_2O_6$ thin films with crystallized walls remains a complex task, and hence detailed photocatalytic-activity studies of such films are scarce.

In particular, suitable well-defined mesoscopic, photocatalytically active metal oxides would be ideal materials for a case study to address the importance of high crystallinity coupled with a well-developed mesostructure. It has been often stated that the performance of mesoporous metal oxides requires both features to be optimized at the same time, but to the best of our knowledge no systematic study has been performed in the field of photocatalysis.

Various oxides with high crystallization temperatures have only recently been synthesized successfully in the form of highly ordered mesoporous thin films, thanks to novel templates such as poly(ethylene-*co*-butylene)-*b*-poly(ethylene oxide), “KLE” (Kraton Liquid -*block*-poly(ethylene oxide)). The KLE template is capable of forming relatively large mesopores and thick walls, and at the same time possesses a high decomposition temperature of up to 400 °C, which facilitates preservation of the ordered mesoporous structure during heating to a high crystallization temperature [12-14]. This work reports the synthesis and photocatalytic characterization of crystallized, mesoporous $MgTa_2O_6$ thin films, obtained through an evaporation-induced self-assembly (EISA) approach, with the help of the KLE template. The photocatalytic activity of the nanoarchitectured $MgTa_2O_6$ thin film was compared both to that achieved by using the BASF Pluronic F127 (*block* copolymer EO_{106}–PO_{70}–EO_{106}), which forms larger mesopores compared to most other commercially available templates, and to a previously reported type of anatase TiO_2 thin film with ordered mesopores, examples of which are widely used as photocatalysts [15,16]. Recently, a further class of block copolymers with advanced templating properties was introduced, namely poly(isobutylene)-*b*-poly(ethylene oxide) [14,17]. Here, we also used such a polymer, namely “PIB6000”, $CH_3C(CH_3)_2(CH_2C(CH_3)_2)_{107}CH_2C(CH_3)_2C_6H_4O(CH_2CH_2O)_{100}H$, see [17], as an additional structure-directing agent.

As a main motivation, our study addressed the influence of the heat-treatment temperature (i.e., crystallite size) on the photocatalytic activity. Thereby, the influence of the crystallite size and mesostructural organization on the photocatalytic activity was systematically investigated by using dye degradation as a qualitative measure.

Results and Discussion

Film characterization

In the following, we focus on mesoporous $MgTa_2O_6$ films templated by the KLE block copolymer. PIB6000 generates films with very similar mesopore structure and crystallinity, with only the average lateral size of the mesopores (ca. 20 nm) being larger than in the case of KLE template films (ca. 15 nm). Since the mesopore structure (spherical mesopores) and also photocatalytical activity of these films are very similar, in the following, mainly KLE-templated films are discussed. Additional results for PIB6000-templated mesoporous films are presented in Supporting Information File 1.

Both the mesoporous and the nonporous (nontemplated) films show distinct X-ray diffraction (XRD) reflections corresponding to a tri-rutile structure $MgTa_2O_6$ (JCPDS card 32-0631), only after calcination at temperatures beyond 760 °C, as illustrated in Figure 1. The crystallinity of $MgTa_2O_6$ in the KLE-templated mesoporous film increased with increasing

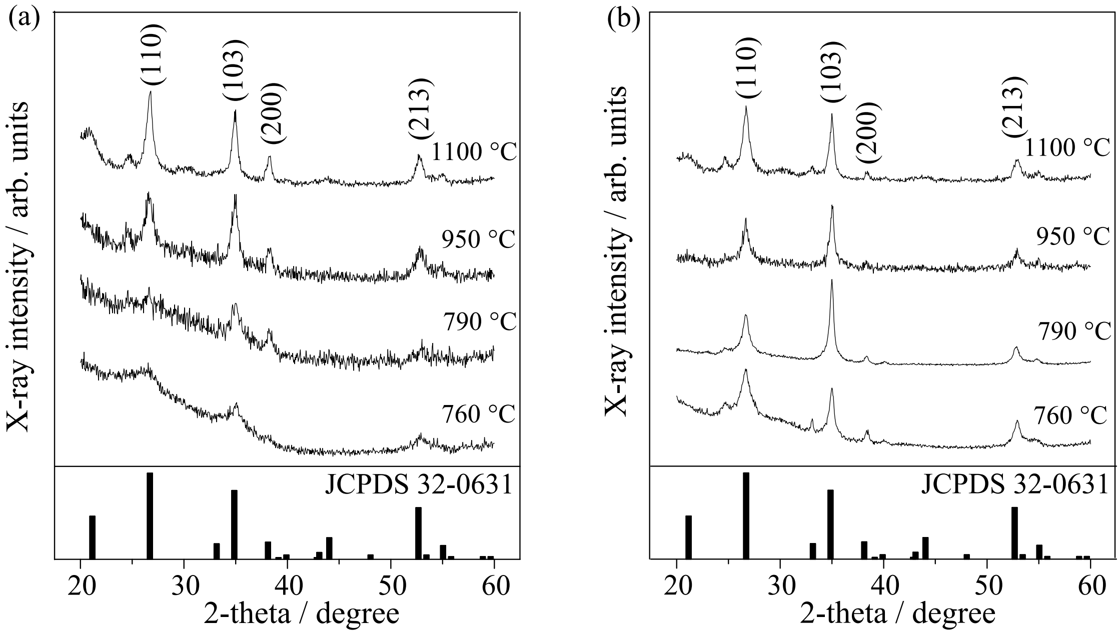

Figure 1: XRD patterns of (a) the KLE-templated mesoporous and (b) the nonporous $MgTa_2O_6$ thin film after thermal treatment at various temperatures.

calcination temperature from 760 up to 1100 °C. The average grain size, which was estimated by applying the Rietveld refinement, is shown in Figure 2 as a function of the calcination temperature for both mesoporous and nonporous films. Owing to the lower overall crystallinity of the investigated material and a high background in some of the analyzed XRD patterns, the microstrain part in the size-microstrain procedure within the Rietveld refinement was not refined and was kept to the instrumental values determined by the crystalline standard. The standard was also used for the deconvolution of the instrumental-broadening contribution. Since the initial refinement gave rather high disagreement between the experimental and calculated curves, particularly in the [103] direction, an anisotropic broadening with a larger crystallite size along the [103] direction was assumed. Accordingly, the difference curves were then smooth and all refinements were satisfactory. In Figure 2, vertical error bars represent the distribution interval of crystallite sizes for all reflections, and therefore the error interval is actually a measure of crystal anisotropy. It is obvious that the nonporous crystallites appear with a larger anisotropy (larger grains in [103] direction) compared to their mesoporous counterparts. When the calcination temperature was increased from 760 to 1100 °C the grain size of $MgTa_2O_6$ in the mesoporous film showed a gradual increase from 1.1 to 9.4 nm. When both films were heated to the same temperature of 760 and 790 °C, the crystallinity of $MgTa_2O_6$ in the nonporous film was more pronounced than in the mesoporous one, which can be attributed to the retarding effect of the template and the mesopores on the grain growth.

Grain growth of $MgTa_2O_6$ in the nontemplated film with increasing calcination temperature from 760 up to 1100 °C was

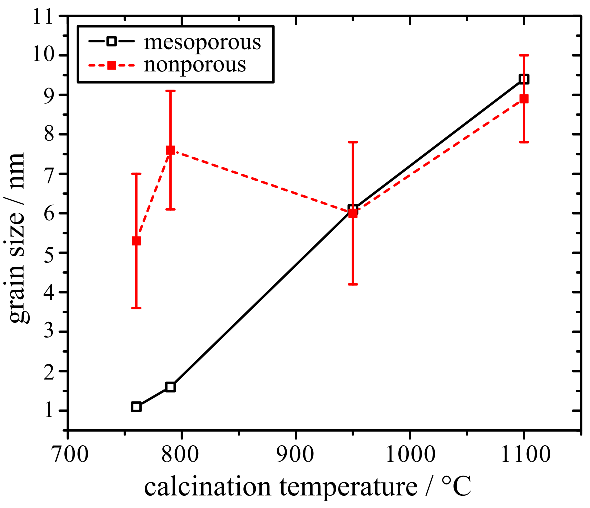

Figure 2: Average grain size and its standard deviation as a measure of anisotropy of $MgTa_2O_6$ in the mesoporous KLE-templated and nonporous films, as a function of the calcination temperature.

not so conspicuous. The grain size only increased from 5.3 to 8.9 nm.

Figure 3 shows the SEM surface morphology of the $MgTa_2O_6$ thin film subjected to various calcination temperatures. The EISA procedure achieved a crack-free surface with randomly distributed micrometer-sized round concaves, while the film as a whole consisted of highly ordered mesopores. The dual nanoarchitecture remained almost unchanged upon heating to 760 °C, with crystallized $MgTa_2O_6$ appearing within the walls. After being heated to the highest temperature available (1100 °C), conspicuous cracks appeared within the round concaves and the ordered mesopores decayed to a wormlike state. However, the microstructure was still preserved, and most thermally induced cracks were restricted to each concave, that is, they did not coalesce or propagate throughout the film upon heating to 1100 °C. At this temperature, well-crystallized $MgTa_2O_6$ walls were obtained, as seen by XRD.

Figure 4 illustrates the AFM surface morphology of the $MgTa_2O_6$ film after calcination at 760 °C, which is in agreement with the SEM observation. The corresponding height profile obtained from the AFM image suggests that the depth of the randomly distributed round concaves was ca. 60 nm. The film thickness was estimated to be ca. 200 nm; therefore, the ordered mesoporous $MgTa_2O_6$ film thoroughly covered the Si substrate. The distance between two neighboring mesopores remained constant at ca. 22 nm after calcination at 760 °C. The ordered mesoporous structure was further confirmed by the TEM morphology of flakes scratched off from the $MgTa_2O_6$ film before and after heating at 760 °C, as indicated in Figure 5. From such TEM images a spherical mesopore shape was inferred with an average mesopore diameter of ca. 15 nm. TEM images of PIB6000-templated films are shown in Supporting Information File 1 (Figure S6).

Figure 6 shows the SAXS patterns (measured in symmetric reflection with a 1-D detector) of the mesoporous $MgTa_2O_6$ film after calcination at various temperatures. The diffuse SAXS pattern does not allow for an unambiguous determination of the pore morphology. Taking into account previous studies on KLE as a template and the TEM images, the SAXS data can be interpreted in terms of spherical mesopores, although fcc, bcc and hcp structures cannot be distinguished. The scattering maxima are characteristic of ordered mesopores, being assigned as the (110) reflection of a distorted bcc mesoporous structure, and became diffuse as the calcination temperature increased to 760 °C, i.e., the onset of crystallization temperature. However, the SAXS scattering maxima can still be discerned after calcination up to 1000 °C. Therefore, the present ordered mesoporous $MgTa_2O_6$ film possessed a relatively high thermal stability. This property was attributed to the special templating properties of KLE, which forms relatively large micelles during the EISA procedure and hence helps to stabilize the ordered mesopores even after the template has been removed [15-19]. In addition, the randomly distributed round concaves also possibly aid the release of thermal stress, thus helping to maintain the ordered mesopores up to calcination temperatures as high as 1000 °C.

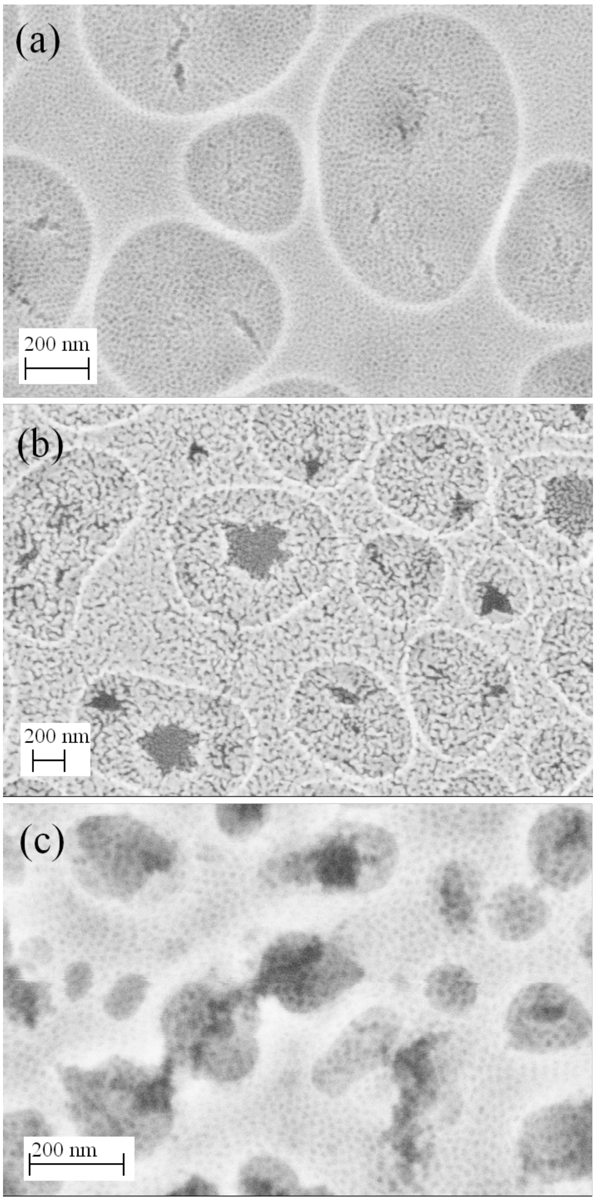

Figure 3: SEM surface morphologies of a mesoporous KLE-templated $MgTa_2O_6$ film after thermal treatment at (a) 760 °C and (b) 1100 °C, and (c) of a mesoporous PIB6000-templated $MgTa_2O_6$ film after thermal treatment at 760 °C.

2-D-SAXS patterns of the as-stabilized mesoporous $MgTa_2O_6$ film and of those heated to 550, 650 and 760 °C are shown in

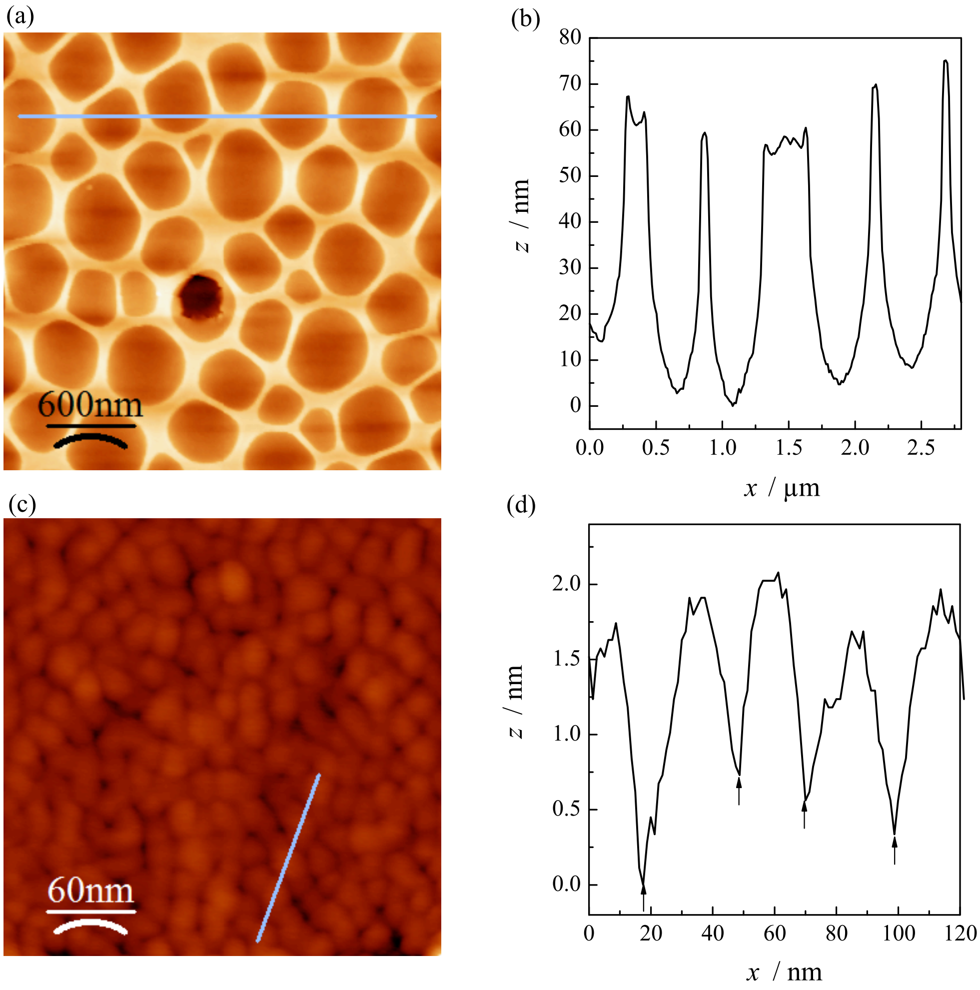

Figure 4: AFM (a, c) morphology of the KLE-templated mesoporous $MgTa_2O_6$ film after calcination at 760 °C. The corresponding profiles along the lines indicated in (a) and (c) are shown in (b) and (d), respectively.

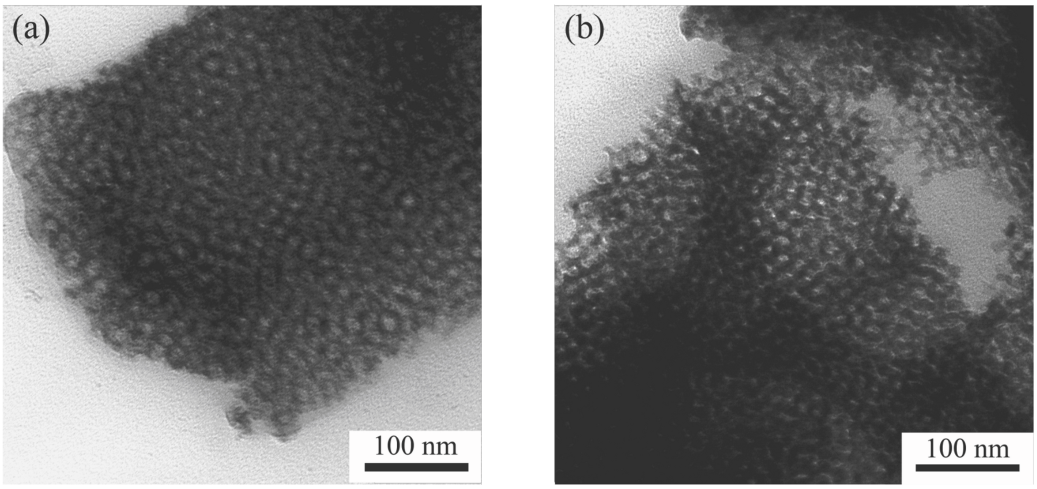

Figure 5: TEM morphology of a fragment scratched off from a mesoporous KLE-templated $MgTa_2O_6$ thin film before (a) and after calcination at 760 °C (b).

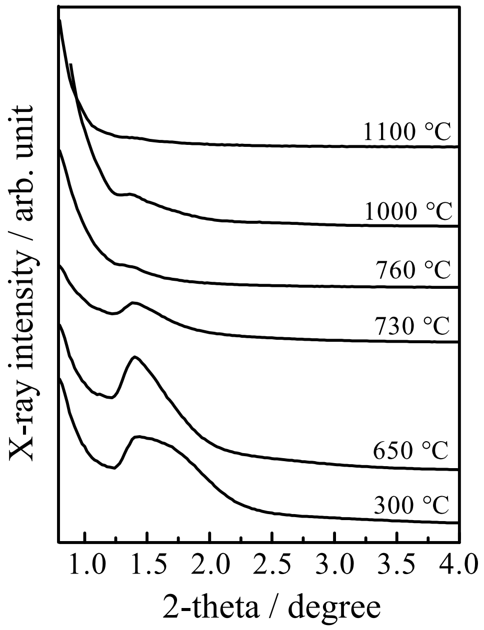

Figure 6: SAXS patterns (measured in symmetric reflection) of the mesoporous KLE-templated $MgTa_2O_6$ thin film after calcination at various temperatures.

Figure 7. Here, the material was synthesized on ultrathin Si wafers (thickness ca. 30 μm), allowing the penetration of the covered wafers by X-rays. The maxima attributable to a bcc mesostructure in [110] orientation relative to the substrate can be discerned in the 2-D patterns measured with an angle of incidence of β = 10°, even after the onset of crystallization [20]. In addition, the 2-D-SAXS patterns became increasingly ellipsoidal, suggesting an anisotropic shrinkage of the mesostructure in the direction normal to the substrate, which has often been observed previously [20]. For the SAXS patterns obtained in transmission geometry (β = 90°) the 1,−1,0 ring, corresponding to a random orientation of mesostructured domains of the bcc mesoporous structure within the plane parallel to the substrate, was observed for all the films. No in-plane contraction in the plane occurred even for a film heated to 760 °C, which is in agreement with the crack-free surface observed by SEM (Figure 3) and AFM (Figure 4). The in-plane *d*-spacing of 22 nm derived from the 2-D-SAXS patterns collected at β = 90° agreed well with the AFM measurement (Figure 4). 2-D-SAXS data of F127- and PIB6000-templated films are shown in Supporting Information File 1 (Figure S5).

The EISA procedure has been widely utilized to synthesize thin films with ordered mesopores, with the help of certain surfactants; however, such round concaves containing ordered mesopores have not been noticed before. As a preliminary result, we ascribe the formation of such a nanoarchitecture to the Mg^{2+} ions in the precursor, which increased the polarity of the ethanol and enhanced the evaporation speed of the solvent. The rapid evaporation produced randomly distributed bubbles, and when these collapsed they left randomly distributed, open, round concaves.

The mesoporosity was additionally investigated by nitrogen physisorption at 77 K (see Supporting Information File 1). Since the amount of material is by far too small for a single film, as an example, four films of PIB6000-templated $MgTa_2O_6$ were deposited on top of each other in order to provide a suffi-

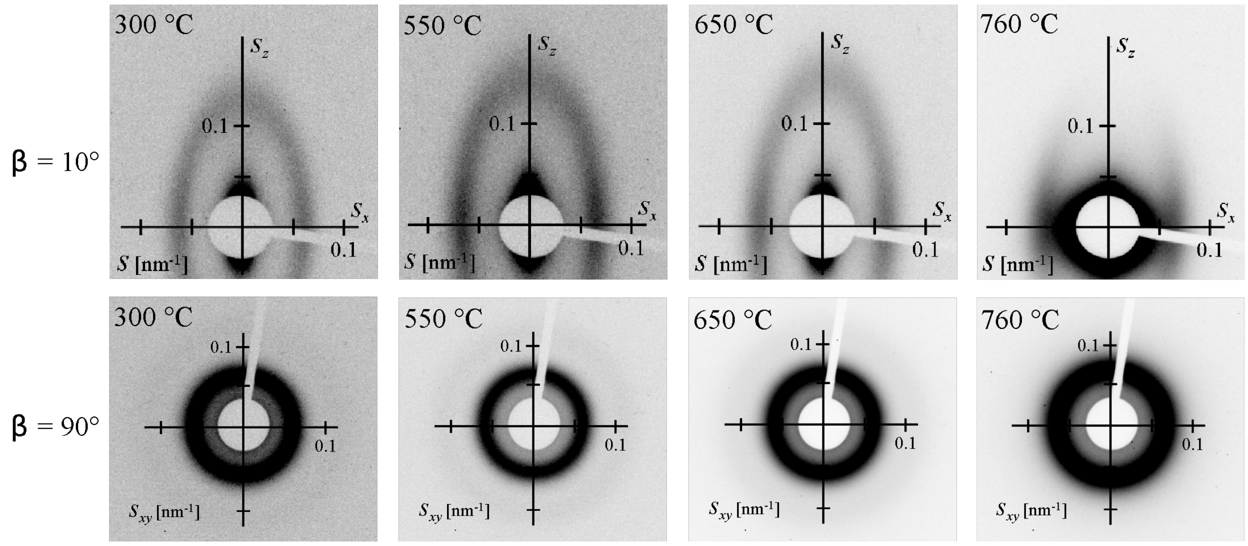

Figure 7: 2-D-SAXS patterns of the KLE-templated mesoporous $MgTa_2O_6$ thin film after calcination at various temperatures. The values β = 10° and β = 90° indicate the angles of incidence between the surface of the film and the X-ray beam.

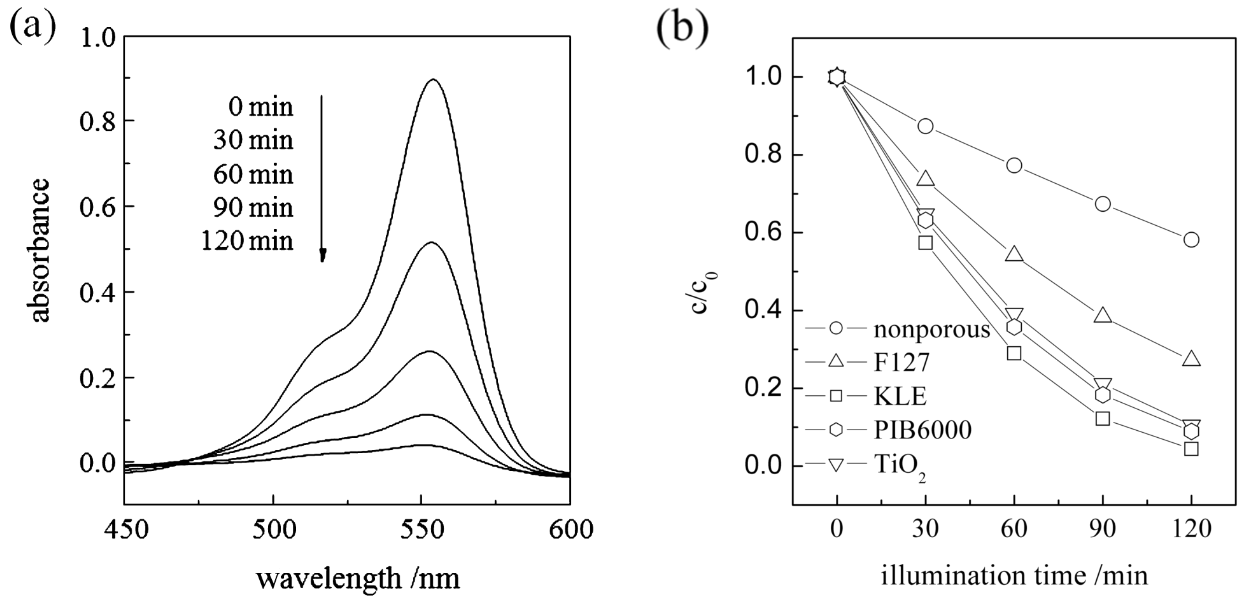

Figure 8: (a) Absorption spectra of RhB after photodegradation for given durations, assisted by the mesoporous KLE-templated $MgTa_2O_6$ thin film after calcination at 790 °C. (b) The RhB concentration as a function of the photodegradation time, assisted by the mesoporous anatase TiO_2 thin film ("TiO_2") after calcination at 550 °C, the KLE-, PIB6000- and F127-templated mesoporous $MgTa_2O_6$ thin film after calcination at 790 °C, as well as the nonporous $MgTa_2O_6$ thin film.

ciently large absolute surface area. These multilayer films were studied by SAXS and SEM to ensure that indeed the multilayer deposition did not disturb the mesostructure. For comparison, multilayers of nontemplated films were studied by nitrogen physisorption.

For such a PIB6000-templated mesoporous multilayer $MgTa_2O_6$ film with four single layers a BET surface area of ca. 260 m^2 cm^{-3} was observed (after heat treatment at 790 °C), which is typical of mesoporous films with such large mesopores. While the quality of the isotherm is limited, owing to the low amount of material, an average mesopore size of ca. 12 nm can be formally deduced from the BJH approach applied to the adsorption branch. Such a value has to be regarded with care, but nevertheless is consistent with the suggestion of the spherical mesopores being substantially contracted perpendicular to the surface. Thus, nitrogen physisorption provides a well-defined accessible mesopore structure up to high temperatures. A nontemplated film did not exhibit substantial uptake of nitrogen, and no reasonable isotherm was obtained.

Photocatalytic activity evaluation

In the absence of the oxide film, the UV irradiation induced no remarkable degradation of rhodamine B (RhB) in water. When the $MgTa_2O_6$ film was exposed to radiation, RhB underwent gradual decomposition depending on the irradiation time. As an example, Figure 8a shows the absorption curve of the aqueous RhB solution as a function of the UV irradiation time in the presence of the KLE-templated $MgTa_2O_6$ film after calcination at 790 °C. The change in RhB concentration as a function of the irradiation time, in the presence of various oxide films, is illustrated in Figure 8b. Here, two oxide films, namely, a mesoporous anatase film and a F127-templated $MgTa_2O_6$ film, were included as references. The fabrication and characterization of the mesoporous anatase film is reported elsewhere [21]. F127-templated $MgTa_2O_6$ films also exhibited an ordered mesoporous structure with concaves, even after calcination at 760 °C; however, the pore-to-pore distance was much smaller and the mesopores were less ordered compared to those templated by KLE. In addition, the round concaves were much smaller and distributed less homogeneously. After calcination, the F127-templated $MgTa_2O_6$ film exhibited XRD patterns corresponding to tri-rutile structure $MgTa_2O_6$ (see Figure S1 for the 2-D-SAXS patterns, Figure S2 for the SEM morphology, and Figure S3 for the XRD pattern in Supporting Information File 1). From Figure 8b it can be seen that, of all the various oxide films, the KLE derived mesoporous $MgTa_2O_6$ film possessed the highest activity in assisting the photodegradation of RhB in water.

Interestingly, PIB6000-templated mesoporous $MgTa_2O_6$ thin film showed a very similar dye-degradation activity as compared with the KLE-templated films.

Photocatalytic degradation of RhB in water roughly follows a pseudo-first-order reaction [22-24],

$$\ln \frac{c_0}{c} = kt \qquad (1)$$

where c/c_0 is the normalized RhB concentration, t is the illumination time, and k is the apparent reaction rate in terms of min^{-1}. All of the data demonstrated good linearity for all the curves based on Equation 1 (Figure not shown). The derived reaction rate constant is listed in Table 1. Also included in Table 1 is the so-called turnover frequency (TOF), which defines the ratio of the reaction rate constant to the catalyst content and reflects the intrinsic activity per site of catalysis [25]. The catalyst content in the mesoporous film was calculated assuming a condensed film with a porosity of ca. 30% and a thickness of 200 nm (the densities of $MgTa_2O_6$ [1] and anatase TiO_2 [24] are 7.2 g cm^{-3} and 3.8 g cm^{-3}, respectively), which would overestimate the catalyst content and hence underestimate the TOF value for the mesoporous films. A detailed description of the result in Table 1 will be presented later.

Figure 9 shows the reaction rate constants of the mesoporous and nonporous $MgTa_2O_6$ films as a function of the calcination temperature. The photocatalytic activity of the nonporous film reached an optimum value of ca. 0.0175 min^{-1} after being heated to 950 °C. However, the evolution in photocatalytic activity for the mesoporous $MgTa_2O_6$ film with increasing calcination temperatures was considerably more complicated. Between 550 °C and 760 °C the photocatalytic activity initially increased to a maximum of 0.0216 min^{-1} at 700 °C, but then decreased as the calcination temperature rose to 760 °C. Interestingly, the photocatalytic activity increased again to a maximum of 0.0260 min^{-1} when the calcination temperature rose from 760 °C to 790 °C. There was a dramatic drop in photocatalytic activity as the temperature increased to 850 °C followed by a gradual increase as the temperature rose to 1100 °C.

Since this peculiar increase and decrease in the activity is one of the most relevant findings of the present study, the measurements were repeated three times. As the results were similar to PIB6000-templated films, Figure 9 shows only one of the films for KLE-templated $MgTa_2O_6$.

Under UV illumination, $MgTa_2O_6$ adsorbs photons with a wavelength shorter than ca. 278 nm and generates electron–hole pairs corresponding to its bandgap of ca. 4.4 eV [10] (see Figure S4, Supporting Information File 1, for the UV–vis diffuse-reflectance spectrum). The photogenerated holes diffuse all the way to the surface where they oxidize the preadsorbed RhB molecules directly, or indirectly by forming hydroxyl radicals, which abstract H atoms from the organics on or near the semiconductor surface [26]. During subsequent calcination, three factors readily affecting the photocatalytic activity

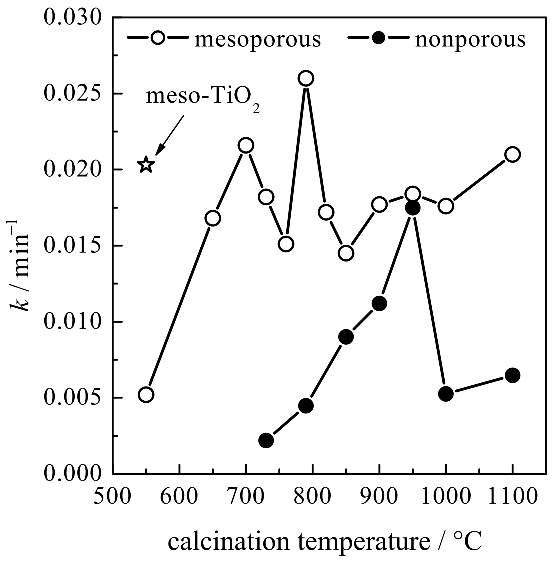

Figure 9: Reaction rate constants of the photodegradation reaction in the presence of the KLE-templated mesoporous and nonporous $MgTa_2O_6$ thin films after thermal treatment at various temperatures. The value for a mesoporous TiO_2 thin film is represented by a star in the figure for reference.

Table 1: Reaction rate constant (k) and turnover frequency (TOF) of selected photocatalysts.

photocatalyst	m (catalyst content) / mmol	k / min^{-1}	TOF (k/m) / $(\text{mmol·min})^{-1}$
nonporous $MgTa_2O_6$ film (790 °C)	0.00490	0.00448	0.914
nonporous $MgTa_2O_6$ film (950 °C)	0.00490	0.0175	3.57
KLE-derived $MgTa_2O_6$ film (790 °C)	0.00490	0.0260	5.30
F127-derived $MgTa_2O_6$ film (790 °C)	0.00490	0.0109	2.22
PIB-derived $MgTa_2O_6$ film (790 °C)	0.00490	0.0202	4.12
mesoporous TiO_2 film (550 °C)	0.0152	0.0203	1.34

changed dramatically in the current investigation, i.e., crystallinity, grain size, and ordered mesopores [27,28]. Defects serve as traps for photogenerated electron–hole pairs [26]; therefore, improved crystallinity prolongs the lifetime of the photogenerated pairs, thus increasing the number of holes that are able to diffuse all the way to the surface to be involved in the photodegradation reaction. Small grains are assumed to facilitate the photocatalytic reaction, as it takes less time for the photogenerated pairs of holes and electrons to migrate all the way to the surface to be involved in the reaction, which thus inhibits the recombination of the pairs [27,28]. Ordered mesopores being accessible from the top favors the diffusion of organic molecules to the oxide surface and at the same time significantly increases the number of catalytically active sites [15]. In a word, improved crystallinity and small grain size of oxides, together with well-ordered mesopores contribute to the photocatalytic activity of semiconductor oxide films with ordered mesoporous structures.

Increasing the calcination temperatures promotes crystallinity, but at the same time causes grain growth and deterioration of the ordered mesoporous structure; consequently, choosing the calcination temperature is always a balancing act. Considering that 760 °C is the onset of crystallization for the present $MgTa_2O_6$ (Figure 1), the fact that the first maximum appeared at 700 °C in the temperature range of 550–760 °C for the mesoporous $MgTa_2O_6$ film can be attributed to the balancing act between the crystallinity and the ordered mesopores. When heated to a temperature tens of degrees below the onset of crystallization, e.g., 700 °C, the decay in the ordered mesopores was not so significant, as can be discerned from the SAXS results shown in Figure 6 and Figure 7. Therefore, the enhanced crystallinity obtained by increasing calcination temperature produced a near linear improvement in the photocatalytic activity at 700 °C. As the calcination temperature approached that of the onset of crystallization, decay in the ordered mesoporous structure became significant due to the further mechanical stress accompanying the amorphous–crystalline phase transformation [29]. There was a decline in photocatalytic activity at the point where the advantages of the increasing crystallinity were outweighed by the disadvantage introduced by the deterioration of the ordered mesopores.

After the onset of crystallization, the negative effect caused by the collapsed mesoporous structure stabilized. In this case, one should expect the gradually increasing crystallinity to produce a gradual increase in photocatalytic activity as calcination temperatures rise. However, the other factor readily affecting the photocatalytic activity of a crystallized oxide, i.e., the grain size, should not be neglected. After the onset of crystallization, the grain size of $MgTa_2O_6$ increased steadily with increasing calcination temperature from 760 °C to 950 °C, as indicated in Figure 2. The negative effect caused by larger grains, in combination with the positive effect originating from the improved crystallinity, resulted in the second maximum of photocatalytic activity at 790 °C in the temperature range of 760–850 °C. The gradual increase in photocatalytic activity of the films after calcination beyond 850 °C can be ascribed to a consistently improved crystallinity and also to the fact that the changes in the grain size and mesopores were not overly significant.

The positive impact of the ordered mesoporous structure on the photocatalytic activity is reinforced by the significantly higher photocatalytic performance of the mesoporous $MgTa_2O_6$ film compared to the nonporous one (Figure 9). In addition, the KLE-templated mesoporous $MgTa_2O_6$ film exhibited higher photocatalytic activity than the F127-templated counterpart at the optimized calcination temperature of 790 °C. In the current investigation, a $MgTa_2O_6$ film with an ordered mesoporous structure was also successfully synthesized by using the commercial F127 template even after calcination at 760 °C; however, the mesopores were much smaller and less ordered. It is not possible to synthesize ordered mesoporous $MgTa_2O_6$ films with crystallized walls by using the other widely used block polymer of P123, because of the even smaller mesopores formed during the EISA procedure [11]. Therefore, the present KLE template contributes greatly to the $MgTa_2O_6$ film with microstructures favoring the photocatalytic property.

Besides the ordered mesoporous structure, the randomly distributed round concave areas with depths of ca. 60 nm might further contribute to the photocatalytic activity. Compared to the generally achieved ordered mesoporous structure with a smooth surface, such a 3-D nanoarchitecture enlarged the surface area of $MgTa_2O_6$ exposed to the RhB solution. Meanwhile, as evidenced from Figure 3, cracks that initiated during the calcination procedure, due either to the thermal mismatch between the $MgTa_2O_6$ film and the substrate or to the mechanical stress originating from the amorphous–crystalline transformation, were effectively confined within the round concaves, which improved the interfacial strength of the thin film.

The present nanoarchitectured mesoporous $MgTa_2O_6$ film possessed an optimized photocatalytic activity significantly higher than that of the ordered mesoporous anatase film. When considering the TOF value, the nanoarchitectured $MgTa_2O_6$ film calcinated at 790 °C possessed a photocatalytic activity ca. four times that of the mesoporous anatase film (Table 1). Although $MgTa_2O_6$ powders have been reported to possess the ability to assist photoinduced water-splitting, their activities are not promising [10,11]. The successful synthesis of the present novel nanoarchitectured $MgTa_2O_6$ film significantly promoted the potential property of $MgTa_2O_6$ as a photocatalyst, which we believe could find practical applications in heterogeneous photocatalysts and solar-induced water splitting.

Conclusion

Well-crystallized $MgTa_2O_6$ films with ordered mesoporous structures, imposed by randomly but homogeneously distributed round concaves, were synthesized through evaporation-induced self-assembly followed by calcination at temperatures above 760 °C. Such an advanced mesostructure can be achieved by special block copolymers such as KLE or polymers of the poly(isobutylene)-*b*-poly(ethylene oxide) type, which show similar properties in terms of structure and photocatalysis (see Supporting Information File 1). With increasing calcination temperature up to 1100 °C, two maxima in the photocatalytic activity for the $MgTa_2O_6$ film were achieved as a result of the combined effects of increasing crystallinity, increasing grain size, and deterioration of the ordered mesopores. The $MgTa_2O_6$ film with a novel nanoarchitecture possessed an enhanced ability to assist photodegradation of rhodamine B in water under UV irradiation. The optimal photocatalytic activity, when evaluated in terms of turnover frequency, was about four times that of previously reported anatase films with ordered mesopores [15] and even exceeded the photocatalytic performance of such films doped with other elements (see, e.g., [30] and references therein).

In conclusion, our work represents a show-case study regarding the interplay of crystallinity/crystallite size and mesoscopic order. The combination of photocatalytical characterization with comprehensive, temperature-dependent structural analysis proved that mesoporosity itself is not sufficient to endow metal oxides with advanced physicochemical performance.

Experimental section

Film fabrication

$MgCl_2$ (47 mg; 99.99%, Aldrich) and $Ta(OC_2H_5)_5$ (500 mg; 99.98%, Aldrich) were dissolved separately in ethanol (2 g) under magnetic stirring. After the addition of concentrated HCl (1.5 g) to the $Ta(OC_2H_5)_5$ solution, the $MgCl_2$ ethanolic solution was added dropwise. Finally, an isotropic solution consisting of the KLE template (100 mg; or 100 mg of the polymer F127 or PIB6000), ethanol (2 g) and tetrahydrofuran (1 g) was added, and the final precursor was stirred for a further 6–10 h before dip-coating. This amount of block copolymers was found to be optimum with respect to the mesostructural organization. The $MgTa_2O_6$ thin films were deposited on Si wafers by dip coating at a controlled relative humidity of 12% with a constant withdrawal speed of 6.5 mm s^{-1}, and then dried at 80 °C for 1 h in air and maintained at 300 °C overnight in order to stabilize the mesoporous structure. The subsequent calcination was conducted by heating to the desired temperatures at a rate of 5 K min^{-1}. The samples were then removed immediately and allowed to cool down rapidly. The nonporous $MgTa_2O_6$ film was fabricated in a similar procedure except that no template was added in the precursor.

Film characterization

Scanning electron microscopy (SEM) observations were performed in a LEO440 instrument with an acceleration voltage of 3.0 kV. Atomic force microscopy (AFM) investigations were conducted with a Nanoscope III, Digital Instruments, in tapping mode. Transmission electron microscopy (TEM) images were taken with a Zeiss EM 912Ω instrument at an acceleration voltage of 120 kV. The small-angle X-ray scattering (SAXS) and X-ray diffraction (XRD) measurements were performed in a Bruker D8 diffractometer with an accelerating voltage of 40 kV and a current of 40 mA, with Cu K_α radiation. The 2-D-SAXS measurements were carried out by using a Nonius rotating anode setup (Cu K_α radiation with $\lambda = 0.154$ nm) featuring a three-pinhole collimation system and a MAR CCD area detector, with a sample-to-detector distance of 750 mm. The angle β between the incident beam and the substrate was set to 10° or 90°. Ultrathin Si wafers with a thickness of ca. 30 μm were used for the 2-D-SAXS measurement.

Photocatalytic activity measurement

Rhodamine B (RhB), a xanthene dye molecule, was used as a probe to evaluate the photocatalytic activity of the thin films [22]. For each test, 33 mL RhB aqueous solution with an initial concentration of 0.01 mmol L^{-1} was illuminated with an 8 W UV lamp (λ_{max} = 254 nm, CAMAG, Germany) in the presence of the thin films with a total exposure surface area of ca. 16 cm^2. The distance between the lamp and the film was ca. 2 cm. The solution was stirred continuously and exposed to air during each run of the photocatalytic reaction for up to 120 min, interrupted at an interval of 30 min to monitor the change in RhB concentration. The relative concentration c/c_0 of RhB was determined by normalizing the absorption of the solution to that of the initial one (A/A_0) after a given reaction duration. Monitoring was conducted with a UV–vis spectrophotometer (UVIKON 931, Kontron Instruments, Switzerland) at a fixed wavelength of 554 nm, using a quartz cuvette of 1 cm as the optical path length.

Supporting Information

Supporting Information File 1

Additional Figures.
[http://www.beilstein-journals.org/bjnano/content/supplementary/2190-4286-3-13-S1.pdf]

Acknowledgements

J.-M. Wu appreciates the research fellowship awarded by the Alexander von Humboldt Foundation. Prof. Antonietti and MPI of Colloids and Interfaces are thanked for hosting J.-M. Wu and for scientific support for this study.

BASF SE (especially Dr. Cornelia Röger) is gratefully acknowledged for providing the PIB-PEO block copolymer.

References

1. Ferrari, C. R.; Hernandes, A. C. *J. Eur. Ceram. Soc.* **2002,** *22,* 2101. doi:10.1016/S0955-2219(02)00020-1
2. Tealdi, C.; Islam, M. S.; Malavasi, L.; Flor, G. *J. Solid State Chem.* **2004,** *177,* 4359. doi:10.1016/j.jssc.2004.06.055
3. Huang, C.-L.; Chiang, K.-H.; Huang, C.-Y. *Mater. Chem. Phys.* **2005,** *90,* 373. doi:10.1016/j.matchemphys.2004.10.037
4. Kim, E. S.; Kim, S. J.; Lee, H. G. *J. Ceram. Soc. Jpn.* **2008,** *116,* 545. doi:10.2109/jcersj2.116.545
5. Sun, D. C.; Senz, S.; Hesse, D. *J. Eur. Ceram. Soc.* **2004,** *24,* 2453. doi:10.1016/j.jeurceramsoc.2003.07.004
6. Navale, S. C.; Samuel, V.; Ravi, V. *Mater. Lett.* **2005,** *59,* 3926. doi:10.1016/j.matlet.2005.07.035
7. Navale, S. C.; Ravi, V. *Mater. Sci. Eng., B* **2005,** *119,* 189. doi:10.1016/j.mseb.2005.02.058
8. Mergen, A. *Ceram. Int.* **2009,** *35,* 1151. doi:10.1016/j.ceramint.2008.05.016
9. Ganguli, A. K.; Nangia, S.; Thirumal, M.; Gai, P. L. *J. Chem. Sci.* **2006,** *118,* 37. doi:10.1007/BF02708763
10. Kato, H.; Kudo, A. *Chem. Phys. Lett.* **1998,** *295,* 487. doi:10.1016/S0009-2614(98)01001-X
11. Kondo, J. N.; Uchida, M.; Nakajima, K.; Daling, L.; Hara, M.; Domen, K. *Chem. Mater.* **2004,** *16,* 4304. doi:10.1021/cm030355s
12. Smarsly, B.; Grosso, D.; Brezesinski, T.; Pinna, N.; Boissière, C.; Antonietti, M.; Sanchez, C. *Chem. Mater.* **2004,** *16,* 2948. doi:10.1021/cm0495966
13. Grosso, D.; Boissière, C.; Smarsly, B.; Brezesinski, T.; Pinna, N.; Albouy, P. A.; Amenitsch, H.; Antonietti, M.; Sanchez, C. *Nat. Mater.* **2004,** *3,* 787. doi:10.1038/nmat1206
14. Wang, Y.; Brezesinski, T.; Antonietti, M.; Smarsly, B. *ACS Nano* **2009,** *3,* 1373. doi:10.1021/nn900108x
15. Beyers, E.; Cool, P.; Vansant, E. F. *J. Phys. Chem. B* **2005,** *109,* 10081. doi:10.1021/jp050310+
16. Sakatani, Y.; Grosso, D.; Nicole, L.; Boissiere, C.; Soler-Illia, G. J. de A. A.; Sanchez, C. *J. Mater. Chem.* **2006,** *16,* 77. doi:10.1039/b512824m
17. Groenewolt, M.; Brezesinski, T.; Schlaad, H.; Antonietti, M.; Groh, P. W.; Iván, B. *Adv. Mater.* **2005,** *17,* 1158. doi:10.1002/adma.200401549
18. Smarsly, B.; Antonietti, M. *Eur. J. Inorg. Chem.* **2006,** *6,* 1111. doi:10.1002/ejic.200501003
19. Brezesinski, T.; Smarsly, B.; Iimura, K.-i; Grosso, D.; Boissiere, C.; Amenitsch, H.; Antonietti, M.; Sanchez, C. *Small* **2005,** *1,* 889. doi:10.1002/smll.200500024
20. Ruland, W.; Smarsly, B. M. *J. Appl. Crystallogr.* **2007,** *40,* 409. doi:10.1107/S0021889807010503
21. Wu, J.-M.; Antonietti, M.; Gross, S.; Bauer, M.; Smarsly, B. M. *ChemPhysChem* **2008,** *9,* 748. doi:10.1002/cphc.200700679
22. Zhang, L.; Yu, J. C. *Chem. Commun.* **2003,** 2078. doi:10.1039/b306013f
23. Wu, J.-M.; Qi, B. *J. Am. Ceram. Soc.* **2008,** *91,* 3961. doi:10.1111/j.1551-2916.2008.02786.x
24. Wu, J.-M.; Zhang, T.-W.; Zeng, Y.-W.; Hayakawa, S.; Tsuru, K.; Osaka, A. *Langmuir* **2005,** *21,* 6995. doi:10.1021/la0500272
25. Alvaro, M.; Aprile, C.; Benitez, M.; Carbonell, E.; Garcia, H. *J. Phys. Chem. B* **2006,** *110,* 6661. doi:10.1021/jp0573240
26. Linsebigler, A. L.; Lu, G.; Yates, J. T. *Chem. Rev.* **1995,** *95,* 735. doi:10.1021/cr00035a013
27. Carp, O.; Huisman, C. L.; Reller, A. *Prog. Solid State Chem.* **2004,** *32,* 33. doi:10.1016/j.progsolidstchem.2004.08.001
28. Wu, J.-M.; Huang, B.; Zeng, Y.-H. *Thin Solid Films* **2006,** *497,* 292. doi:10.1016/j.tsf.2005.10.066
29. Brezesinski, T.; Groenewolt, M.; Antonietti, M.; Smarsly, B. *Angew. Chem., Int. Ed.* **2006,** *45,* 781. doi:10.1002/anie.200502332
30. Zhao, J.; Sallard, S.; Smarsly, B. M.; Gross, S.; Bertino, M.; Boissière, C.; Chen, H.; Shi, J. *J. Mater. Chem.* **2010,** *20,* 2831. doi:10.1039/b919536j

License and Terms

Beilstein Journal
of Nanotechnology

Plasmonics-based detection of H_2 and CO: discrimination between reducing gases facilitated by material control

Gnanaprakash Dharmalingam, Nicholas A. Joy, Benjamin Grisafe
and Michael A. Carpenter*

Full Research Paper

Open Access

Address:
College of Nanoscale science and Engineering, University at Albany-State University of New York, 257 Fuller Road, Albany, New York 12203, United States

Email:
Michael A. Carpenter* - mcarpenter@albany.edu

* Corresponding author

Keywords:
hydrogen detection; nanocomposites gold nanoparticles; optical sensor; plasmonics; physical vapor deposition; surface plasmon resonance

Beilstein J. Nanotechnol. **2012,** *3,* 712–721.
doi:10.3762/bjnano.3.81

Received: 31 August 2012
Accepted: 18 October 2012
Published: 31 October 2012

This article is part of the Thematic Series "Chemical sensing with nanostructured materials".

Guest Editors: A. Gurlo and J. J. Schneider

Abstract

Monitoring emissions in high-temperature-combustion applications is very important for regulating the discharge of gases such as NO_2 and CO as well as unburnt fuel into the environment. This work reports the detection of H_2 and CO gases by employing a metal–metal oxide nanocomposite (gold–yttria stabilized zirconia (Au–YSZ)) film fabricated through layer-by-layer physical vapor deposition (PVD). The change in the peak position of the localized surface plasmon resonance (LSPR) was monitored as a function of time and gas concentration. The responses of the films were preferential towards H_2, as observed from the results of exposing the films to the gases at temperatures of 500 °C in a background of dry air. Characterization of the samples by XRD and SEM enabled the correlation of material properties with the differences in the CO- and H_2-induced LSPR peak shifts, including the relative desensitization towards NO_2. Sensing characteristics of films with varying support thicknesses and metal-particle diameters have been studied, and the results are presented. A comparison has been made to films fabricated through co-sputtered PVD, and the calibration curves of the sensing response show a preferential response towards H_2. The distinction between H_2 and CO responses is also seen through the use of principal-component analysis (PCA). Such material arrangements, which can be tuned for their selectivity by changing certain parameters such as particle size, support thickness, etc., have direct applications within optical chemical sensors for turbine engines, solid-oxide fuel cells, and other high-temperature applications.

Introduction

Sensors based on surface plasmon resonance have been a principal area of research in optical sensing devices [1-4]. The catalytic activity of highly dispersed gold particles either supported on metal oxides or embedded in metal oxides as discovered by Haruta et al. [5] served as pioneering work in the field of noble-metal catalysis in general, and particularly for plasmonics-based gas sensing. The extremely high sensitivity of the plasmon resonance peak to changes in the free-electron density of gold nanoparticles or a change in the dielectric function of the metal-oxide host material due to adsorbate reactions on surfaces makes this a viable chemical sensing technique. Although many metals, such as Cu, Al, and Ni [6], show characteristic plasmon peaks, they typically exhibit resonances at higher frequencies, which necessitates the use of complicated and expensive light sources. The use of gold or silver as the active sensing material does not warrant this, as the resonance wavelength region is in the visible and lower UV range, enabling the use of compact and inexpensive light sources. The choice of gold has thus been validated by its stability at high temperatures (the melting point of an unsupported 6 nm diameter Au nanoparticle, for example, is around 1150 K and decreases with decreasing particle size [7]).

There have been studies investigating the use of catalytically active gold or silver nanoparticles as optical sensors [8-12], along with theoretical models of the sensing response [13] and calculations of the sensitivity of the response to parameters such as shape, size and composition of the nanoparticles [14]. Ando et al. have reported, in one of the earlier investigations of sensing at high temperatures, the plasmonic sensing characteristics of Au nanoparticles when embedded in a CuO matrix, at a working temperature of 300 °C [15].

For consistent and sensitive detection of H_2, CO and NO_2, Rogers et al. and Sirinakis et al. used Au–yttria stabilized zirconia (Au–YSZ) films and reported sensing observations through hundreds of hours of laboratory testing between 500 and 800 °C [16-18]. While detection of these gases at high temperatures has been demonstrated, selectivity between these gases remains a challenging task, as many interactions between the different analyte gases and the film surface can be manifested as a change in the position of the plasmon peak. Selective detection of gases can be addressed either through a materials-development approach and/or the implementation of specific methods for data analysis. One example of this is selective chemiresistive sensor measurements with Ga_2O_3 materials. These studies showed that selectivity was enabled through the morphological tailoring of Ga_2O_3 and the use of both temperature changes as well as physical and chemical filters [19]. Another example in the direction of materials development is the work by Buso et al., who monitored specific wavelengths of the absorption spectrum of SiO_2 sol–gel films containing NiO and Au NPs during gas exposures. They demonstrated the selective detection of H_2 over CO, based on the differing response characteristics of the films in the different wavelength regions [20]. In another study, Gaspera et al. investigated the role of sol–gel-synthesized metal-oxide (NiO and TiO_2) films that were coated over Au NPs. One of the motivations of this work was to examine if the catalytic activity of the sol–gel-coated Au NPs increased due to the reduction in temperature-driven sintering of the Au NPs by the metal-oxide films, which would serve to reduce the Au NP size. They showed that such an arrangement had a reversible response to ethanol [21]. In the direction of investigating the use of both materials and statistical algorithms to discriminate the different responses of a single film towards the CO, H_2 and NO_2 target gases, Joy et al. recently demonstrated a method of extracting spectral information from sensing experiments using both supervised and unsupervised statistical algorithms, linear-discriminant analysis (LDA) and principal-component analysis (PCA), respectively [22]. This study has practical benefits in that relevant wavelength regions can be identified from the entire plasmon spectrum, as determined by statistical algorithms that show the greatest selective detection of the target analytes.

In the current work, a Au–YSZ film has been fabricated through a layer-by-layer physical vapor deposition (PVD) procedure, and the response of the film to H_2, CO and NO_2 at 500 °C has been monitored by observing the change in the position of the localized surface plasmon resonance (LSPR) peak. This work employs a layer-by-layer approach, meaning that the Au was first deposited and annealed to form nanoparticles and was then followed by the deposition and annealing of the YSZ capping layer. The metal-oxide overcoat has a crucial role in restricting the growth of the Au NPs during long-term high-temperature exposures, and its thickness has a direct impact on the number of oxygen vacancies in the film. The vacancies are introduced into the film through the yttria dopant in zirconia. YSZ is an excellent oxygen-ion conductor at temperatures greater than 300 °C, with almost 99% of its conductivity being due to the transport of oxygen ions above this temperature [23]. In the current study, an investigation into the dependence of the chemical sensing on Au particle size coupled with the YSZ-overcoat thickness has been performed for the first time. The resulting material properties of these films have produced a unique sensing dependence, which has enabled an enhanced detection of H_2 by a factor of 4 in comparison to CO. Such a strong difference in the detection of these two reducing gases is significant with respect to meeting the challenge towards selectivity. An additional analysis that exemplifies the differences between the two most prominent films was carried out by using PCA.

Results and Discussion

Exposure conditions and sensing results

The gases tested were H_2, CO and NO_2 in an air background. The exposure concentrations were 200, 500, 1000, 5000 and 10000 ppm for H_2 in dry air; 20, 50, 100, 500 and 1000 ppm for CO in dry air; and 2, 5, 10, 50 and 100 ppm for NO_2 in dry air. For ease of discussion, all samples with 3 nm Au but with 5/10/20 nm YSZ are referred to as medium-, large- and small-particle samples, respectively, and the film with 1.5 nm Au and 20 nm YSZ is referred to as the thinner gold sample. For comparison of the sensing data, a film fabricated by co-sputtering of the Au and YSZ, which was previously studied, was selected and is referred to as the co-sputtered sample. The exposure temperature was 500 °C, and all samples were allowed a warm-up time of five hours before the first exposure. An example of the shift in peak position, in this case for the small-particle sample on exposure to H_2, is shown in Figure 1 along with a sample Lorentzian fit used to determine the LSPR peak position, which was used as the sensing signal and monitored as a function of time. As these H_2 exposures were repeated a total of three times in a 72-hour experiment, a subset of the results for the hydrogen exposures are shown in Figure 2 and Figure 3.

From the exposure plots the most obvious observation is the shift in the plasmon resonance peak towards shorter wavelengths upon exposure to H_2. This shift is likely the result of interfacial charge-transfer reactions between H_2 and the oxygen anions forming water as the product [12-14]. As a result, electrons are transferred to the Au NPs inducing a blue shift or increase in LSPR frequency, ω, as characterized by the Drude model in Equation 1.

$$\omega = \sqrt{\frac{N_0 e^2}{(1+2\varepsilon_m)m_e\varepsilon_0}} \qquad (1)$$

In the above equation N_0 is the free-electron density of the Au particle, e the electron charge, ε_m the dielectric constant of the matrix and ε_0 the permittivity of vacuum [24]. These reactions will also likely induce a change in the polarizability of the YSZ matrix, changing the dielectric constant. The shift in the plasmon peak position will therefore be a result of the combined effect of the charge exchange and the change in dielectric properties of the YSZ. Other chemical reactions between H_2 and YSZ could also induce a change in the dielectric function, and while the adsorption of hydrogen is an activated process, the activation energy is typically less than 1 eV [25]. The uptake of hydrogen as an OH species by a zirconia matrix at temperatures between 673 and 873 K has been confirmed through studies using infra-red spectroscopy [26]. A significant difference between this previous study and practical studies of emission-gas sensing is that the measurements were not done in the presence of background oxygen. However, if H_2 were to react in the presence of an oxygen background, (such as in air) these reactions would induce a change in the dielectric function of the matrix. Such operando studies, combining chemical sensing measurements with analytical methods that simultaneously probe the reaction mechanism that induces the sensing response, remain a challenging experiment under relevant atmospheric sensing conditions.

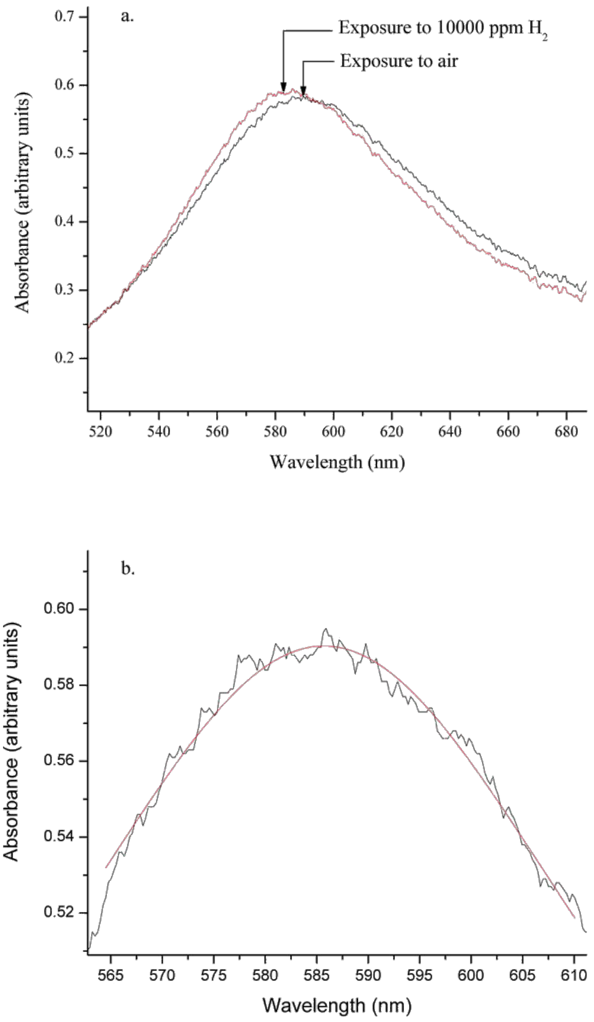

Figure 1: (a) Change in peak position of the small-particle sample between exposures to air and H_2. The lower plot (b) shows a sample Lorentzian fit (red line) of the absorbance spectrum to the spectrometer data (black line), which was used to monitor the change in peak position.

Inspection of Figure 2 and Figure 3 shows that while each of the five films responds well to H_2 as evidenced by the significant

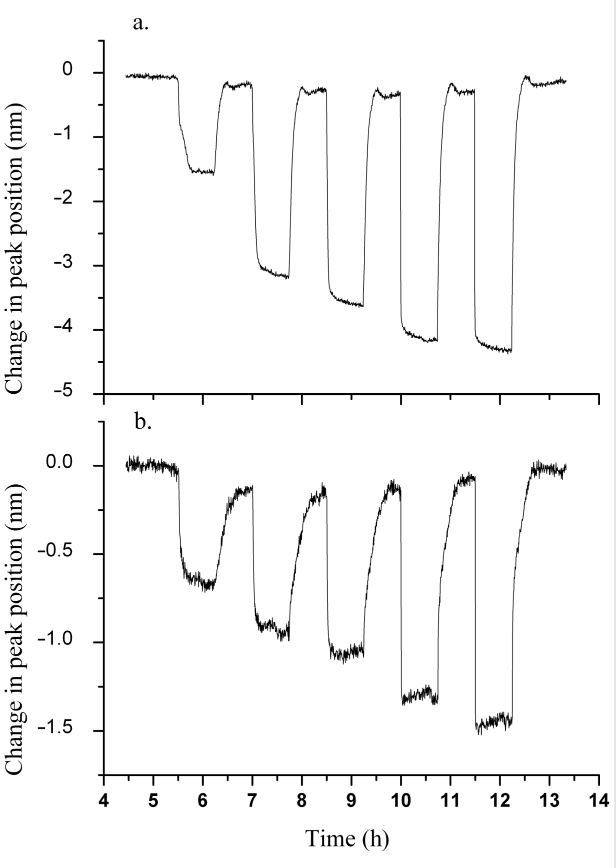

Figure 2: Hydrogen-exposure plots of (a) small-particle and (b) medium-particle samples. Concentrations of 200, 500, 1000, 5000 and 10000 ppm of H_2 in an air background were tested and are overlaid for the two samples, corresponding to increases along the time axis.

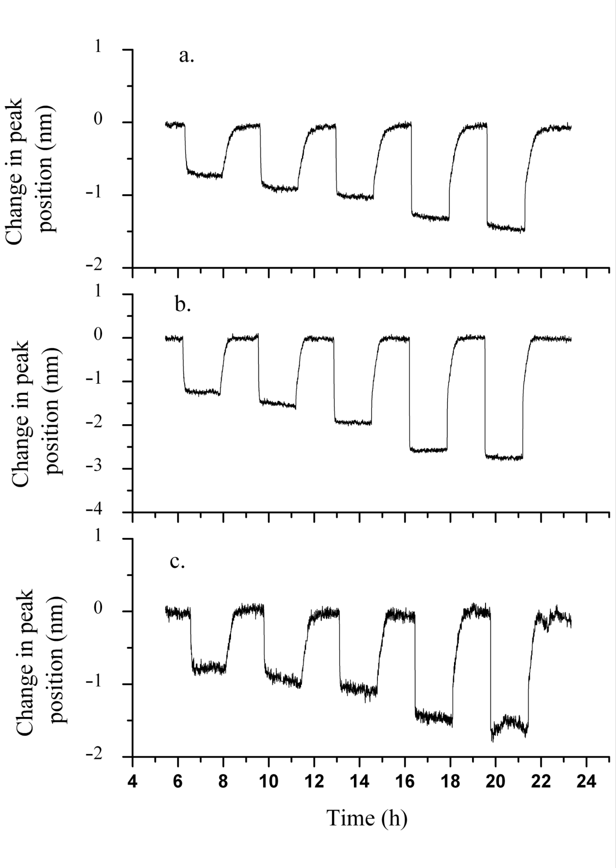

Figure 3: Hydrogen exposure plots of (a) thinner gold, (b) co-sputtered and (c) large-particle samples. The exposures are overlaid and correspond to concentrations of 200, 500, 1000, 5000 and 10000 ppm of H_2 in air, respectively, increasing along the time axis.

shifts in the plasmon peak position and the stable baseline peak position during the air cycles, the small-particle film is the most responsive among all samples. This is evident from the maximum change in the plasmon peak position as a function of H_2 concentration and is more clearly shown in the calibration curves in Figure 4. The data plotted is the change in LSPR peak position as a function of the H_2 concentration, with the values of the LSPR peak position representing the weighted average of three repeats for each gas concentration, and the error bars representing the uncertainty in the weighted average. The enhanced response of the small-particle film towards H_2 is quite interesting and is approximately a factor of 1.5 better than the co-sputtered film that was used in previous studies. The difference in response towards H_2 as a function of the film composition used in Figure 2 and Figure 3 requires some further comparison with respect to their morphological differences. One determining factor may be the respective oxygen vacancies in each of the films. For the calculation of the oxygen-vacancy concentration in all films, a general assumption was that the YSZ film had a cubic fluorite lattice structure. The calculations were performed by taking into account the deposited area,

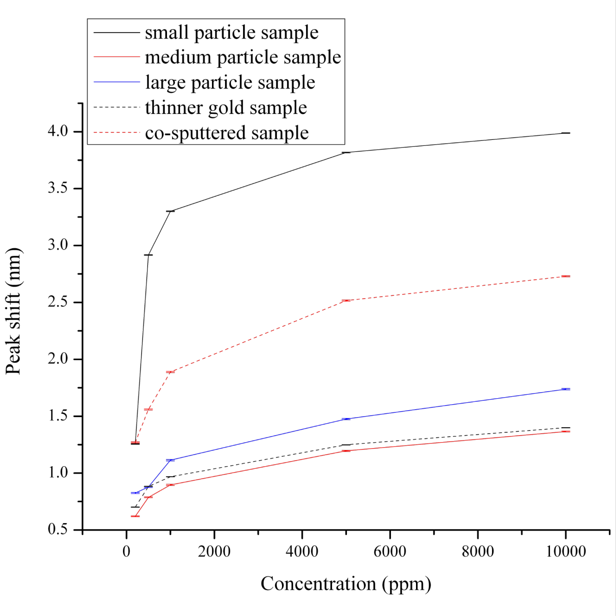

Figure 4: Calibration curves of all investigated samples for hydrogen. Error bars for each of the five separate H_2 exposures have been included.

thickness and lattice parameter of the YSZ film, and the number of oxygen vacancies that would be formed due to the yttria dopant level.

Calculation of the number of oxygen vacancies per square centimeter led to the following numbers for the films: 8.16 × 10^{15}/cm^2 for the small-particle sample and the thinner gold sample, 2.04 × 10^{15}/cm^2 for the medium-particle sample and 4.08 × 10^{15}/cm^2 for the large-particle sample. Given the proposed reaction mechanism, the enhanced response towards H_2 for the small-particle sample may be due to the highest oxygen vacancy concentration in this film among all the samples, which would facilitate an increase in H_2 adsorption, coupled with the smaller-diameter Au particles. Although the thinner Au sample has the same thickness of YSZ and hence essentially the same number of oxygen vacancies as the small-particle sample, the smaller Au particles in the latter case lead to an increased response. This may be attributed to the number of adsorption sites (such as defects, etc., which are the preferred sites for adsorption [27]) being higher for this sample. For the medium- and large-particle samples, the reduced response to H_2 in comparison to the small-particle sample may be a direct consequence of the fact that the reduced YSZ thickness would reduce the number of oxygen vacancies, decreasing the number of oxygen anion species for reaction. In comparing these films, it is noted that while there has not been a direct scaling of the magnitude of the change in plasmon peak position with YSZ thickness, the general qualitative trend of an increased response with an increase in the number of oxygen vacancies appears to be followed.

The samples were also tested for their response towards CO, and a subset of the exposure results are shown in Figure 5.

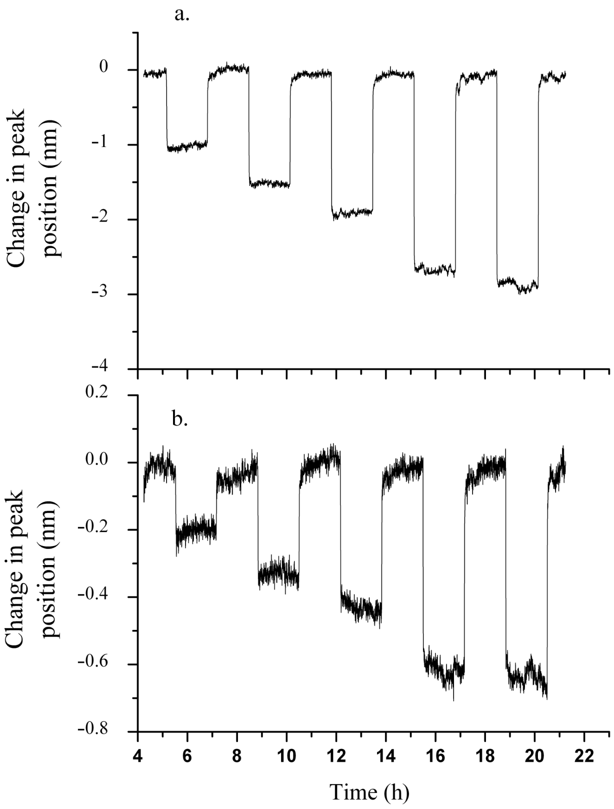

Figure 5: Exposure plots of (a) co-sputtered sample and (b) small-particle sample to CO. The concentrations tested were 20, 50, 100, 500 and 1000 ppm, respectively, in the increasing direction of the time axis.

Similar to H_2, the mechanism of the LSPR shift can be explained as follows. The adsorption of CO leads to the extraction of oxygen ions from the lattice, followed by injection of electrons from the O^{2-} ions into the matrix and CO_2 desorption. This can increase the free-electron density of the Au particles and cause the shift of the plasmon peak to the lower wavelength region of the spectrum. Similar to the H_2 experiments, these reactions could also affect the dielectric function. Although all samples were investigated for their response to CO, only the co-sputtered and small-particle samples showed a detectable response for all CO concentrations, as shown in Figure 5. The sample with the highest response was the co-sputtered sample with the small-particle sample having a small but measurable change in LSPR peak position. Each of the other samples either had a very small peak-shift response to the higher concentrations of CO, or none that was detectable above the baseline noise. The catalytic reaction of CO to CO_2 has been found to have a strong dependence on the Au NP size. Specifically, for inert metal-oxide supports, an enhancement in CO adsorption on the surface occurs only for particles with diameters less than 2 nm [28]. However, activity towards CO oxidation also occurs for particle diameters ranging from 12 to 30 nm when the particles are supported on active metal-oxide supports, such as Fe_2O_3 and YSZ. These supports are able to trap oxygen due to the presence of oxygen vacancies in their lattice. The combined effect of dissociative adsorption of oxygen on these supports with the activity of the Au nanoparticles produces an active material towards CO oxidation [29]. Thus, it was proposed that the ability of the YSZ support to provide reactive oxygen for CO oxidation increases the critical diameter for CO oxidation enhancement into the 10–30 nm range. It was noted, however, that the catalytic activity does decrease with increasing particle diameters, even for active supports. Rogers et al. [30] have also discussed the enhancement in sensitivity with decreasing particle sizes of Au for the detection of H_2, NO_2 and CO gases in a background gas containing mixtures of N_2 and O_2 as well as air. Thus, we propose that the reduced particle size, in addition to the fact that the metal oxide used in this study serves as an active support, is the reason for the observed increase in response of the co-sputtered sample (which has a mean particle size of 13 nm) when compared to the other samples (the sample with the smallest particles having a mean diameter of 48 nm). The calibration curves for CO response for the two samples (co-sputtered and small-particle sample) are shown in Figure 6.

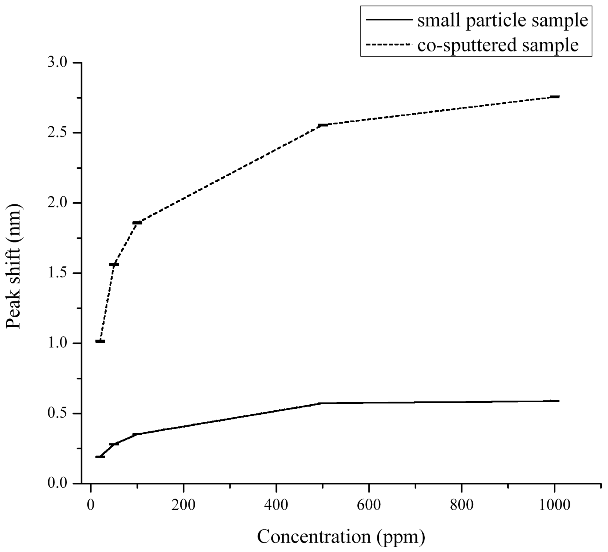

Figure 6: CO Calibration curves for the small particle sample and the co-sputtered sample. The error bars are shown for all concentrations.

Exposure to NO_2 should cause a red shift in the plasmon peak position, as it is known that NO_2 dissociates on Au–metal-oxide composites [31], and, provided oxygen vacancies are available, the dissociated oxygen would be adsorbed as either surface or lattice oxygen anions, O^- or O^{2-} respectively. This would cause a reduction in the free-electron density of Au and would decrease the plasmon frequency, causing the aforementioned red shift. Interestingly, all the layer-by-layer samples were relatively desensitized to NO_2. This conclusion was drawn from the fact that the maximum peak shift for the highest concentration of NO_2 was approximately 0.25 nm, a factor of 2 lower than the CO response, which in itself was much lower than the response towards H_2. The reason for the low response is likely the unavailability of oxygen vacancies in the YSZ matrix, as the samples are exposed to a constant air background. Thus, an almost completely saturated matrix (i.e., the vacancies are saturated due to O^{2-} formation from dissociative adsorption of O_2) is hypothesized as the cause for the low response of the samples towards NO_2. This hypothesis is further supported by the work of Rogers et al. [17], wherein the response to NO_2 was found to increase when the concentration of O_2 in the background gas was reduced from 20% to 5%. The exposure plot of the small-particle sample, which had the highest response, is shown in Figure 7 for NO_2 exposures of 5, 10, 50 and 100 ppm.

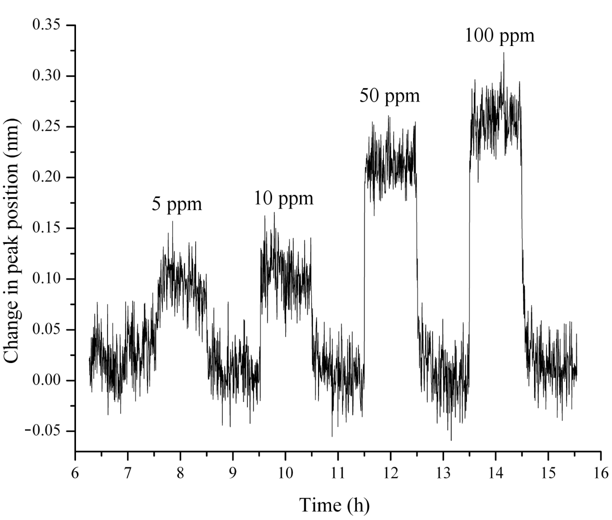

Figure 7: Exposure plot of small-particle sample to NO_2. The concentrations tested were 2, 5, 10, 50 and 100 ppm, and only the last four concentrations, for which the sample had a detectable response, have been shown here, in order of increasing time.

To summarize, the response of the small-particle sample to H_2 was found to be higher than that of the co-sputtered sample (a 150% increase in response, to 10,000 ppm of H_2), while the response to CO is much lower (a 450% reduction in response, to 1000 ppm of CO). Such a varied response to two reducing gases raises the possibility for the employment of these samples in a sensing array for the selective detection of H_2 and CO. We are currently probing the optimization of the small-particle-sample configuration so that it will have an increased response to H_2, while being even more desensitized to CO and NO_2. Optimization of the particle sizes and the thickness and chemistry of the metal-oxide support may help realize these objectives. To elicit the selective response of the small-particle sample towards CO and H_2, PCA was carried out on datasets for both the small-particle sample and the co-sputtered sample; the co-sputtered sample being selected because of its almost identical response towards H_2 and CO in terms of its respective change in plasmon peak position upon gas exposure.

Principal component analysis

The purpose of performing PCA is to extract as much information as possible from the absorbance spectrum of a sample in order to observe a unique response for each of the analytes. Of the many multivariate methods available, PCA is attractive due to its simplicity of application [22,32,33]. It is an unsupervised technique that reduces the dimensionality of a dataset while still retaining as much variance in the data as possible. In order to do this, data points are transformed onto a new set of orthogonal axes that run in directions of maximum variance in the data. Dimensionality can be reduced by projecting the data points onto a subspace of just the first two principal components (PCs), which typically retain most of the variance in the data.

For the present analysis, the observations, or data points, consist of each of the H_2 and CO concentrations (five each for H_2 and CO). The measured variables consist of 1570 individual wavelengths in the absorption spectrum between 450 and 850 nm. PCA was performed with the Python programming language by using singular value decomposition (SVD). Details on the mathematical procedure can be found elsewhere [34,35]. The observations were then projected onto the principal component 1 (PC1) and principal component 2 (PC2) axes and plotted in Figure 8, which are known as the PC scores plots.

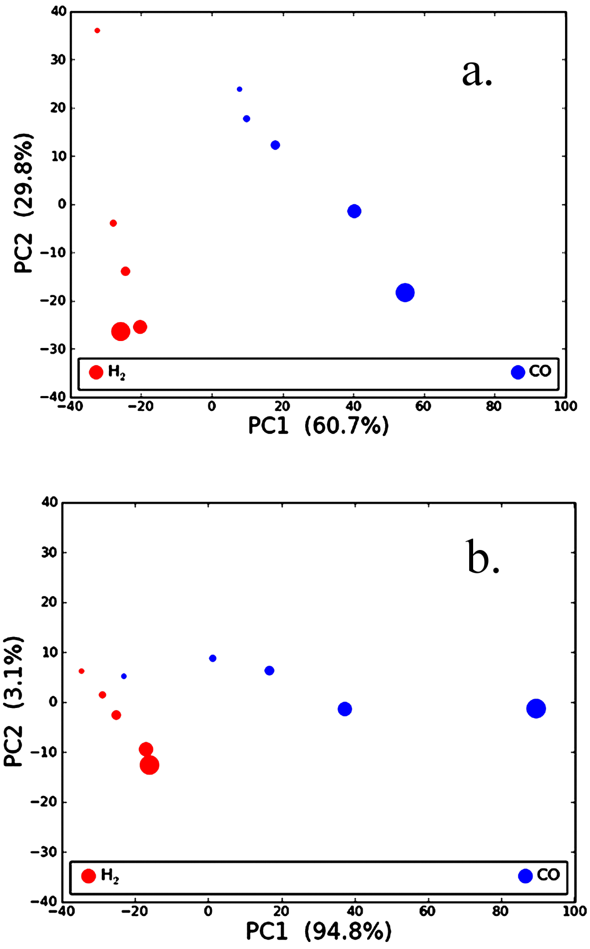

Figure 8: PC scores plot for (a) small-particle sample and (b) co-sputtered sample in an air background at 500 °C. The percent variance in the data described by each PC is listed in parentheses and data marker size increases with analyte concentration. The degree of separation between the H_2 (red) and CO (blue) markers is a qualitative measure of the difference in response of the sample to the two gases.

The PC scores plots can be viewed qualitatively based on the separation between the clusters of points representing H_2 exposure and clusters representing CO exposure. As the separation improves, it becomes easier to distinguish one analyte from the other. Given the range of concentrations tested for this experiment, points tend to form lines rather than clusters. However, a distinct separation between the H_2 and CO data points is seen for both samples in Figure 8. Although the analysis is limited in terms of the number of observations (i.e., data points), the results indicate that the small-particle sample has a distinction between H_2 and CO at all concentrations, while the co-sputtered sample has less separation of the data points at the lower concentrations. This suggests that the small-particle sample appears to be better suited to classifying the analytes at the lower concentrations. This observation is quite important as the selective detection of CO and H_2 for many types of metal-oxide-based sensing applications is problematic since they both react readily with the oxygen anion species and produce a similar response on the transducer of interest [1]. The results from this current study show that by tuning the material properties, a single metal-oxide film can have a CO response that is a factor of about 5 lower than that of H_2, evident from a plasmon peak shift of 0.6 nm for 1000 ppm of CO as opposed to 3.3 nm for 1000 ppm of H_2.

Conclusion

In this work, we have demonstrated that morphological modification of a Au-YSZ nanocomposite results in a vivid change in the response to H_2 and CO gases, and also an apparent desensitization to NO_2. The morphological switching mentioned here results from a change in the sample fabrication method from a co-sputtered Au–YSZ film, in which the Au particles are embedded in the YSZ matrix, to a layer-by-layer process for nanocomposite preparation. PCA analysis was employed to illustrate the difference in response between H_2 and CO for the co-sputtered and small-particle sample. These composites could serve as potential sensing materials in a sensor array for selective detection of H_2, CO and NO_2. Experiments are currently underway to determine the optimal configurations of these samples for a selective response to all gases. Further investigations to describe quantitatively and qualitatively the mechanism of charge exchange in terms of the reaction kinetics are in progress. Additional work to investigate the adsorbed species during the gas exposures through Raman spectroscopic characterization is on track, such that a predictive method of optimal sample preparation and configuration can be applied in the future.

Experimental

Film fabrication

Radio-frequency co-magnetron confocal physical-vapor deposition was used in the synthesis of all films. The general fabrication procedure was as follows: (i) deposition of 1.5 or 3 nm Au on quartz substrates with half of the substrate masked. The masked region allows for a reference spectrum to be continuously recorded during the spectral measurements of the Au–YSZ nanocomposite film. (ii) Annealing of the deposited Au film at a temperature of 900 °C for five minutes in an Ar environment with a flow of 2000 sccm. This annealing step results in the transition of the Au film to Au NPs. (iii) Deposition of the YSZ capping layer (5/10/20 nm thickness depending on the samples) on the Au film. And finally, (iv) annealing of the deposited films for three hours at 800 °C in a 2000 sccm flow of Ar to stabilize them for the sensing experiments. A half hour ramp-up and a final cool-down of the samples in argon were part of the annealing process.

The PVD targets used were Au of 99.99% purity and YSZ (99.9% purity) with a 5 wt % doping of yttria. The use of a constant annealing time and temperature for each of the samples lead to samples with Au particle sizes resulting from a change in PVD deposition conditions. The trends in particle sizes were corroborated by using environmental scanning electron microscopy (ESEM) and X-ray diffraction (XRD) The co-sputtered sample was fabricated by co-sputtering of Au and YSZ, by using a procedure described elsewhere [22]. Table 1 lists the sample nomenclature and the PVD deposition parameters. The selection of the co-sputtered film was based on the fact that the response to CO of the co-sputtered film was relatively similar in magnitude to its response to H_2. This is in stark contrast to the unique sensing response observed for films deposited in a layer-by-layer fashion. The layer-by-layer process has enabled the use of a unique set of samples with varying Au NP size and Au atomic percentage. Specifically, calculations of the Au content in each of the films revealed values of 2%, 8%, 4% and 1% for the small, medium, large and thinner gold samples, respectively, with the balance of these films being YSZ. The co-sputtered film was shown to have 9 atom % Au.

Optical sensing apparatus

The sensing apparatus used for the experiments is shown in Figure 9. The setup consists of, from right to left, an Ocean Optics tungsten halogen source with an emission wavelength range of 360–2500 nm; the quartz flow cell in which the sample is placed in the optical centerline by mounting in a Macor holder; a tube furnace for temperature control up to 900 °C; two lenses to create the optical image of the sample; and two beam splitters, which direct the beam onto two Ocean Optics spectrometers, one for recording the reference spectrum and the other for monitoring the spectrum from the sample. This setup is a simpler and lower-cost alternative to the 2-D CCD-imaging-based optical apparatus used previously [22]. The gas flow was regulated by computer-controlled mass-flow controllers supplied by MKS, and the total flow rate was maintained constant at 2000 sccm for all exposures.

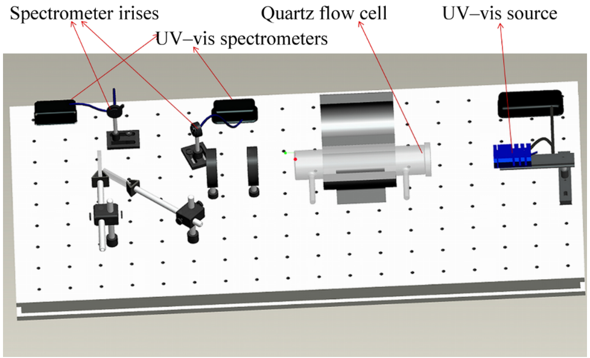

Figure 9: Optical sensing apparatus. From left: UV–vis source, quartz flow cell with gas inlet and outlet ports, tube furnace, focusing lenses, beam splitters and spectrometers.

Sample characterization

For characterizing the deposited samples, ESEM and XRD were used. ESEM analysis was carried out by using a FEI E-SEM 600, and the crystallite sizes from the ESEM images were calculated using ImageJ software, assuming spherical particles of gold. The particle (crystallite) diameters for all the samples are tabulated in Table 2.

Figure 10a,b and Figure 11a,b show ESEM images of the small-, medium- and large-particle samples, and the thinner gold sample, respectively. From the ESEM images the Au crystallites can be clearly seen, and the scaling of the Au particle size with decreasing YSZ thickness is obvious, except for the

Table 1: Sample nomenclature and physical-vapor-deposition parameters.

Sample ID	Thickness of Au layer (nm)	Thickness of YSZ overcoat (nm)	Deposition rate of Au layer (Å/s)	Deposition rate of YSZ overcoat (Å/s)
Small-particle sample	3	20	0.3	0.3
Medium-particle sample	3	5	0.3	0.3
Large-particle sample	3	10	0.3	1.4
Thinner-gold sample	1.5	20	0.3	1.4

Table 2: ESEM characterization results for PVD prepared samples. All values are in nanometers.

Sample ID	Mean crystallite size	Standard deviation in crystallite size
Small-particle sample	48	14
Medium-particle sample	64	23
Large-particle sample	125	48
Thinner gold sample	57	16

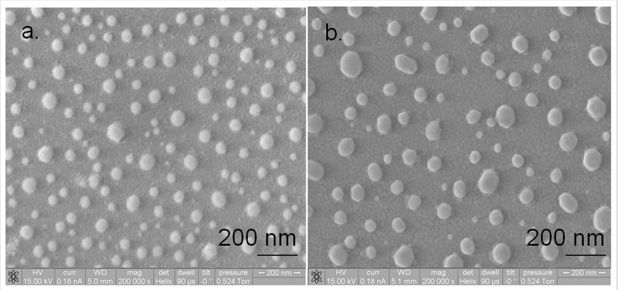

Figure 10: ESEM images of (a) small-particle and (b) medium-particle films. The annealing times were kept constant for all films so that variations in the particle size would be entirely a consequence of the deposition parameters. Diameter measurements were done on 172 particles for (a) and 89 particles for (b) to get the average sizes.

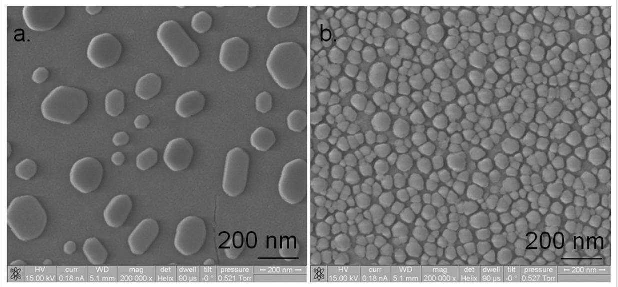

Figure 11: ESEM images of (a) large-particle sample and (b) thinner gold sample. Diameter measurements were carried out on 34 particles for (a) and 545 particles for (b) to arrive at the average sizes.

fact that the particle size of the large-particle film should have been smaller than that of the medium-particle film due to the larger YSZ thickness. We speculate that this deviation is due to the fact that the deposition rate during the sample preparation of the former film was three times higher than the latter, thereby possibly changing the morphology of the YSZ film and allowing an increased sintering of the Au crystallites during annealing.

XRD analyses were performed on the samples with a Scintag XDS 2000 by using Cu Kα radiation (wavelength of 1.54 Å). The crystallite sizes were determined by using the Scherrer Equation 2,

$$t = \frac{k\lambda}{\beta\cos\theta} \qquad (2)$$

Where t is the crystallite size in nanometers, k is the Scherrer constant (assumed to be 0.9), λ is the wavelength of the radiation, β is the value of the full width at half maximum (FWHM) of the Gaussian fit to the XRD peak profile, and θ is the diffraction angle. The tabulated values of the crystallite sizes for all samples have been included in Table 3, along with the calculated values from ESEM data for comparison. The instrumental contribution to the peak width for the XRD was accounted for by using the XRD profile fit of a thick gold sample with large Au particles (greater than 500 nm in diameter) within a YSZ film that was 40 nm thick.

The crystallite sizes from the ESEM and the XRD are mostly in reasonable agreement with respect to the average diameters. The small variations may be attributed to the fact that the calculations of the particle sizes for ESEM were not averaged over the entire sample surface, which could have resulted in a closer agreement with the XRD values. This is particularly true for the differences observed for the medium-particle sample, which shows values that are different by a factor of about 2.

Table 3: Crystallite sizes calculated from XRD data and the Scherrer equation. ESEM particle sizes are shown for comparison. All values are in nanometers.

Sample ID	Average crystallite size from XRD	Average crystallite size from ESEM
Small-particle sample	58	48
Medium-particle sample	129	64
Large-particle sample	120	125
Thinner gold sample	63	70

Acknowledgements

This work was supported in part by the United States Department of Energy National Energy Technology Laboratory under contract number DE-FE0007190 as well as the National Science Foundation [PN: 1006399]. Any opinions, findings, and conclusions or recommendations expressed in this publication are those of the authors and do not necessarily reflect the views of the United States Department of Energy National Energy Technology Laboratory.

References

1. Carpenter, M. A.; Mathur, S.; Kolmakov, A., Eds. *Metal Oxide Nanomaterials for Chemical Sensors;* Springer, 2012.
2. Ohodnicki, P. R., Jr.; Wang, C.; Natesakhawat, S.; Baltrus, J. P.; Brown, T. D. *J. Appl. Phys.* **2012,** *111,* 064320. doi:10.1063/1.3695380
3. Lesuffleur, A.; Im, H.; Lindquist, N. C.; Oh, S.-H. *Appl. Phys. Lett.* **2007,** *90,* 243110. doi:10.1063/1.2747668
4. Wang, C.; Ma, L.; Hossain, M.; Wang, H.; Zou, S.; Hickman, J. J.; Su, M. *Sens. Actuators, B* **2010,** *150,* 667–672. doi:10.1016/j.snb.2010.08.022
5. Haruta, M.; Kobayashi, T.; Sano, H.; Yamada, N. *Chem. Lett.* **1987,** *16,* 405–408. doi:10.1246/cl.1987.405
6. Rhodes, C.; Franzen, S.; Maria, J.-P.; Losego, M.; Leonard, N. D.; Laughlin, B.; Duscher, G.; Weibel, S. *J. Appl. Phys.* **2006,** *100,* 054905. doi:10.1063/1.2222070
7. Shim, J.-H.; Lee, B.-J.; Cho, Y. W. *Surf. Sci.* **2002,** *512,* 262–268. doi:10.1016/S0039-6028(02)01692-8
8. Brolo, A. G.; Gordon, R.; Leathem, B.; Kavanagh, K. L. *Langmuir* **2004,** *20,* 4813–4815. doi:10.1021/la0493621
9. Larsson, E. M.; Langhammer, C.; Zorić, I.; Kasemo, B. *Science* **2009,** *326,* 1091–1094. doi:10.1126/science.1176593
10. Tu, M. H.; Sun, T.; Grattan, K. T. V. *Sens. Actuators, B* **2012,** *164,* 43–53. doi:10.1016/j.snb.2012.01.060
11. Lertvachirapaiboon, C.; Yamazaki, R.; Pienpinijtham, P.; Baba, A.; Ekgasit, S.; Thammacharoen, C.; Shinbo, K.; Kato, K.; Kaneko, F. *Sens. Actuators, B* **2012,** *173,* 316–321. doi:10.1016/j.snb.2012.07.003
12. Hashimoto, N.; Hashimoto, T.; Teranishi, T.; Nasu, H.; Kamiya, K. *Sens. Actuators, B* **2006,** *113,* 382–388. doi:10.1016/j.snb.2005.03.033
13. Lee, K.-S.; El-Sayed, M. A. *J. Phys. Chem. B* **2006,** *110,* 19220–19225. doi:10.1021/jp062536y
14. Xu, H.; Käll, M. *Sens. Actuators, B* **2002,** *87,* 244–249. doi:10.1016/S0925-4005(02)00243-5
15. Ando, M.; Kobayashi, T.; Iijima, S.; Haruta, M. *Sens. Actuators, B* **2003,** *96,* 589–595. doi:10.1016/S0925-4005(03)00645-2
16. Rogers, P. H.; Sirinakis, G.; Carpenter, M. A. *J. Phys. Chem. C* **2008,** *112,* 6749–6757. doi:10.1021/jp712007f
17. Rogers, P. H.; Sirinakis, G.; Carpenter, M. A. *J. Phys. Chem. C* **2008,** *112,* 8784–8790. doi:10.1021/jp800524z
18. Sirinakis, G.; Siddique, R.; Manning, I.; Rogers, P. H.; Carpenter, M. A. *J. Phys. Chem. B* **2006,** *110,* 13508–13511. doi:10.1021/jp062760n
19. Fleischer, M.; Meixner, H. *Sens. Actuators, B* **1998,** *52,* 179–187. doi:10.1016/S0925-4005(98)00271-8
20. Buso, D.; Busato, G.; Guglielmi, M.; Martucci, A.; Bello, V.; Mattei, G.; Mazzoldi, P.; Post, M. L. *Nanotechnology* **2007,** *18,* 475505. doi:10.1088/0957-4484/18/47/475505
21. Gaspera, E. D.; Karg, M.; Baldauf, J.; Jasieniak, J.; Maggioni, G.; Martucci, A. *Langmuir* **2011,** *27,* 13739–13747. doi:10.1021/la2032829
22. Joy, N. A.; Nandasiri, M. I.; Rogers, P. H.; Jiang, W.; Varga, T.; Kuchibhatla, S. V. N. T.; Thevuthasan, S.; Carpenter, M. A. *Anal. Chem.* **2012,** *84,* 5025–5034. doi:10.1021/ac3006846
23. Kosacki, I.; Petrovsky, V.; Anderson, H. U. *J. Electroceram.* **1999,** *4,* 243–249. doi:10.1023/A:1009940616970
24. Kreibig, U.; Vollmer, M. *Optical Properties of Metal Clusters;* Springer: Berlin, 1995.
25. Joy, N. A.; Settens, C. M.; Matyi, R. J.; Carpenter, M. A. *J. Phys. Chem. C* **2011,** *115,* 6283–6289. doi:10.1021/jp112228h
26. Trunschke, A.; Hoang, D. L.; Lieske, H. *J. Chem. Soc., Faraday Trans.* **1995,** *91,* 4441–4444. doi:10.1039/ft9959104441
27. Benvenutti, E. V.; Franken, L.; Moro, C. C. *Langmuir* **1999,** *15,* 8140–8146. doi:10.1021/la990195s
28. Chen, M.; Goodman, D. W. *Acc. Chem. Res.* **2006,** *39,* 739–746. doi:10.1021/ar040309d
29. Liu, H.; Kozlov, A. I.; Kozlova, A. P.; Shido, T.; Asakura, K.; Iwasawa, Y. *J. Catal.* **1999,** *185,* 252–264. doi:10.1006/jcat.1999.2517
30. Rogers, P. H.; Carpenter, M. A. *J. Phys. Chem. C* **2010,** *114,* 11033–11039. doi:10.1021/jp101299k
31. Choi, K.-H.; Coh, B.-Y.; Lee, H.-I. *Catal. Today* **1998,** *44,* 205–213. doi:10.1016/S0920-5861(98)00192-8
32. Beebe, K. R.; Pell, R. J.; Seasholtz, M. B. *Chemometrics: A Practical Guide;* Wiley: New York, NY, 1998.
33. Potyrailo, R. A.; Leach, A. M.; Surman, C. M. *ACS Comb. Sci.* **2012,** *14,* 170–178. doi:10.1021/co200112s
34. Jackson, J. E. *A user's guide to principal components;* Wiley-IEEE: New York, U.S.A., 2003.
35. Jolliffe, I. T. *Principal Component analysis;* Springer: New York, U.S.A., 2002.

License and Terms